UNIVERSITAT DE BARCELONA
DEPARTAMENT D'ASTRONOMIA I METEOROLOGIA

UNIVERSITAT DE BARCELONA

Determination of the distance to the Andromeda Galaxy using variable stars

Memòria presentada per
Francesc Vilardell Sallés
per optar al grau de
Doctor en Física

Barcelona, gener de 2009

Programa de Doctorat d'Astronomia i Meteorologia

Bienni 2002–2004

Memòria presentada per **Francesc Vilardell Sallés** per optar al grau de Doctor en Física

Directors de la tesi

Dra. Carme Jordi i Nebot

Dr. Ignasi Ribas i Canudas

A la Nuria

Contents

Agraïments **ix**

Resum **xi**

1 Introduction **1**
1.1 The extragalactic distance ladder 1
1.2 The Andromeda Galaxy 3
1.3 Eclipsing binaries 5
1.3.1 Distance determination methods 10
1.3.2 The experience of LMC 11
1.3.3 Eclipsing binaries in M 31 and M 33 12
1.4 Goals 13

2 Time series photometry **15**
2.1 Observations 15
2.2 Data reduction 16
2.2.1 Data calibration 16
2.2.2 Difference image analysis 17
2.2.3 Standard photometry 19
2.2.4 Astrometry 22
2.2.5 Periodicity search 23
2.3 The catalogs 24
2.3.1 Reference catalog 24
2.3.2 Variable star catalog 27
2.4 Selection of variable stars suitable for distance determination . . . 29
2.4.1 Eclipsing binaries 29
2.4.2 Cepheids 36

3 Spectroscopy and spectrophotometry **39**
3.1 Spectroscopy 39
3.1.1 Observations 39
3.1.2 Data reduction 41
3.2 Spectrophotometry 43
3.2.1 Observations 43
3.2.2 Data reduction 45

4 Eclipsing binaries **53**
4.1 Physical properties 54
4.1.1 M31V J00443799+4129236 54
4.1.2 M31V J00443610+4129194 66
4.1.3 M31V J00444528+4128000 73
4.1.4 M31V J00442326+4127082 81
4.2 Distance determination 88

5 Cepheids **91**
5.1 Period distribution 92
5.2 Fourier decomposition 93
5.3 Period-luminosity relationship 95
5.3.1 Absorption 97
5.3.2 Metallicity 98
5.3.3 Blending 99
5.4 Distance determination 105

6 The distance to M 31 and final remarks **109**
6.1 The distance to M 31 109
6.2 Summary of the results 112
6.2.1 Data acquisition, reduction and analysis 112
6.2.2 Properties of eclipsing binaries 114
6.2.3 Properties of Cepheids 116
6.2.4 Distance determinations 116
6.3 Future work 117

Bibliography **119**

A Large optical flare **127**
A.1 The observed phenomenon 127
A.2 Stellar properties 128
A.3 Flare energy estimation 130
A.4 Weak flaring and post-flare events 132

Agraïments

Hi ha qui recorre els camins de la vida només per veure el final, sense adonar-se que el més important no és el destí, sinó el trajecte. La vida mateixa és un clar exemple d'aquesta metàfora on el més important no és arribar al final (a la mort), sinó disfrutar de la vida mateixa. Una tesi doctoral és un altre clar exemple. Hi ha qui prepara una tesi doctoral únicament i exclusiva per arribar al final, sense adonar-se que el més important no és el resultat sinó tot el que s'ha viscut i s'ha après en el transcurs d'aquesta.

De particular importància és la gent que un ha conegut i amb la que s'ha conviscut al llarg del recorregut. És per aquest motiu que és important, i és de justícia que, arribat el moment, es valorin les persones que han ajudat a arribar al final del camí.

En primer lloc, evidentment, hi ha els meus dos directors de tesi, la Carme i l'Ignasi. Ells han sigut les persones que m'han encaminat i dirigit des del començament del camí i que, d'alguna manera, m'han servit d'estrelles guia per trobar la direcció correcta en cada moment del trajecte.

En segon lloc, vull agrair la seva companyia a tots els companys de viatge del Departament d'Astronomia i Meteorologia de la Universitat de Barcelona (i alguns de fora). La llista és llarga, gairebé tant com el camí recorregut, però tots m'han ajudat en algun aspecte d'aquest treball, ja sigui il·luminant les zones fosques del camí, fent-me més clars els indicadors més amagats, o simplement compartint una bona conversa mentre feia una parada per descansar del llarg viatge. Que sapigueu que us recordo a tots, fins i tot aquells que penseu que no heu fet res. La vostra companyia és impagable.

Cal agrair també l'ajuda que m'han donat totes les persones del *Department of Astronomy and Astrophysics* a la *Villanova University* i del *Department of Physics and Astronomy* a la *Tel Aviv University*. La seva amabilitat i la seva hospitalitat, fins i tot oferint-se a fer algunes parts del meu camí, m'han fet sentir com a casa, tot i estar molt lluny del punt de partida.

Finalment, vull agrair l'ajuda i el suport dels meus pares, que m'han fet de bastó i que m'han donat suport durant tots aquests anys i, de fet, des de molt abans de començar.

L'últim record és per una de les persones que més m'ha ajudat al llarg del camí, la Nuria. Una persona que m'ha fet de bastó, que m'ha il·luminat el camí i que, amb la seva atenció i la seva paciència, m'ha ajudat a trobar els camins més amagats.

A tots, moltes gràcies.

Resum⋆

Introducció

La determinació de distàncies es basa en un procés jeràrquic (conegut com a escala cosmològica de distàncies) on els objectes propers amb distàncies ben determinades s'utilitzen per trobar distàncies d'objectes més llunyans. Les paral·laxis trigonomètriques (utilitzades per determinar distàncies a les estrelles més properes) són pràcticament l'únic mètode directe de determinació de distàncies. Tota la resta de mètodes es basen (fins a cert punt) en el coneixement de la lluminositat intrínseca de certs objectes (que reben el nom de candeles estàndard).

Tot i que hi ha un gran nombre de candeles estàndard (Fig. 1.1), les estrelles Cefeides jugen un paper predominant en l'escala cosmològica de distàncies. La importància de les Cefeides rau en la seva relació període-lluminositat (P-L) la qual relaciona el període de polsació amb la magnitud absoluta. Per determinar amb precisió la relació P-L, s'utilitzen mesures tant a la Via Làctia com al Núvol Gran de Magallanes (LMC). És per aquest motiu que es considera que LMC és el primer esglaó extragalàctic de l'escala cosmològica de distàncies.

De tota manera, la geometria irregular de LMC, juntament amb la seva baixa metal·licitat i la gran dispersió de les distàncies obtingudes fins ara (Fig. 1.2), ha introduït alguns dubtes pel que fa la seva idoneïtat com a primer esglaó extragalàctic. Així doncs, calen mesures precises a altres galàxies del Grup Local per tal de determinar un calibratge precís de l'escala cosmològica de distàncies.

En aquest sentit, la galàxia d'Andromeda (M 31) pot representar un excel·lent calibrador, ja que té una rica població estel·lar i presenta diverses candeles estàndard que no té LMC. A més a més, és prou propera com per poder observar estrelles individuals, a la vegada que està prou lluny com perquè la seva geometria no introdueixi cap sistemàtica en la determinació de distàncies. Desafortunadament, tot i que hi ha diverses determinacions de la distància a M 31 (Taula 1.1),

⋆Summary in Catalan (according to the rules at the Universitat de Barcelona).

no hi ha cap determinació directa (totes es basen en calibratges de la Via Làctia o del Núvol Gran de Magallanes).

Les binàries eclipsants poden suplir aquesta mancança. Les binàries eclipsants són sistemes compostos per dues estrelles que, en orbitar l'una al voltant de l'altra, presenten eclipsis periòdics. Les binàries eclipsants sempre han estat una eina important per determinar les propietats físiques de les estrelles. El gran potencial de les binàries eclipsants és que el seu moviment (observat a les corbes de velocitat radial) i la forma dels eclipsis (observats a les corbes de llum) es poden explicar completament a partir de les lleis de gravitació universal i de la geometria dels sistema (vegeu Hilditch, 2001, per més detalls). Així doncs, per a una binària eclipsant, la combinació de les corbes de llum i les corbes de velocitat radial permet la determinació de les propietats físiques dels components (com la massa i el radi) de forma directa i a partir de principis fonamentals.

Un cop conegut el radi dels components, cal determinar el flux superfical de cadascun d'ells per conèixer-ne la distància. S'han proposat diversos mètodes per tal de determinar el flux superficial (i la distància) de les binàries eclipsants. D'entre els diversos mètodes, en destaca el mètode espectrofotomètric, pel fet que el flux superficial dels components es determina conjuntament amb l'absorpció interestel·lar i la distància (Eq. 1.13). Aquest mètode es va utilitzar per determinar la distància a quatre binàries eclipsant a LMC (Taula 1.3), obtenint un mòdul de distància de $(m - M)_0 = 18.42 \pm 0.06$ mag.

Com a pas següent per al calibratge de l'escala cosmològica de distàncies, l'objectiu del present treball és la determinació de la distància a M 31 mitjançant binàries eclipsants. A l'inici d'aquest projecte, les úniques binàries eclipsants amb fotometria CCD a M 31 eren les identificades pel grup DIRECT (Macri, 2004). Com que la qualitat de les corbes de llum és insuficient per al nostre objectiu, en el transcurs del present treball s'ha obtingut nova fotometria, així com les velocitats radials necessàries. Les dades obtingudes s'han utilitzat per determinar les propietats físiques de les binàries eclipsants estudiades, així com la distància a M 31. Juntament amb les binàries eclipsants, la fotometria ha proporcionat un gran nombre de Cefeides i excel·lents corbes de llum d'altres objectes. Les Cefeides s'han analitzat per determinar una distància addicional a M 31. Finalment, el potencial del catàleg fotomètric obtingut es posa de manifest amb l'anàlisi de les propietats d'una fulguració estel·lar descoberta en el transcurs d'aquest treball.

Sèries fotomètriques

Les observacions per obtenir les corbes de llum de binàries eclipsants a M 31 van ser realitzades amb el telescopi Isaac Newton (INT) a la Palma. En total es van obtenir unes 260 imatges amb l'instrument Wide Field Camera (entre 1999 i 2003) en cadascun dels dos filtres: B i V de Johnson.

Les imatges obtingudes van ser corregides de *overscan*, de *bias* i de *flat-field*. Els píxels dolents es van corregir mitjançant interpolació dels píxels adjacents. El resultat són unes imatges corregides de gairebé tots els defectes instrumentals, excepte un petit efecte de diafragma a la cantonada nord-est del camp (Fig. 2.1).

Com que el camp és extremadament poblat d'estrelles, vàrem adaptar un algoritme basat en la tècnica de substracció d'imatges (Alard & Lupton, 1998) per adquirir la fotometria de les estrelles del camp. El procés de substracció d'imatges consisteix, primerament, en la creació d'una imatge de referència a partir de les imatges amb millor *seeing* i major relació senyal-soroll. A continuació, es resta la imatge de referència a totes les imatges obtingudes per tal d'obtenir una imatge diferenciada que conté només estrelles variables. La imatge diferenciada s'utilitza per obtenir la variació de flux de les estrelles variables respecte de la imatge de referència (també anomenat fotometria diferencial).

Per tal de transformar la fotometria diferencial a fotometria instrumental, vàrem realitzar fotometria mitjançant DAOPHOT (Stetson, 1987) a la imatge de referència. Amb la fotometria de referència i la fotometria diferencial, ja es poden obtenir les magnituds instrumentals mitjançant l'Eq. 2.1. Com que la fotometria DAOPHOT i la fotometria diferencial es basen en processos differents, vàrem utilitzar un factor d'escala que transforma les magnituds a un sistema estàndard.

Un cop obtingudes les magnituds instrumentals, vàrem calcular les magnituds estàndard a partir d'estrelles estàndard de Landolt (1992), observades durant dues nits de la campanya del 1999. El procés va proporcionar fotometria estàndard per a 236 238 estrelles de la imatge de referència, amb magnituds $17.5 < V < 25.5$ i $18 < B < 26$ (37 241 de les quals tenen un error fotomètric inferior a 0.1 mag en els dos filtres). Addicionalment, també es van transformar les magnituds instrumentals de les 3 964 estrelles variables a magnituds estàndard.

Juntament amb la fotometria, també vàrem determinar la posició de totes les estrelles detectades. Per això vàrem creuar les estrelles detectades amb el catàleg GSC 2.2.1, obtenint una transformació de coordenades que té una precisió de 0.16 segons d'arc en ascensió recta, i de 0.12 en declinació.

L'últim pas en el procés de reducció és la determinació de la possible periodicitat de les estrelles variables. Per tal de detectar periodicitats, vàrem aplicar un algoritme d'anàlisi de la variança (Schwarzenberg-Czerny, 1996) a les corbes de llum, en tots dos filtres, de les 3 964 estrelles variables detectades. Les corbes de llum resultants d'aquesta anàlisi van ser inspeccionades visualment per identificar patrons de variabilitat coneguts. Com a resultat, vàrem identificar 437 binàries eclipsants i 416 Cefeides.

Així doncs, el procés de reducció va proporcionar-nos dos catàlegs: el catàleg de referència i el catàleg d'estrelles variables (Sect. 2.3). Per tal d'assegurar-se que el procés de reducció fotomètric és acurat, vàrem comparar la fotometria del catàleg de referència amb dos catàlegs que tenen un gran nombre d'estrelles en

comú amb el catàleg obtingut: DIRECT (Macri, 2004) i LGGS (Massey et al., 2006). El resultat de la comparació mostra que les magnituds *B* obtingudes són completament compatibles amb les magnituds proporcionades per LGGS (Fig. 2.6 i Fig. 2.7). Pel que fa a les magnituds en *V*, s'observa una certa tendència en les dues comparacions. Donat que les tendències són diferents segons quin sigui el catàleg de comparació, és impossible de saber si hi ha algun effecte sistemàtic en la fotometria en *V*. En qualsevol cas, aquests efecte és inferior a 0.03 mag per estrelles amb $V < 20.5$ mag.

Pel que fa al catàleg d'estrelles variables, cal dir que s'ha comparat la fotometria de les binàries eclipsants amb dos catàlegs: DIRECT i T05 (Todd et al., 2005). El resultat de la comparació mostra que T05 té una sistemàtica a les binàries anomenades f2BEB i f3BEB del seu catàleg (Fig. 2.9 i Taula 2.2), mentre que les magnituds de les nostres binàries eclipsants són compatibles amb les obtingudes per DIRECT.

Un cop obtingudes les sèries fotomètriques i un cop comprovada la seva fiabilitat, vàrem continuar amb la selecció de binàries eclipsants adequades per a la determinació de distàncies. De les 437 binàries identificades al catàleg d'estrelles variables, les més aptes per a la determinació de distàncies són aquelles que són prou brillants com per obtenir-ne velocitats radials amb la instrumentació actual. Tenint en compte que els telescopis més grans tenen entre 8 i 10 metres, i que calen dispersions de l'ordre de R$\sim$3 000 en els espectres, vàrem seleccionar només aquelles binàries eclipsants que tenen una magnitud $V < 20.5$. A més a més, per a una precisa determinació dels paràmetres físics, cal que les binàries tinguin eclipsis profunds ($\Delta V > 0.2$ mag). El resultat són 24 binàries eclipsants aptes per a la determinació de la distància a M 31.

Donat que les característiques pròpies de cada sistema binari poden tenir una important influència en la determinació precisa de les seves propietats, vàrem realitzar un ajust preliminar de les 24 binàries eclipsants seleccionades amb el programa de Wilson & Devinney (1971, W&D). Per tal de reduir la correlació entre els paràmetres i obtenir solucions més estables, vàrem considerar, per a cada sistema, dues configuracions possibles (separat i semi-separat), en funció de si els components del sistema binari omplen o no el lòbul de Roche. En general, l'ajust resultant proporciona pistes sobre quina és la solució òptima per a cada sistema. De tota manera, aquells sistemes que presenten indicis d'excentricitat van ser considerats com a separats. A més a més, en alguns casos, s'observa l'anomenat efecte O'Connell (Davidge & Milone, 1984), degut a la presència de taques a la superfície de les estrelles. Tenint en compte que les estrelles estudiades es troben a la part superior de la seqüència principal (Fig. 2.10), aquest efecte es pot explicar com a conseqüència de l'impacte del material procedent d'una estrella sobre la companya. Així doncs, aquests sistemes es van suposar que eren semi-separats.

Els paràmetres determinats per a cada sistema són: temps de mínim, període, inclinació, quocient de temperatures, potencial superfical normalitzat de la primà-

ria i quocient de lluminositats. Per sistemes separats, a més a més, s'ha determinat el potencial superficial normalitzat de la secundària i, en cas de ser excèntrics, l'excentricitat i l'argument del periastre. A la solució final, també es va ajustar la tercera llum, és a dir, la contribució deguda a d'altres estrelles en la lluminositat del sistema binari (vegeu l'apartat 2.4.1 per a més detalls). Els ajustos resultants es poden veure a la Fig. 2.11, mentre que els paràmetres derivats es poden veure a la Taula 2.3.

Espectroscòpia i espectrofotometria

Com a pas següent en la determinació de la distància a M 31, vàrem obtenir espectroscòpia amb el telescopi Gemini-North (Hawaii) i l'instrument GMOS. El camp observat conté 5 de les 24 binàries eclipsants seleccionades anteriorment. En total vàrem obtenir nou espectres per a cadascuna de les cinc binàries, entre setembre de 2004 i febrer de 2005, amb 4100 segons d'exposició per cadascun d'ells (l'últim dels quals amb un temps d'exposició inferior) i una resolució espectral de $\sim$80 km s^{-1}. Els temps d'observació es van seleccionar per tal que dues de les binàries eclipsants més brillants tinguessin, cadascuna d'elles, almenys dues observacions a les quadratures.

La reducció de les observacions va ser duta a terme amb el paquet IRAF de Gemini. Les imatges es van corregir de *bias* i de *flat-field*. Per realitzar el calibratge en longitud d'ona, vàrem utilitzar làmpades de calibratge (de coure i argó). Els espectres calibrats en longitud d'ona van ser corregits del fons de cel i extrets amb obertures d'entre un i dos segons d'arc. Els espectres resultants (Fig. 3.3) inclouen totes les línies de Balmer (excepte Hα a 656.3 nm) amb una relació senyal-soroll que arriba a 40 en el millor dels casos (Taula 3.2).

Seguint el mètode espectrofotomètric de determinació de distàncies (apartat 1.3.2), també vàrem aconseguir temps d'observació (al 2005) amb el telescopi espacial Hubble (HST). Les candidates seleccionades per obtenir-ne espectrofotometria (amb l'instrument ACS) eren dues de les binàries eclipsants observades amb GMOS (M31V J00443799+4129236 i M31V J00442326+4127082). Les observacions van ser finalment realitzades al 2006, però, degut a la fallada de l'ACS, només es varen obtenir dades completes (tres observacions en total) per a una de les dues candidates (Taula 3.4).

Donat que cadascuna de les observacions va ser obtinguda amb un prisma i un detector different (per cobrir el rang de longituds d'ona entre 115 i 1050 nm), la reducció de les dades és lleugerament different en cada cas. De tota manera, la reducció de *bias*, corrent fosc i *flat-fields* es realitza de forma automàtica. La resta de la reducció va ser realitzada, pas per pas, per nosaltres i consisteix, bàsicament, en corregir la deformació de camp (perquè els detectors utilitzats estan fora de l'eix òptic del HST), calibrar els espectres en longitud d'ona, restar el fons de

cel i extreure els espectres. Malauradament, una estrella veïna contamina un dels tres espectres de la binària eclipsant, fent que no es pugui utilitzar el tram entre 170 i 215 nm. A més a més, les transformacions a espectrofotometria estàndard introdueixen un error de l'ordre del 5% en els espectres observats. Així doncs, l'error de les observacions està, generalment, entre el 10 i el 20% (Fig. 3.4 a Fig. 3.7).

Binàries eclipsants

De les cinc binàries eclipsants observades amb GMOS, quatre tenen espectres amb una relació senyal-soroll suficient com per determinar-ne les propietats físiques. A continuació es presenta l'anàlisi de cadascuna d'elles. La distància a M 31 que se'n deriva es pot veure al final del present apartat.

M31V J00443799+4129236 (SB2A)

El primer pas per a la determinació de les propietats físiques és l'obtenció de les velocitats radials. De tota manera, en un sistema binari, els espectres dels dos components es troben combinats en un de sol i, per tant, cal un algoritme capaç de determinar la velocitat dels dos components a la vegada. Així doncs, vàrem utilitzar un programa de correlació creuada en dues dimensions (anomenat TODCOR, de Zucker & Mazeh, 1994). Com a espectres de referència (o patró) vàrem utilitzar els proporcionats pels models de TLUSTY (Lanz & Hubeny, 2003, 2007) i d'ATLAS9 de Kurucz.

Per aquesta binària eclipsant, les propietats dels espectres patró (temperatura, gravetat superficial, etc.) es van seleccionar, en primera instància, a partir de l'ajust preliminar de les corbes de llum. Un cop determinades les velocitats radials, els espectres de cada component es van separar per determinar-ne la temperatura dels components (apartat 4.1.1.3). Les temperatures determinades es van utilitzar per definir uns espectres patró amb més precisió i, d'aquests, trobar-ne les velocitats.

Un cop determinades les velocitats radials (Taula 4.2), ja es poden determinar les propietats físiques del sistema. Per a això vàrem utilitzar el programa de W&D. L'ajust de les corbes de llum i de velocitat radial es va fer de forma independent i iterativa fins a assolir una solució consistent amb totes les observacions. Les observacions inclouen no solament les obtingudes per nosaltres, sinó també les corbes en *V* de DIRECT. Els ajustos resultants es poden veure a la Fig. 4.2, i els paràmetres corresponents a la Taula 4.3. Cal destacar-ne la presència d'efecte O'Connell, que va ser modelitzat amb una taca brillant a la primària.

Per derivar-ne la distància, aquesta binària eclipsant encara necessitava una

determinació de la temperatura dels components. En aquest cas es van intentar dos procediments: modelització dels espectres i espectrofotometria.

Com ja s'ha comentat, en un sistema binari, l'espectre dels dos components es troba combinat en un de sol. Per tal de modelitzar l'espectre de cada component, primer cal separar-los. Per aquest motiu es va utilitzar el programa KOREL (Hadrava, 1995). Els espectres separats (Fig. 4.3) es van modelitzar amb models de TLUSTY, obtenint la temperatura, la velocitat de rotació, la magnitud absoluta dels components i, finalment, un mòdul de distància a M 31 de $(m - M)_0 = 24.44 \pm 0.12$ mag (Taula 4.4).

El segon procediment que es va intentar per determinar la temperatura d'aquesta binària eclipsant va ser el mètode espectrofotomètric. D'aquest sistema se'n va poder obtenir espectrofotometria amb el HST. De tota manera, de seguida es va fer evident que els errors en les observacions eren massa grans com per determinar-ne les propietats de forma fiable. Així doncs, es van fer servir les observacions per confirmar els resultats obtinguts a través de la modelització dels espectres. Per tal de fer la comprovació, es van imposar els valors obtinguts amb la modelització espectral i es va introduir una corba d'extinció mitjana de la Via Làctia. La distribució espectral d'energia derivada dels models és dins dels errors de les observacions (Fig. 4.4) i, per tant, l'espectrofotometria obtinguda està d'acord amb els resultats de la modelització espectral.

Un cop determinades les propietats físiques, vàrem determinar l'estadi evolutiu del sistema. Per això vàrem comparar les masses i els radis obtinguts amb els models evolutius de Lejeune & Schaerer (2001, Fig. 4.5) per a estrelles isolades. Els resultats obtinguts mostren que les dues estrelles són massa lluminoses per les seves masses i que el sistema està en un estadi de post-transferència de massa, en el que l'estrella originàriament més massiva és ara la secundària. A més a més, els resultats obtinguts mostren indicis d'una important transferència de massa (efecte O'Connell, velocitat de rotació de la primària, etc.) des de la secundària cap a la primària.

M31V J00443610+4129194 (SB2B)

Com en el cas de SB2A, el primer pas en l'anàlisi d'aquesta binària eclipsant va ser la determinació de les velocitats radials a partir dels espectres observats amb GMOS. Els models utilitzats per determinar-ne les velocitats radials amb TODCOR van ser, de nou, els models de TLUSTY i de Kurucz. De tota manera, la determinació dels espectres patró que proporcionaven millors velocitats radials va ser més iterativa. En aquest cas, vàrem buscar primer uns espectres patró a partir de l'ajust preliminar de W&D (amb corbes de llum). Un cop determinades les velocitats radials, vàrem realitzar un nou ajust de W&D i, a continuació, les noves propietats trobades, es van fer servir per trobar uns nous espectres patró.

El procés es va repetir fins que els espectres patró van ser els mateixos en dues iteracions.

Per trobar les masses i els radis vàrem utilitzar, de nou, el programa de W&D. Els procés seguit va ser similar al descrit anteriorment, però per aquesta binària eclipsant, van caldre diverses proves per tal d'identificar la configuració que millor podia explicar les observacions. Així doncs, en primer lloc, es va intentar modelitzar el sistema com a separat, però els resultats proporcionaven solucions on o bé la primària, o bé la secundària, omplien el lòbul de Roche. Així doncs, vàrem intentar dues solucions suposant que el sistema era semi-separat: una on la primària omplia el lòbul de Roche i l'altra on la secundària l'omplia. La principal diferència entre les dues solucions rau en el quocient de lluminositat que se'n deriva. Com es dedueix de la determinació de temperatures (apartat 4.1.2.3), la secundària és més feble que la primària, el que indica que és la primària, i no la secundària, la que omple el lòbul de Roche (Fig. 4.6).

La determinació de temperatues d'aquesta binària eclipsant es va fer a partir de la modelització dels espectres observats. El procés de modelització és igual que el descrit per a la SB2A. Cal destacar-ne el fet que l'espectre de la secundària és bàsicament soroll (Fig. 4.7). Això es pot explicar si es suposa que la secundària és més feble que la primària i, per tant, indica que la configuració on la primària omple el lòbul de Roche és la més probable. A l'espectre separat de la primària s'ha ajustat un model de TLUSTY per determinar-ne la temperatura, la gravetat superficial i la velocitat de rotació (Taula 4.7). Combinant tots els resultats vàrem derivar una segona distància a M 31 de $(m - M)_0 = 24.30 \pm 0.11$ mag.

Finalment, per tal d'acabar de caracteritzar el sistema, vàrem comparar les propietats observades amb els models evolutius de Lejeune & Schaerer (2001). En contra del que passa amb la binària SB2A, els components coincideixen amb les posicions predites pels models evolutius (Fig. 4.8) d'estrelles isolades. Això és característic de sistemes separats, però els ajustos obtinguts amb el W&D per a aquest sistema semblen indicar que la primaria omple el lòbul de Roche. Les observacions es poden explicar si es considera que el sistema es troba en un estadi evolutiu on la primària està a punt d'omplir el lòbul de Roche i on la transferència de massa encara no ha començat.

M31V J00444528+4128000 (SB1)

L'ajust prelimar de les corbes de llum, així com els espectres observats per a aquesta binària eclipsant, suggereixen que només es poden observar les línies espectrals d'un dels components. Així doncs, per tal de determinar les velocitats radials de la primària, es va fer servir un programa anomenat TIRAVEL (Zucker & Mazeh, 2006), on les velocitats radials (Taula 4.8) es determinen a partir del desplaçament relatiu de les línies i, per tant, no cal cap espectre patró.

A més a més de les velocitats radials, TIRAVEL també proporciona un espectre combinat que inclou tots els espectres observats. Aquest espectre es va utilitzar per realitzar una determinació de la temperatura, la gravetat superficial, la metal·licitat, la velocitat microturbulenta i la velocitat de rotació de la primària (Taula 4.9).

L'últim pas per determinar les propietats físiques del sistema és la determinació de la massa i del radi. De tota manera, com que només es tenen les velocitats radials de la primària, calen suposicions addicionals per tal de resoldre les propietats del sistema. En el nostre cas vàrem calcular el radi de la primària a partir de la temperatura observada (i d'una distància a M 31) i vàrem imposar que la solució obtinguda amb el W&D coincidís amb el radi calculat. L'ajust resultant es pot veure a la Fig. 4.10 i a la Taula 4.10. Cal destacar el fet que els residus observats indiquen clarament que almenys un dels components és intrínsecament variable.

En comparar els resultats amb els models evolutius (Lejeune & Schaerer, 2001, Fig. 4.11), es confirma una cosa que ja es podia observar a l'espectre combinat: que la primària és una supergegant blava. Pel que fa a la secundària, s'observa que és sublluminosa per la seva massa. De tota manera, les propietats de la secundària s'han deduït, bàsicament, a partir de les corbes de llum. Cal tenir present que aquestes presenten una variabilitat que no és tinguda en compte en errors proporcionats pel W&D. Així doncs, la diferència en la secundària pot no ser significativa si es té en compte la variabilitat del sistema.

M31V J00442326+4127082 (SB3)

L'últim sistema binari analitzat presenta diversos indicis a favor de la presència d'un tercer component (que pot correspondre a una o vàries estrelles). Així doncs, per determinar les velocitats radials d'aquest sistema, es va utilitzar un nou algoritme (desenvolupat a la Universitat de Tel Aviv i anomenat TRIMOR) que és capaç de realitzar correlació creuada amb tres components. De nou, es va utilitzar un procés iteratiu per determinar els espectres patró que proporcionaven millors velocitats radials (Taula 4.11).

Per a la determinació de les masses i els radis del sistema doble, es va realitzar, com en els casos anteriors, un ajust amb el W&D. Els resultats de l'ajust mostren un sistema molt interessant (Taula 4.12 i Fig. 4.13), ja que és excèntric, els seus components tenen masses per sobre de 40 $M_\odot$ i, a més, presenta moviment apsidal.

Els espectres dels components d'aquest sistema no es varen poder separar de l'espectre observat i, per tant, no vàrem poder determinar-ne una temperatura directa. De tota manera, considerant que els dos components del sistema es van formar a la vegada, vàrem poder realitzar una modelització del sistema a partir dels models evolutius de Lejeune & Schaerer (2001).

En primer lloc, vàrem utilitzar el diagrama massa-radi per determinar l'edat i la lluminositat dels dos components eclipsants (Fig. 4.14). A més a més, a partir de la tercera llum (derivada de les corbes de llum) també vàrem determinar les propietats del tercer component (suposant que es va formar al mateix temps que el sistema binari, Taula 4.13). Els paràmetres derivats són compatibles amb les línies espectrals observades als espectres de GMOS (Fig. 4.12) i, a més, permeten determinar un mòdul de distància a M 31 de $(m - M)_0 = 24.8 \pm 0.6$ mag.

Un cop determinades les propietats fonamentals dels components (massa, radi i temperatura), ja s'està en condicions d'analitzar l'origen del moviment apsidal. Cal dir que l'anàlisi presentat en aquest treball és preliminar i que cal, en un futur, una anàlisi més detallada. De tota manera, hi ha tres causes possibles pel moviment apsidal observat: la contribució de la terciària, els efectes relativistes i l'estructura interna dels components. Després de repassar cadascuna de les possibles contribucions, vàrem deduir que la causa més probable del moviment apsidal observat és l'estructura interna dels components. De tota manera, els models d'estructura estel·lar prediuen un moviment apsidal més gran que l'observat. Aquesta diferència es pot explicar si les estrelles tenen nuclis convectius més grans del què prediuen els models.

La distància a M 31 a partir de binàries eclipsants

Tres de les quatre binàries eclipsants estudiades (SB2A, SB2B i SB3), han proporcionat dades suficients com per permetre una determinació de la distància a M 31 (Taula 4.14). D'aquestes tres distàncies, dues són determinacions directes, ja que no depenen de cap calibratge previ. La distància proporcionada per SB3 es basa en models evolutius, els quals tenen un gran nombre de suposicions i, per tant, no es pot considerar directa. La mitjana de les dues distàncies directes dóna un mòdul de distància a M 31 de $(m - M)_0 = 24.36 \pm 0.08$ mag (744 ± 33 kpc).

Els errors de la distància calculada no tenen en compte una possible sistemàtica introduïda pels models d'atmosfera estel·lar (TLUSTY). De tota manera, per la nostra experiència, estimem que aquesta sistemàtica és inferior a 0.05 mag. Algunes vegades també s'ha argumentat que els sistemes que presenten una important deformació, degut a la proximitat entre els components, no són adequats per determinacions de distància. Aquesta afirmació no és del tot certa, ja que els possibles efectes de proximitat es veuen compensats per una reducció en el nombre de paràmetres lliures i, per tant, els sistemes semi-separats poden, igualment, ser utilitzats per a determinació de distàncies. Així doncs, les distàncies derivades són directes i precises.

Finalment, és important destacar que el procediment utilitzat en aquest treball ha compensat la manca d'espectrofotometria gràcies a la separació i modelització dels espectres de GMOS. Aquest nou procediment requereix menys observacions i, per tant, fa possible l'anàlisi d'un major nombre de binàries eclipsants.

Cefeides

El primer que es pot estudiar de la mostra de 416 Cefeides detectades en el catàleg d'estrelles variables és la distribució de períodes. El primer que vàrem fer va ser comparar la distribució de períodes de les Cefeides observades amb aquelles conegudes a M 31 del catàleg GCVS (Fig. 5.1). Es va observar com els dos catàlegs són clarament diferents degut, bàsicament, a una manca de Cefeides de períodes curts (i febles) al GCVS. Posteriorment es va observar com la distribució de períodes de les Cefeides observades és molt similar a l'obtinguda pel catàleg DDO, on hi ha Cefeides de la nostra galàxia. Així doncs, es va deduir que el catàleg de Cefeides obtingut és tant complet com el catàleg DDO i, a més, que les distribucions de períodes de les Cefeides són similars en les dues galàxies.

El següent pas en l'anàlisi de les Cefeides observades va ser la seva classificació polsacional. És a dir, seleccionar les Cefeides en funció de si polsen en el mode fonamental o en algun dels seus harmònics. Aquesta classificació es pot realitzar mitjançant l'ajust d'una sèrie de Fourier a les corbes de llum i observant la relació entre els coeficients dels primers ordres. En total vàrem poder classificar 315 Cefeides: 240 polsant en el mode fonamental i 75 polsant en el primer harmònic (Fig. 5.2). A més a més, totes les Cefeides amb un període superior a 8 dies es va considerar que polsaven en el mode fonamental (fent un total de 281 Cefeides en el mode fonamental), ja que no hi ha Cefeides polsant en el primer harmònic amb un període superior a 7 dies.

Un cop classificades les Cefeides vàrem procedir a estudiar la relació P-L. La relació obtinguda amb la mostra de Cefeides fonamentals mostra una gran dispersió (Fig. 5.4) deguda a tres possibles factors: absorció, efectes de metal·licitat i de contaminació.

Per tal de corregir l'efecte d'absorció, vàrem utilitzar relacions període-color del grup OGLE (Udalski et al., 1999). Un cop determinats els colors $(B-V)_0$, vàrem determinar l'absorció de cada Cefeida utilitzant un coeficient d'extinció total respecte extinció parcial ($\mathcal{R}_V$) estàndard.

Per tal de corregir l'efecte que la metal·licitat té en la magnitud absoluta de les Cefeides, en primer lloc vàrem utilitzar un gradient galactocèntric (Zaritsky et al., 1994) per estimar la metal·litat de les Cefeides. A continuació, vàrem aplicar una correcció a la magnitud de cada Cefeida (Sakai et al., 2004), segons la metal·licitat derivada.

L'últim possible effecte és la contaminació per estrelles veïnes. A la distància de M 31, la resolució angular de les imatges obtingudes amb el INT correspon a uns 4 pc. Així doncs, el que sembla una sola Cefeida pot contenir la contribució de diverses estrelles. Així doncs, vàrem desenvolupar un mètode per determinar el valor de la contaminació introduïda per altres estrelles en la magnitud de les Cefeides observades. El procés es basa en el fet que l'amplitud d'una Ce-

feida sempre disminueix quan hi ha estrelles contaminants i que la relació entre l'amplitud d'una Cefeida en dos filtres (B i V) és aproximadament constant.

Els resultats obtinguts per a cada Cefeida tenen un error molt important, fent impossible la determinació de la contaminació en cada Cefeida. De tota manera, el gran nombre de Cefeides estudiades va permetre la determinació d'un valor mig de la contaminació (Taula 5.1). Els resultats mostren que l'efecte de la contaminació en la magnitud mitjana d'una Cefeida és de l'ordre de 0.2 mag. El mateix valor va ser observat per altres autors a M 33 i, a més, s'observa un valor similar per la tercera llum de les 24 binàries eclipsants seleccionades com a bones candidates per a la determinació de distàncies.

L'efecte que la contaminació sempre disminueixi l'amplitud de les Cefeides va ser utilitzat per seleccionar aquelles Cefeides menys afectades. Així doncs, vàrem seleccionar les 66 Cefeides amb una amplitud major que 0.8 mag per determinar una distància a M 31. Basant-nos en les relacions P-L de OGLE i un mòdul de distància a LMC de $(m - M)_0 = 18.42 \pm 0.06$ mag, el mòdul de distància a M 31 resultant és de $(m - M)_0 = 24.32 \pm 0.12$ mag.

Resultats i conclusions

Un cop presentat l'anàlisi realitzada i presentats els resultats, cal comparar les diferents determinacions i posar-les en context amb el coneixement actual de la matèria.

La distància a M 31 en context

En primer lloc, cal dir que la determinació directa de la distància a M 31 (objectiu principal del projecte) s'ha assolit. El valor obtingut de $(m - M)_0 = 24.36 \pm 0.08$ mag és directe, ja que no es basa en cap determinació prèvia de distàncies; acurat, ja que s'han utilitzat dues binàries eclipsants amb característiques diferents i s'han tingut en compte les possibles sistemàtiques; i precís, ja que el valor obtingut té només un 4% d'error.

El valor obtingut està completament d'acord amb les determinacions indirectes obtingudes prèviament a M 31, el què demostra el correcte calibratge de la majoria de candeles estàndard. El valor obtingut amb les Cefeides també està perfectament d'acord amb el valor de les binàries eclipsants. Aquest fet té una conseqüència important, ja que la distància de les Cefeides està basada en una determinació de la distància a LMC amb binàries eclipsants. Així doncs, la distància obtinguda no només és consistent amb altres indicadors de distància, sinó que és consistent amb altres determinacions de distàncies amb binàries eclipsants.

Resultats més destacats

La recerca de binàries eclipsants a M 31, realitzada amb el telescopi INT, va proporcionat un extensiu catàleg fotomètric. L'anàlisi de les observacions va revelar 3 964 estrelles variables, 437 de les quals són binàries eclipsants i 416 són Cefeides. La gran precisió de la fotometria obtinguda, amb 37 241 objectes amb un error inferior a 0.1 mag, i el gran nombre d'estrelles variables (amb 3 000 d'elles sense identificar) representa una base de dades excel·lent per futures anàlisis a M 31.

Les binàries eclipsants identificades es van seleccionar, proporcionant una llista de 24 candidates idònies per a la determinació de la distància a M 31. D'aquestes, se'n van observar 5 amb el telescopi Gemini-North. L'aplicació de nous algoritmes de correlació creuada va proporcionar velocitats radials per a quatre d'elles. Addicionalment, els algoritmes utilitzats van permètre la separació dels espectres de cada component per determinar les propietats físiques dels sistemes binaris (temperatura, gravetat superficial, etc.) mitjantçant ajustos espectrals.

Per dues de les binàries amb velocitats radials es va aconseguir temps d'observació espectrofotomètrica amb el Hubble Space Telescope, però la qualitat de les dades obtingudes són insuficients per tal de determinar una distància a M 31 mitjançant un mètode espectrofotomètric. Així doncs, caldrà esperar a futures missions per poder aplicar aquest mètode.

La modelització de les binàries eclipsants observades amb Gemini-North va permetre la determinació directa de les masses i els radis de quatre sistemes binaris. Tots ells tenen propietats que els fan extremadament interessants per entendre millor les propietats físiques d'estrelles massives. En particular l'anàlisi realitzada ha permès identificar una de les binàries (SB2A, M31V J00443799+4129236) com un sistema tipus Algol, on els seus components són més brillants del què prediuen els models degut a la intensa transferència de massa. Un altre dels sistemes binaris (SB2B, M31V J00443610+4129194) està format per dues estrelles separades (on la primària gairebé omple el lòbul de Roche) permetent una determinació de l'edat del sistema binari. La tercera binària eclipsant (SB1, M31V J00444528+4128000) és un sistema evolucionat on la secundària omple el lòbul de Roche, fent-lo molt interessant per estudiar la transferència de massa en aquests sistemes. Finalment, una de les binàries eclipsants analitzades (SB3, M31V J00442326+4127082) ha demostrat ser un sistema supermassiu amb moviment apsidal, permetent un primer anàlisi de l'estructura interna en estrelles de més de 40 masses solars.

Addicionalment, les Cefeides detectades al catàleg fotomètric es van analitzar, permetent determinar que la mostra obtinguda és tant completa com el catàleg DDO de la Via Làctia. La gran qualitat de les corbes de llum va permetre identificar 281 Cefeides polsant en el mode fonamental i 75 en el primer harmònic. L'exhaustiu anàlisi realitzat de la relació període-lluminositat i el de-

senvolupament d'un nou mètode per calcular la contaminació per estrelles veïnes va mostrat com l'efecte de la contaminació és tant important com la correccio de la metal·licitat per determinar distàncies amb Cefeides.

Finalment, les binàries eclipsants van proporcionar un mòdul de distància a M 31 de $(m - M)_0 = 24.36 \pm 0.08$ mag (744 ± 33 kpc). Aquest resultat és compatible amb les determinacions prèvies de la distància a M 31, demostrant que els indicadors de distància estan ben calibrats. A més, la distància obtinguda a partir de les Cefeides demostra que el resultat és compatible també amb la determinació de la distància a LMC amb binàries eclipsants. Així doncs, el present treball demostra que les binàries eclipsants són excel·lents indicadors de distància i obre la porta a futures determinacions de distància a altres galàxies del Grup Local.

Apèndix: gran fulguració estel·lar

Com a mostra del gran potencial que té el catàleg fotomètric obtingut, a continuació es detalla l'anàlisi d'una fulguració estel·lar del dia 25 de setembre de 2000 i que vàrem descobrir durant el procés de reducció.

Les fulguracions estel·lars s'observen en estrelles magnèticament actives com, per exemple, el Sol. En general, les fulguracions poden emetre entre 10^{30} i 10^{32} ergs i són especialment comunes en estrelles fredes. En estrelles M, aquestes fulguracions solen ser especialment intenses en l'òptic, mentre que tendeixen a ser observades en el rang UV i de rajos X en les estrelles més calentes.

L'estrella que presenta la fulguració estel·lar es troba identificada, en el catàleg de referència, com a M31 J00453912+4130395. Aquesta estrella també té fotometria de DIRECT i de 2MASS (Skrutskie et al., 2006). Tenint en compte totes aquestes observacions, es pot estimar que l'estrella és una nana de tipus espectral M4 i que es troba situada a uns 300 pc.

L'anàlisi dels 5 anys de sèries fotomètriques obtingudes no presenta clars signes de variabilitat fora del període amb fulguració (Fig. A.2), el què indica que l'estrella té taques relativament poc importants o repartides de forma homogènia.

Per tal de determinar l'energia emesa durant la fulguració, en primer lloc, es pot observar que la durada de la fulguració és de l'ordre de 30 000 segons. Això classifica aquesta fulguració dins el grup de les més intenses, amb energies de l'ordre de 10^{32} ergs. Addicionalment, es pot calcular l'energia emesa tot integrant la variació de lluminositat durant la fulguració i multiplicant-la per l'energia de l'estrella en l'estadi quiescent. Els resultats mostren que la fulguració observada és de les més intenses que mai s'han observat (Taula A.2).

Juntament amb la fulguració principal, també es van observar cinc fulguracions menors, amb durades d'uns 8 000 segons. Tres d'aquestes fulguracions van

ser observades durant la decreixença de la fulguració principal. Aquests fenòmens són observats també en altres casos i es poden explicar com reconexions magnètiques, degudes al mecanisme proposat per Attrill et al. (2007).

1 Introduction

1.1 The extragalactic distance ladder

Distance determinations are based on a hierarchic procedure where the closest distance indicators are used to calibrate farther distances. This process has been commonly known as the distance scale or the distance ladder, in the same way that the first rungs of a ladder are used to reach further steps. The first rung of the distance ladder is the Astronomical Unit, which can be determined by a wealth of different methods and procedures, either direct or indirect. With the determination of the Astronomical Unit and with accurate astrometric parallaxes, the distance to neighboring stars can be directly determined.

The most accurate and wide survey of astrometric parallaxes was obtained by the Hipparcos satellite (launched in 1989), which observed ~120 000 stars with an *absolute* parallax precision between 1 and 10 milliarcsec (Perryman & ESA, 1997; van Leeuwen, 2007). In the future, the Gaia mission is expected to greatly improve Hipparcos determinations, with a precision between 4 and 200 microarcsec for 10^9 stars (Perryman et al., 2001).

Geometric distance determination through parallaxes (with the exception of orbital parallaxes, see Herrnstein et al., 1999, as an example) is almost the only purely direct method. All the remaining distance determinations are based (to some extent) on the knowledge of the intrinsic luminosity of certain objects (usually referred as standard candles). Unfortunately, precise trigonometric parallax determinations (with errors below 10%) can only be obtained for the closest stars (~100 pc with Hipparcos). Therefore, as a new rung in the distance ladder, the trigonometric parallaxes are used to calibrate the luminosities of stars.

The number of photometric distance indicators is very large (see Jacoby et al., 1992, for a critical review), each one being suitable for certain distance intervals (Fig. 1.1). In all cases, the distance is obtained by knowing the intrinsic luminosity of the studied object (L_λ) at a certain wavelength λ and comparing it with the

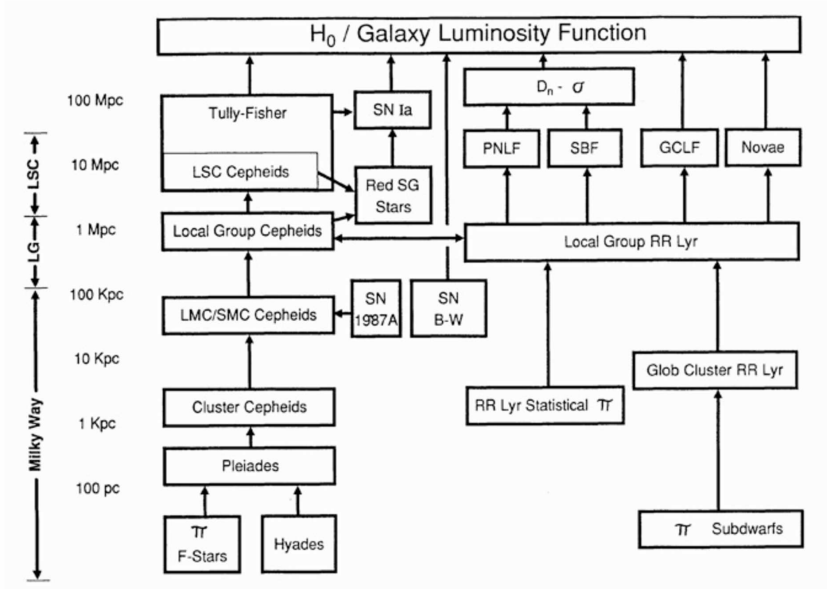

Figure 1.1. Distance determination techniques as described in Jacoby et al. (1992). The used abbreviations stand for: LSC — Local Super Cluster; SG — Supergiant; SN — Supernovae; B-W — Baade-Wesselink; PNLF — Planetary-Nebula Luminosity Function; SBF — Surface-Brightness Fluctuations; GCLF — Globular-Cluster Luminosity Function; π — astrometric parallax.

observed (absorption corrected) flux ($f^{\oplus}_{0,\lambda}$) through the expression known as the inverse square law of distance

$$f^{\oplus}_{0,\lambda} = \frac{L_\lambda}{4\pi d^2} \tag{1.1}$$

where d is the distance to the object of known luminosity. Equivalently, the distance can also be expressed in terms of the absolute magnitude (M_λ) of the object from the definition of the distance modulus

$$(m - M)_0 \equiv m_{0,\lambda} - M_\lambda = 5\log(d) - 5 \tag{1.2}$$

where $m_{0,\lambda}$ is the (absorption corrected) magnitude of an object at d parsecs.

Among all the standard candles, Cepheids play a central role in the distance ladder (Fig. 1.1). Cepheids are evolved variable stars (of spectral class F6 to K2) that pulsate radially (with periods ranging from ∼1 to ∼50 days). These variable stars have large amplitudes and bright intrinsic luminosities that make them easily detectable in photometric variability surveys, even in distant galaxies. In addition,

they present a strong correlation between the period of pulsation and their absolute magnitude (known as period-luminosity relationship, Leavitt & Pickering, 1912). The Cepheid period-luminosity (P-L) relationship has made of these variable stars one of the main cornerstones in deriving extragalactic distances (see Freedman et al., 2001, for a review).

The pulsation mechanism is relatively well understood from the theoretical point of view (see Gautschy & Saio, 1996, for a review). However, the large number of required assumptions has made that, in most cases, the calibration of the P-L relationship has been obtained empirically. The zero-point of the P-L relationship has been established from several distance indicators, such as the Hipparcos statistical parallaxes of Cepheids (Feast & Catchpole, 1997; Luri et al., 1998), from isochrone fitting to galactic open clusters and from the infrared surface brightness technique (Gieren et al., 1997). The slope of the P-L relationship has traditionally been obtained from extragalactic Cepheids. The largest effort in this sense has been performed by the OGLE group (Udalski et al., 1999), identifying $\sim$ 1300 Cepheids in the Large Magellanic Cloud (LMC).

The Large Magellanic Cloud has traditionally been used as the first extragalactic rung of the distance ladder because of its proximity to the Milky Way. However, its low metallicity and irregular geometry (see, i.e., Weinberg, 2000) has posed some doubts on the suitability of LMC as the first step of the extragalactic distance ladder, as illustrated by the large spread in distances (Fig 1.2) derived from different methods (Gibson, 2000).

Therefore, accurate distance measurements to other Local Group galaxies are crucial to calibrating the cosmic distance scale. Once Local Group galaxy distances are known, all of its various stellar populations are available as potential standard candles. As major rungs on the cosmic distance ladder, these galaxies serve as calibrators not only for Cepheids but also for novae, supernovae, globular clusters, etc., reaching far beyond the bounds of the Local Group (Hodge, 1981). In addition, precise distance determinations to Local Group galaxies enable the calibration of cosmological distance determination methods, such as supernovae, Tully-Fisher relationship, surface brightness fluctuations, etc. A precise and accurate determination of the extragalactic distance ladder is crucial to understand the physics, the age and the size of the Universe.

1.2 The Andromeda Galaxy

The Andromeda galaxy (M 31) is the nearest external spiral galaxy (Sb; Hubble, 1929) and, with the Milky Way, one of the two largest galaxies in the Local Group. Since the pioneering work of Hubble (1929), a large variety of studies have been performed to investigate its structure and stellar content. A clear example of the structure of M 31 can be seen in Gordon et al. (2006), where infrared observa-

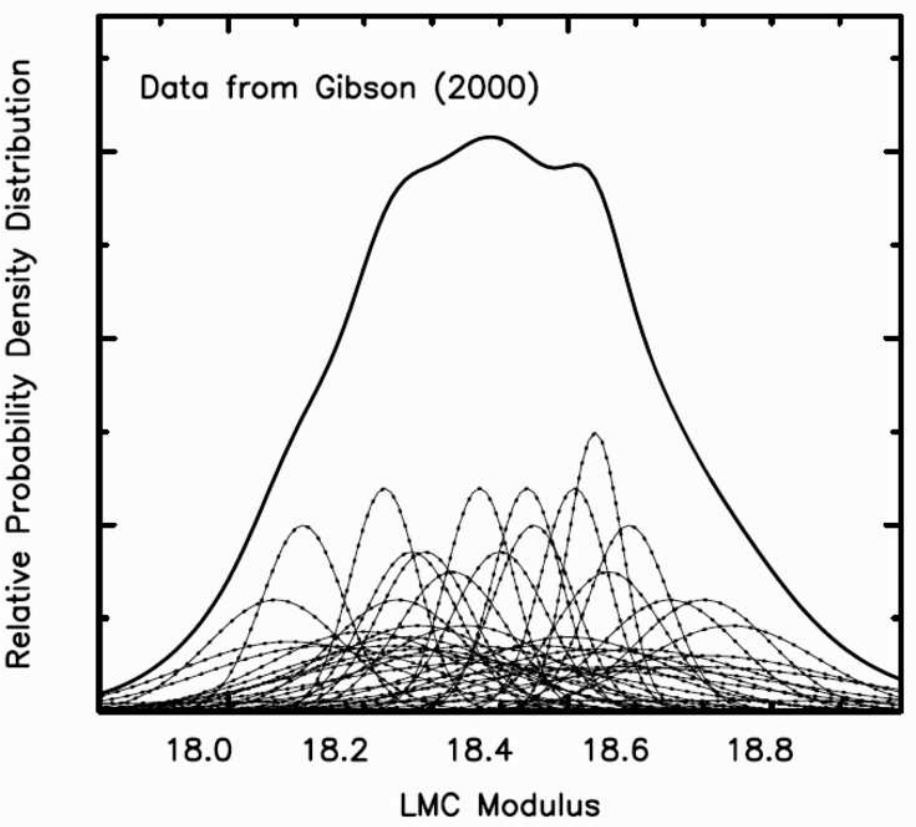

Figure 1.2. Frequentist probability density presented in Freedman et al. (2001); distribution of LMC distance moduli as compiled by Gibson (2000) plotted as a continuous probability density distribution built from the sum of individual unit-area Gaussians centered at the modulus in several works, and broadened by the published internal random error.

tions revealed its complex spiral structure, probably due to interactions with its numerous satellite galaxies. Other studies have revealed a rich stellar population (Massey, 2003) with all types of massive stars (e.g. main sequence stars, Wolf-Rayets, Luminous Blue Variable stars, Red Supergiants, etc). The analysis of its stellar population (and emission nebulae) has revealed that the metallicity of M 31 is very similar to that of the Milky Way. In addition, the similarity in size and morphology makes M 31 an ideal target to study spiral galaxy characteristics, allowing a better understanding of our own galaxy.

M 31 can also be a first-class distance calibrator (Clementini et al., 2001). On the one hand, and contrary to the Magellanic Clouds, the distance to M 31 is large enough so that its geometry does not introduce any systematics in the final distance determination. On the other hand, typically with a moderate reddening value ($E(B-V) = 0.16 \pm 0.01$, Massey et al., 1995), it is close enough to enable the individual identification of stars suitable for distance determination (such as

Cepheids). Moreover, an Sb I–II giant spiral galaxy (like M 31) provides a much more appropriate local counterpart for the galaxies commonly used for distance determination (e.g., Freedman et al., 2001). Finally, M 31 can also provide an absolute calibration of the Tully-Fisher relationship, enabling the calibration of the furthest distance determination methods. Therefore, although stars in M 31 are about six magnitudes fainter than those in LMC, the characteristics of this spiral galaxy make it a promising step of the cosmic distance scale.

Many studies have provided distance determinations to M 31 using a wide range of methods. A comprehensive list of distance determinations to M 31 are shown in Table 1.1 with explicit errors. As can be seen, the values listed are in the range $(m - M)_0$=24.0–24.6 mag. Most of the distance determinations in Table 1.1 rely on previous calibrations using stars in the Milky Way or the Magellanic Clouds. As a consequence of this, a large number of subsequent distance determinations, based only on recalibrations, can be found in the literature. These are not included in Table 1.1. The resulting weighted standard deviation is 0.08 mag (~4% in distance). As can be seen in Fig. 1.3 (where the range in distance modulus is the same that in Fig. 1.2), the dispersion is smaller than the dispersion in LMC distances, revealing that M 31 is potentially a better target to anchor the extragalactic distance scale. Therefore, a direct distance determination to M 31 (i.e., free from any prior calibrations) is of central importance to enable the use of this galaxy as the first step of the extragalactic distance ladder.

1.3 Eclipsing binaries

Eclipsing binaries (EBs) have always been an important tool for testing and determining the physical properties of stars (Popper, 1967; Guinan, 1993). They are composed of two stars that, when orbiting each other, produce periodic eclipses. The great potential of EBs is that their orbital motion, inferred from the radial velocity curves, and the shape of eclipses, obtained from the light curves, can be entirely explained by the gravitation laws and the geometry of the system (see Hilditch, 2001, for details).

Specifically, the light curves provide the relative properties and the orbital properties of the system (Table 1.2). The radial velocity curves can provide the systemic velocity (i.e., the velocity of the center of mass) and the velocity semi-amplitudes (i.e., the maximum velocity deviation of each component with respect to the systemic velocity). With these quantities, the semi-major axis of the system (a) and the individual mass of each component ($\mathcal{M}_P$, $\mathcal{M}_S$) can be determined from the following expressions (see Table 1.2 for nomenclature):

$$a \sin i = \frac{P(K_P + K_S)\sqrt{1 - e^2}}{2\pi} \tag{1.3}$$

Table 1.1. Distance determinations to M 31 as presented in the references. Values resulting from recalibrations of the same observational data, distance moduli without extinction corrections and distances derived in the present work are not included.

Method	$(m-M)_0$ [mag]	Distance [kpc]	Reference
Cepheids	24.20±0.14	690±40	[1]
Tip of the RGB	24.40±0.25	760±90	[2]
Cepheids	24.26±0.08	710±30	[3]
RR Lyrae	24.34±0.15	740±50	[4]
Novae	24.27±0.20	710±70	[5]
Cepheids	24.33±0.12	730±40	[6]
Cepheids	24.41±0.09	760±30	[6]
Cepheids	24.58±0.12	820±50	[6]
Carbon-rich stars	24.45±0.15	780±50	[7]
Cepheids	24.38±0.05	752±17	[8]
Carbon-rich stars	24.36±0.03	745±10	[8]
Glob. Clus. Lum. Func.	24.03±0.23	640±70	[9]
Red Giant Branch	24.47±0.07	780±30	[10]
Red Clump	24.47±0.06	780±20	[11]
Red Giant Branch	24.47±0.12	780±40	[12]
Cepheids	24.49±0.11	790±40	[13]
RR Lyrae	24.50±0.11	790±40	[14]
Tip of the RGB	24.47±0.07	785±25	[15]
Mean & std. deviation	24.39±0.08	750±30	

[1]: Baade & Swope (1963); [2]: Mould & Kristian (1986); [3]: Welch et al. (1986); [4]: Pritchet & van den Bergh (1987); [5]: Capaccioli et al. (1989); [6]: Freedman & Madore (1990); [7]: Richer et al. (1990); [8]: Brewer et al. (1995); [9]: Ostriker & Gnedin (1997); [10]: Holland (1998); [11]: Stanek & Garnavich (1998); [12]: Durrell et al. (2001); [13]: Joshi et al. (2003); [14]: Brown et al. (2004); [15]: McConnachie et al. (2005).

$$\mathcal{M}_P \sin^3 i = \frac{PK_S(K_P + K_S)^2(1-e^2)^{3/2}}{2\pi G} \tag{1.4}$$

$$\mathcal{M}_S \sin^3 i = \frac{PK_P(K_P + K_S)^2(1-e^2)^{3/2}}{2\pi G} \tag{1.5}$$

However, as can be seen from these equations, the inclination of the system, is needed for deriving the individual masses of the components and the semi-major axis. To obtain the inclination of the system, the light curves have to be modeled. The detailed modeling of the light curves involves a comprehensive understanding on the physical laws governing both the geometry of an EB system (usually de-

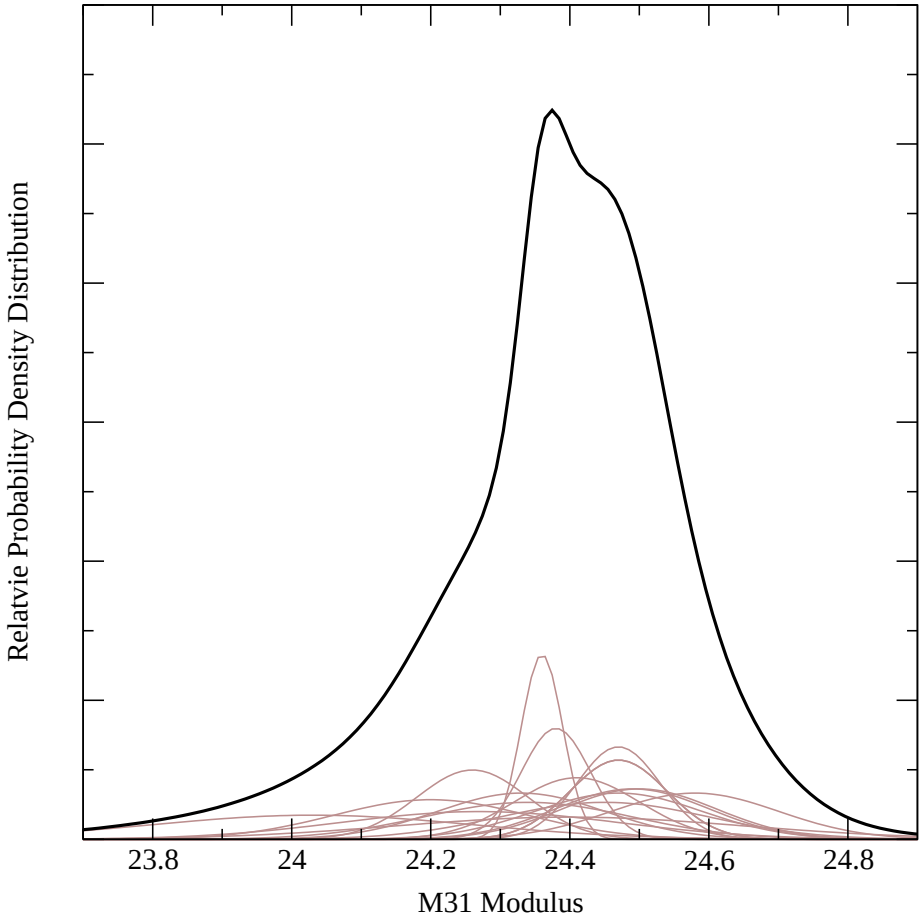

Figure 1.3. Distribution of M 31 distance moduli as compiled in Table 1.1 plotted as a continuous probability density distribution (black line) built from the sum of individual unit-area Gaussians centered at the quoted modulus, and broadened by the published internal random error (gray lines).

termined by the Roche lobe model) and the radiative properties of stars (including limb darkening, gravity brightening, reflection effects, etc.). The great number of processes involved in the light curve modeling has made that some specific algorithms, such as EBOP (Popper & Etzel, 1981) and the one by Wilson & Devinney (1971), have been developed to model the EB light curves. However, in all cases, the great number of involved parameters makes that expertise in modeling EBs is a necessary ingredient. In particular, the knowledge of possible correlations among parameters and the fundamental reasons for the observed correlations must be well understood to achieve an accurate solution. It is in this scenario when reducing the number of free parameters can be the proper way towards an accurate EB modeling.

In the course of the present work (Chap. 2 and Chap. 4), several assumptions are made to reduce the number of free parameters. The most important assumption

Table 1.2. EB properties that can be derived from different data sets. P and S stand for primary and secondary components, respectively, and a is the semi-major axis.

Parameter	Symbol	Light curves	Radial velocity curves	
			Single lines	Double lines
Period	P	✓	✓	✓
Eccentricity	e	✓	✓	✓
Argument of periastron	ω	✓	✓	✓
Luminosity ratio	L_λ^S/L_λ^P	✓	✗	✗
Inclination	i	✓	✗	✗
Radius of primary	R_P	$r_P = R_P/a$	✗	✗
Radius of secondary	R_S	$r_S = R_S/a$	✗	✗
Systemic velocity	γ	✗	✓	✓
Semi-amplitude of primary	K_P	✗	✓	✓
Semi-amplitude of secondary	K_S	✗	✗	✓

relates to the configuration of the system. In the Roche lobe model (see Hilditch, 2001, and references therein), the shapes of stars are determined by their surface potential. When the surface potential of a star is close to a certain limit (that depends basically on the mass ratio and the semi-major axis of the system), the star fills its Roche lobe. At this point, the surface layers of the star can flow out and accrete on the companion star. With this scenario, and depending on the value of the surface potential, the EB systems can be classified as (Fig. 1.4):

- Detached. Both stars are bound within separate equipotential surfaces. In this configuration the properties of every star is roughly independent on the presence of its companion.
- Semi-detached. Only one of the stars fills the Roche lobe (the companion is within a separate equipotential surface). In this configuration the shape of the component filling the Roche lobe is greatly distorted by the presence of its companion. In addition, the system can experience active mass transfer, implying that the evolution of both stars can depart from that of an isolated star.
- Over-contact. Both stars overfill their Roche lobes and share a common envelope. Therefore, their evolution and structure is closely coupled.

The adoption of a configuration can, therefore, reduce the number of free parameters. However, the final decision on the configuration adopted has to be well sustained by several indicators, including some tests with various possible configurations.

Another important consideration to accurately model an EB system is that, to

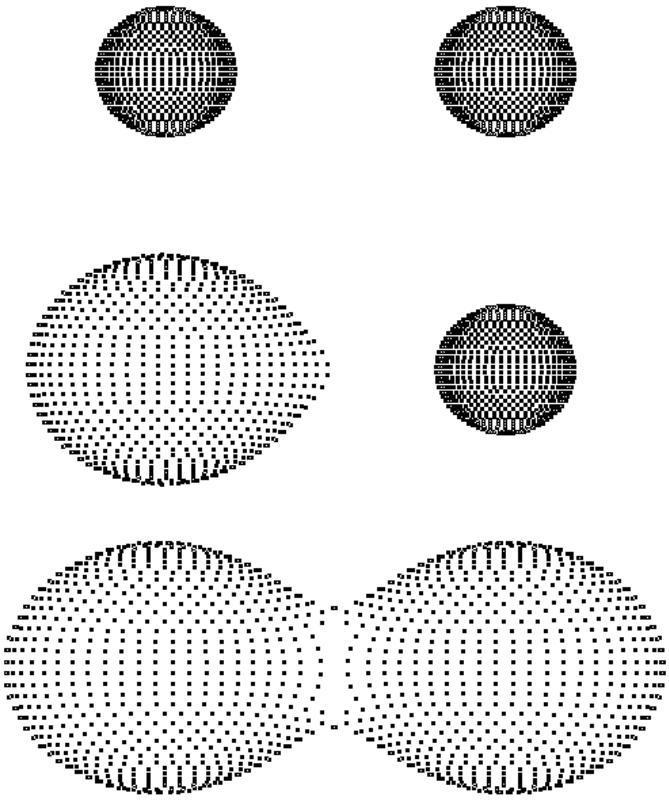

Figure 1.4. Diagram illustrating three possible configurations of an EB system. **Top:** Detached. **Middle:** Semi-detached. **Bottom:** Over-contact.

obtain the radial velocities, spectral lines have to be visible in the spectra. This leads to two possible scenarios:

- When the two components of the system have different luminosities and the lines of only one of them can be observed (called single-line binaries), the radial velocities can only provide the semi-amplitude of one of the components. In these systems, only a limited set of properties can be determined.
- When the luminosities of both components are similar, the spectroscopic lines of each component can be distinguished in the observed spectra. In these systems (called double-line binaries), all the orbital and physical quantities can be directly obtained (Table 1.2).

Therefore, for double-line EBs, the combination of light and radial velocity curves provides direct determinations of the individual radii and masses of the components without any prior calibration. However, a careful examination on the possi-

ble correlations and a detailed analysis of the minimum number of free parameters is required.

1.3.1 Distance determination methods

The direct determination of the radii (R) of the components of EB systems made that several authors (e.g., Lacy, 1977; Giménez et al., 1994) suggested the possibility to use EBs for deriving distances. The only additional requirement to determine the absolute luminosity of an EB system and, hence the distance, is the surface brightness (F_λ) or, equivalently, the effective temperature of the components ($T_{\rm eff}$).

The method of Lacy (1977) involves the use of the Barnes & Evans (1976) relationship to compute the surface brightness of the components. The distance modulus (Eq. 1.2) to each component is then computed assuming that the stars are roughly spherical ($L_\lambda = 4\pi R^2 F_\lambda$) through the expression

$$(m - M)_0 = m_\lambda - A_\lambda + 2.5 \log\left(\frac{R^2 F_\lambda}{R_\odot^2 F_{\lambda,\odot}}\right) - M_{\lambda,\odot} \tag{1.6}$$

with m_λ being the observed magnitude at a certain wavelength and A_λ being the line-of-sight absorption. In the equation above, the absolute magnitude ($M_\lambda = -2.5\log(L_\lambda) + C_\lambda$) is expressed in terms of the solar properties ($R_\odot^2$, $F_{\lambda,\odot}$ and $M_{\lambda,\odot}$) to avoid numerical constants (C_λ).

Afterwards, Giménez et al. (1994) suggested the use of multi-band photometry and UV spectroscopy to better determine the temperature of each component. The distance modulus could then be computed from the definition of effective temperature

$$M_{\rm bol} = -2.5 \log\left(\frac{R^2 T_{\rm eff}^4}{R_\odot^2 T_{\rm eff,\odot}^4}\right) + M_{\rm bol,\odot} = M_\lambda + BC_\lambda \tag{1.7}$$

$$(m - M)_0 = m_\lambda - A_\lambda - M_{\rm bol,\odot} + 2.5 \log\left(\frac{R^2 T_{\rm eff}^4}{R_\odot^2 T_{\rm eff,\odot}^4}\right) + BC_\lambda \tag{1.8}$$

with BC_λ being the bolometric correction at a certain wavelength. The equation above is usually expressed for the V passband

$$(m - M)_0 = m_V - A_V - M_{\rm bol,\odot} + 5 \log\left(\frac{R}{R_\odot}\right) + 10 \log\left(\frac{T_{\rm eff}}{T_{\rm eff,\odot}}\right) + BC_V \tag{1.9}$$

and the absorption is usually determined from a color index (e.g., $(B-V)$) through the expression

$$A_V = \mathcal{R}_V E(B - V) = \mathcal{R}_V \left[(B - V) - (B - V)_0\right] \tag{1.10}$$

where $\mathcal{R}_V \equiv A_V/E(B-V)$ is the total-to-selective extinction ratio, usually assumed to be $\mathcal{R}_V = 3.1$ (e.g., Fitzpatrick, 1999).

The great advantage of this method with respect to other methods is that the required quantities can be obtained from the binary analysis (R) and from stellar atmosphere models ($T_{\rm eff}$, $(B-V)_0$ and BC_V). Therefore, no empirical calibration is needed to obtain the distance to the EB (calibrations to transform the stellar models into the above quantities are still required), making that the distance determination to any EB system is almost direct (Clausen, 2004). In addition, the luminosities of both components can be checked against the luminosity ratio derived from the light curve analysis (Table 1.2), resulting in a solution that is not only direct, but also auto-consistent.

1.3.2 The experience of LMC

The potential of EBs to derive distances, encouraged a project to obtain a direct distance determination to the LMC. The possibility to obtain ultraviolet to visible spectrophotometry (with the Hubble Space Telescope, HST) allowed the use of a specific temperature determination method. The spectrophotometric method is based on Eq. (1.1) and considers that the luminosity of a binary system (with components P and S) can be expressed as:

$$L_\lambda = 4\pi \left(R_P^2 k^P F_\lambda^P + R_S^2 k^S F_\lambda^S \right) \tag{1.11}$$

$$f_\lambda^\oplus = \left(\frac{R_P}{d}\right)^2 \left[k^P F_\lambda^P + k^S \left(\frac{R_S}{R_P}\right)^2 F_\lambda^S \right] 10^{-0.4 A_\lambda} \tag{1.12}$$

where the absorption has been included. In order to consider the possibility that both components can be distorted by the presence of the companion star, a phase-dependent factor ($k^{P,S}$) has been introduced to consider the apparent size variations of the star (as seen from the Earth) and the reflection of light from the companion. Expressing the absorption in terms of the normalized extinction curve ($k(\lambda - V) \equiv E(\lambda - V)/E(B-V)$, Fitzpatrick, 1999) the equation above can be expressed as

$$f_\lambda^\oplus = \left(\frac{R_P}{d}\right)^2 \left[k^P F_\lambda^P + k^S \left(\frac{R_S}{R_P}\right)^2 F_\lambda^S \right] 10^{-0.4 E(B-V)[k(\lambda-V)+\mathcal{R}_V]} \tag{1.13}$$

In the equation above, the surface fluxes $F_\lambda^{P,S}$ are obtained from atmosphere models. The distance is then calculated by finding the best fitting model spectra and normalized extinction curve to the spectrophotometry measured at the Earth ($f_\lambda^\oplus$).

Four EBs have been used up to now to determine accurate distances to the LMC using the method described above (Table 1.3). Light curves were obtained from previous photometric surveys using 1–1.5 m telescopes, and radial velocities

Table 1.3. Distance determinations to LMC as presented in Fitzpatrick et al. (2003). The two distances to LMC provided for each EB (depending on two different orientations of LMC) have been averaged.

System	d_{EB} [kpc]	d_{LMC} [kpc]	$(m-M)_{0,LMC}$ [mag]	Reference
HV 2274	47.0±2.2	46.5	18.3	[1],[2]
HV 982	50.2±1.2	50.7	18.5	[2]
EROS 1044	47.5±1.8	47.4	18.4	[3]
HV 5936	43.2±1.8	44.4	18.2	[4]
Weighted mean		48.3 ± 1.4	18.42 ± 0.06	

[1]: Guinan et al. (1998); [2]: Fitzpatrick et al. (2002); [3]: Ribas et al. (2002); [4]: Fitzpatrick et al. (2003).

were determined from medium-resolution spectra (R=15 500–23 000), obtained with Hubble Space Telescope (HST, 2.5 m) and Cerro Tololo Inter-american Observatory (CTIO, 4 m). Spectrophotometry was acquired with FOS and STIS instruments on board HST. The resulting distances have a scatter that is larger than their formal errors and seem to support the idea that the line-of-sight structure of the LMC is being detected and compromising its value as the first step of the extragalactic distance ladder.

1.3.3 Eclipsing binaries in M 31 and M 33

The first discoveries of M 31 EBs (~ 60 systems) came from photographic surveys in the 60's (Baade & Swope, 1965, and references therein). Due to selection effects, the observed binaries are among the brightest stars in the galaxy, being composed of luminous (and massive) O/B type stars. The low precision of the obtained light curves and the difficulty of obtaining radial velocities made that few attention was paid to these newly discovered EBs.

However, over the past two decades, the use of large format CCD detectors with high quantum efficiencies and low read-out noise has enabled the acquisition of precise (~ 0.01 mag) photometry for 19–20 mag stars with moderate size telescopes (2–3 meter). In addition, the development of improved reduction techniques (such as image subtraction, Alard & Lupton, 1998) has allowed the clear identification of EBs in galaxies well beyond the Local Group (e.g., Bonanos & Stanek, 2003). Together with the improvement on the quality of the light curves, large (8–10 m) telescopes have been built, enabling the acquisition of accurate radial velocities.

In this sense, the DIRECT group (see Macri, 2004, and references therein) started the identification of new EBs in M 31 (Fig. 1.5) and M 33, with 1.2–1.3

meter class telescopes, reporting almost 100 new EB systems in each galaxy. The resulting photometry has an error of $\sim$ 0.05 mag, which is just on the limit to disentangle the correlations among the parameters governing the light curve modeling. Even though, one of the detected EBs in M 33 was used to derive the first direct distance determination to M 33 (Bonanos et al., 2006).

1.4 Goals

Following the same principles already used for the LMC, **the fundamental goal of the present project is to carry out a one-step, accurate distance determination to M 31 using double-line EB systems** (Ribas & Jordi, 2003; Ribas et al., 2004). As previously mentioned (Sect. 1.3), the methodology involves, at least, two types of observations: photometry to obtain the light curves and spectroscopy to obtain the radial velocity curves.

Therefore, a large observational campaign was undertaken with the Isaac Newton Telescope (from 1999 to 2003) to find the most suitable EBs for distance determination to M 31. Following the DIRECT project, a field overlapping their observed fields (Fig. 1.5) was selected to obtain better quality light curves of their reported EBs. Observations were analyzed to discover eclipsing binaries and Cepheids suitable for distance determination (see Chap. 2).

Given the faintness of the targets, large telescopes (8–10 m) are needed to obtain the required radial velocities. The optimum targets for distance determination were selected to be observed with Gemini-North telescope (see Chap. 3). The resulting spectra were used to determine the fundamental properties for four of the selected EBs (Sect. 4).

The remaining needed parameters for distance determination (surface fluxes and line-of-sight extinction) can be obtained from several methods, either from modeling the spectral energy distribution or by new procedures (e.g., Sect 4.1.1.3). The combination of the results yields an accurate determination of the distance to the EB systems and, hence, to M 31 (Sect. 4.2).

In addition to providing accurate distances, the resulting fundamental stellar properties, such as masses and radii, can be used as powerful diagnostics for **studying the structure and evolution of stars that were born in a different chemical environment from that in the Milky Way** (Sect 4.1).

The large data volume treated also provides valuable information for the study of other stellar populations. As seen in previous sections, Cepheids are important standard candles. The photometric catalog resulting from the EB search yielded large numbers of Cepheids. Therefore, **the analysis of the Cepheid population was used to further constrain the distance to M 31** and enable the better calibration of the standard candles commonly used for distance determination (Chap. 5).

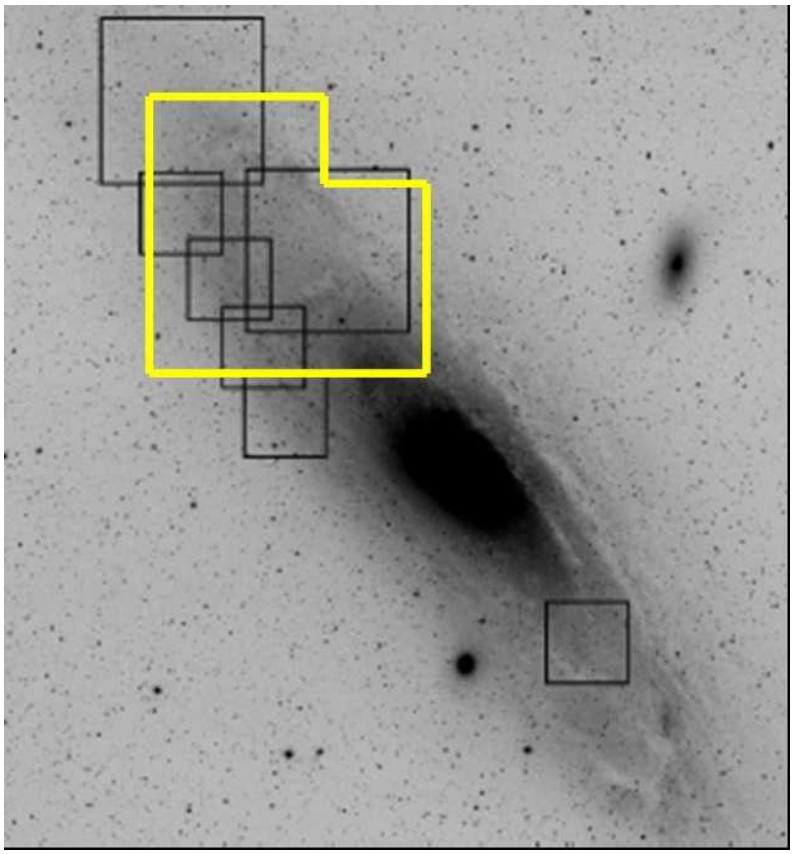

Figure 1.5. Image of M 31 as reported in Macri (2004) with the corresponding DIRECT fields (black boxes). The field studied in the present work has also been over-plotted (white box).

Finally, as a proof of the potential of the obtained photometric catalog and as a by-product of the present work, **the analysis of a flaring M star in the Milky Way**, revealed one of the most intense optical flares ever reported (Appendix A).

2 Time series photometry⋆

The main goal of this project (Sect. 1.4) requires high-quality light curves to obtain precise fundamental properties. By the time this project started, the highest-quality EB light curves were those obtained by the DIRECT group (Kaluzny et al., 1998; Stanek et al., 1998, 1999), but the scatter was too large to determine the physical elements reliably (see Sect. 1.3.3). Therefore, we undertook a new photometric survey to obtain high-quality EB light curves (see Sect. 2.1). With the application of the difference image analysis algorithm in the data reduction process (see Sect. 2.2), precise photometry was obtained not only for the EBs in the field, but also for all the variable stars. Two photometric catalogs were compiled (see Sect. 2.3). The reference catalog contains the photometry in both *B* and *V* passbands of 236 238 stars. Among all the stars in the reference catalog, 3 964 were identified as variable and included in the variable star catalog. The variable star catalog contains 437 EBs and 416 Cepheids and represent the initial lists of variable stars used for distance determination to M 31.

2.1 Observations

The observations were conducted at the 2.5 m Isaac Newton Telescope (INT) in La Palma (Spain). Twenty-one nights in five observing seasons were granted between 1999 and 2003 (one season per year). The Wide Field Camera, with four thinned EEV 4128×2148 CCDs, was used as the detector. The field of view of the WFC at the INT is $33\farcm8 \times 33\farcm8$, with $0\farcs33$ pixel^{-1} angular scale. With this configuration, we found that an exposure time of 15 minutes provides the optimum S/N for stars of $V \sim 19$ mag and ensures that no significant luminosity variation occurs during the integration for EBs with a period longer than one day.

All observations were centered on the same field located in the north eastern part of M 31 ($\alpha = 00^{\rm h}44^{\rm m}46^{\rm s}$ $\delta = +41^\circ38'20''$). The field of study (Fig. 1.5) was

⋆The contents of this chapter were published in Vilardell et al. (2006).

Table 2.1. Number of images used in the data reduction process for each of the five observing campaigns.

Frame	1999	2000	2001	2002	2003	Total
Granted nights	3	4	4	5	5	21
Bias	5	21	10	46	24	106
Darks	0	0	0	6	0	6
B flat-fields	20	31	19	21	42	133
V flat-fields	23	17	14	27	25	106
B Landolt fields	12	0	8	0	0	20
V Landolt fields	16	0	11	0	0	27
B M 31 field	41	45	45	54	80	265
V M 31 field	40	45	43	49	82	259
Total	157	159	150	203	253	922

selected to overlap with the DIRECT fields A, B, and C, since the initial main objective of the project was to obtain high-quality photometry of already known EBs (see Sect. 1.4). To reduce blending problems in such a crowded field (see Fig. 2.1), all the images with PSF FWHM larger than 3″ were rejected. As a result, 265 and 259 frames, with median seeings of 1.″3 and 1.″2, were selected for further analysis in the *B* and *V* passbands, respectively. In addition, during two nights of the 1999 observing run and one night of the 2001 observing run, 15 Landolt (1992) standard stars were observed from three fields (PG0231+051, PG1633+099, and MARK A). In Table 2.1, a complete list of all the images used in the data reduction process for the five observing seasons is presented.

2.2 Data reduction

The treatment of the obtained images follows five major steps: (1) raw data calibration to correct the images, (2) difference image analysis to obtain differential photometry for the variable stars, (3) standard photometry transformation, (4) astrometry to obtain the star positions and (5) periodicity search to compute the periodicity for the variable stars.

2.2.1 Data calibration

The science images for each of the five observing seasons were reduced using the IRAF[1] package. Only bias, dark, and flat-field frames corresponding to the same

[1]IRAF is distributed by the National Optical Astronomy Observatories, which are operated by the Association of Universities for Research in Astronomy, Inc., under cooperative agreement with the NSF.

observing season were used to reduce a given science image.

Each WFC image was separated into four overscan-subtracted images, one per CCD frame. After this step, each CCD frame was treated separately during the reduction process. Bad pixels[2] were also corrected for all images through linear interpolation from the adjacent pixels. Although this method is not optimal for reducing photometric data (since the flux of stars on bad columns is not conserved), it yields the best results for cleaning the calibration images (bias and flat-field images).

A master bias was built for each observing season and CCD frame. Each pixel of the master bias is the median value of the same pixel in all the bias frames. The resulting bias frames were subtracted from each flat-field frame. The bias-subtracted flat-field frames were corrected for non-linearity effects[3] and averaged to produce a master flat-field image for each observing season, CCD frame, and filter.

The science images were processed by subtracting the bias frame and corrected for non-linearity and flat fielding. The resulting images are free of most of the instrumental effects, except for a small area close to the north eastern corner of the field that is associated with field vignetting (see Fig. 2.1).

2.2.2 Difference image analysis

Given that the field under study is highly crowded, a package based on the image subtraction algorithm (Alard & Lupton, 1998) was used to obtain the best possible photometric precision. This technique has the advantage that variable stars are automatically detected and that precise photometry can be obtained even in highly crowded fields. We used our own implementation of the difference image analysis package (DIA) developed by Wozniak (2000). The image subtraction algorithm requires a high-quality reference image. This image was created during the first step of the process by the DIA for each CCD and filter. The combination of the 15 best seeing images produced two reference images, one with $0\farcs9$ FWHM for *V* (see Fig. 2.1) and one with $1\farcs0$ FWHM for *B*.

The main part of the process is the determination of the convolution kernels. The kernels are constructed to match the reference image with each one of the remaining frames under study (supposedly with different seeing values). The DIA kernels are composed of Gaussian functions with constant widths and modified by polynomials. In our case, the kernels consist of three Gaussians with polynomials of orders 4, 3, and 2. A space-varying polynomial of order 4 was also used to

[2]The pixel positions were obtained from the webpage:
`http://www.ast.cam.ac.uk/~wfcsur/technical/pipeline/`

[3]Coefficients were obtained from the webpage:
`http://www.ast.cam.ac.uk/~wfcsur/technical/foibles/`

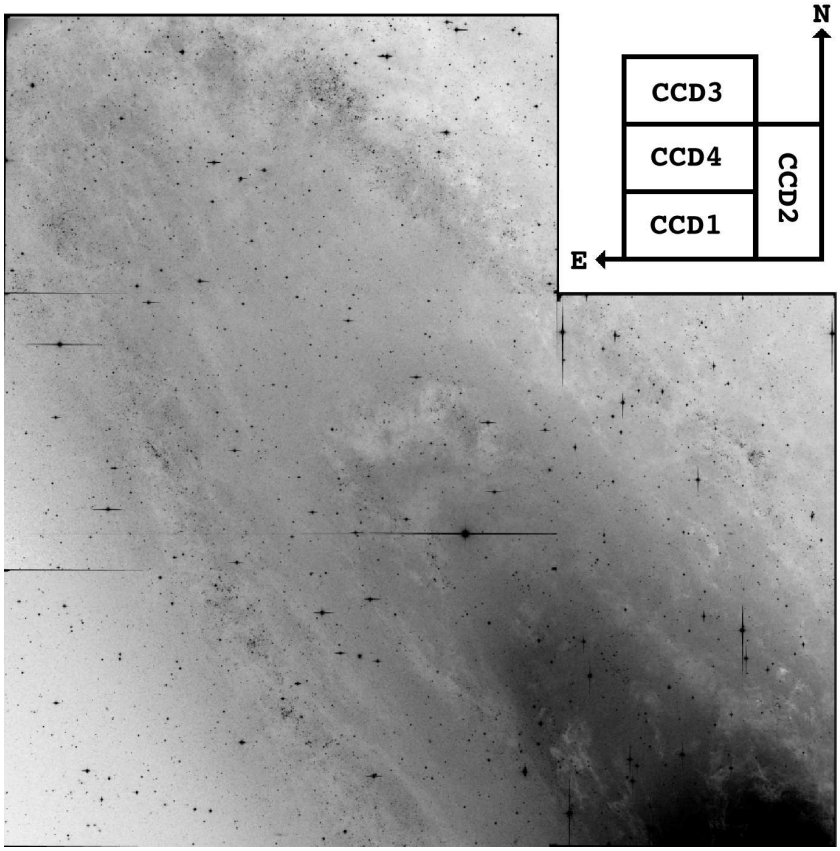

Figure 2.1. Reference image of the selected field of view in V filter. The center of the field is at $\alpha = 00^{\mathrm{h}}44^{\mathrm{m}}46^{\mathrm{s}}$ and $\delta = +41^{\circ}38'20''$

account for the spatial variation across the image. The resulting kernels were convolved with the reference image and subtracted from the original frames to obtain images containing only objects with brightness variations (plus noise).

The variability image is constructed from the differentiated images. This variability image contains all pixels considered to have light-level variations. A pixel is considered to vary if it satisfies at least one of the following two conditions:

- There are more than 4 consecutive observations deviating more than 3σ (where σ is the standard deviation) from the base-line flux in the same direction (brighter or fainter).
- There are more than 10 overall observations deviating more than 4σ from the base-line flux in the same direction.

The variability image is used to identify the variable stars. The reference image PSF is correlated with the variability image and all local maxima with correlation coefficients in excess of 0.7 are considered to be variable stars. Once the

variable stars are located, PSF photometry is performed on all the differentiated images to obtain the differential fluxes. The differential fluxes can be transformed to the usual instrumental magnitudes through the following expression:

$$m_i = C - 2.5 \log(f_0 + a\Delta f_i) \tag{2.1}$$

where Δf_i is the differential flux of a star in the ith observation, f_0 is the base line flux on the reference image, C is a zero-point constant, m_i is the instrumental magnitude of a star in the ith observation, and a is a scaling factor (see below).

The photometric package of DIA does not properly account for contamination from nearby stars in crowded fields (such as in our case). Therefore, the f_0 values obtained with the DIA can potentially be severely overestimated. To obtain precise values for f_0, DAOPHOT PSF photometry (Stetson, 1987) was applied to the reference image. Given that DIA and DAOPHOT photometry use different PSF definitions and functional forms, a scaling factor (a) is needed to transform the DIA fluxes into the DAOPHOT flux units (see Zebrun et al., 2001, for an extensive discussion). A synthetic image was created to compute the scaling factors. The synthetic image contains the representation of the DAOPHOT PSFs at the position of each variable star. The scaling factor at the position of each variable star was obtained from the comparison with the DIA photometry of each PSF. For similar PSFs, the scaling factor can be obtained with an error of 0.3% or less.

This process provided instrumental magnitudes for all the variable stars, as well as all the stars in the reference image. Two main sources of potential systematic errors exist with this procedure, f_0 and a. Both sources affect the amplitudes of the light curves without introducing any additional scatter. Therefore, the only way to study the presence of possible systematics is by comparing the derived light curves with other results given in the literature. As shown in Sect. 2.4.1, the amplitudes of the fitted EBs are perfectly compatible with DIRECT light curves. In addition, the reference fluxes (f_0) result in standard magnitudes that are fully compatible with LGGS and DIRECT standard magnitudes (Sect. 2.3.1). Therefore, the existence of any additional photometric errors resulting from systematics in the derived parameters (f_0 and a) can be excluded.

2.2.3 Standard photometry

To transform instrumental to standard magnitudes, the observed Landolt (1992) standard stars were used. Although the standard stars were observed at different times during the night, the number of collected frames is not enough to accurately determine the atmospheric extinction. Therefore, as a first step, the M 31 images obtained during the same night as the standard stars (30 images in total) were used to compute the coefficients needed to account for the atmospheric extinction. Aperture photometry on 20 bright, but not saturated, and isolated stars on the

M 31 frames was performed. For each night and filter, a linear fit was obtained with dispersions ranging from 0.008 mag to 0.03 mag.

As a second step, aperture photometry was performed on the standard stars. The instrumental magnitudes obtained were corrected with the atmospheric extinction coefficients. The resulting values were used to find the transformation coefficients between the instrumental magnitudes and the standard magnitudes. For each night and CCD, the following relationship was determined:

$$v - V = A_1 + A_2(B - V) \tag{2.2}$$

$$b - v = A_3 + A_4(B - V) \tag{2.3}$$

where b and v are the instrumental magnitudes, B and V the standard magnitudes, and A_i are the transformation coefficients. The resulting mean standard deviation of the fits is 0.02 mag.

The transformation coefficients cannot be directly applied to the M 31 instrumental magnitudes because the latter are based on the reference image, which is a combination of different images. In addition, the transformation coefficients are determined from aperture photometry, while the M 31 instrumental magnitudes have been determined from PSF photometry. For this reason, the only way to obtain standard magnitudes for the M 31 stars is to apply the transformation coefficients to the frames obtained during the same nights as the standard stars.

PSF photometry is needed to find precise standard magnitudes of a reasonable number of objects in the M 31 field, since aperture photometry can only be applied to isolated stars. A sample of bright and isolated stars was used to determine a scaling value to transform the PSF magnitudes into aperture photometry values for each one of the 30 M 31 frames. The scaling values and the transformation coefficients were then used to obtain standard magnitudes for 18 426 objects in the field. A systematic difference was observed for the standard magnitudes obtained from the 2001 frames (probably the night was not photometric), so these values were rejected. The standard magnitudes of every star in all the remaining frames (22 in total) were averaged, and the standard deviation was considered a good estimation of its uncertainty.

The standard magnitudes resulting from this process were used to determine new transformation coefficients (A_i) for the reference images. Only 534 non-variable and non-saturated objects detected in all the frames and with an error below 0.04 mag were used for this purpose. This sample has good standard color and magnitude coverage, with $-0.3 < B-V < 1.7$ mag and $17.5 < V < 21.0$ mag, providing fits with dispersions ranging from 0.013 mag to 0.019 mag, depending on the CCD.

The resulting coefficients were applied to the reference images. The objects detected in the V frame were cross-matched with the objects detected in the B frame. Only the objects identified within $0\farcs33$ (one pixel) in *both passbands* have

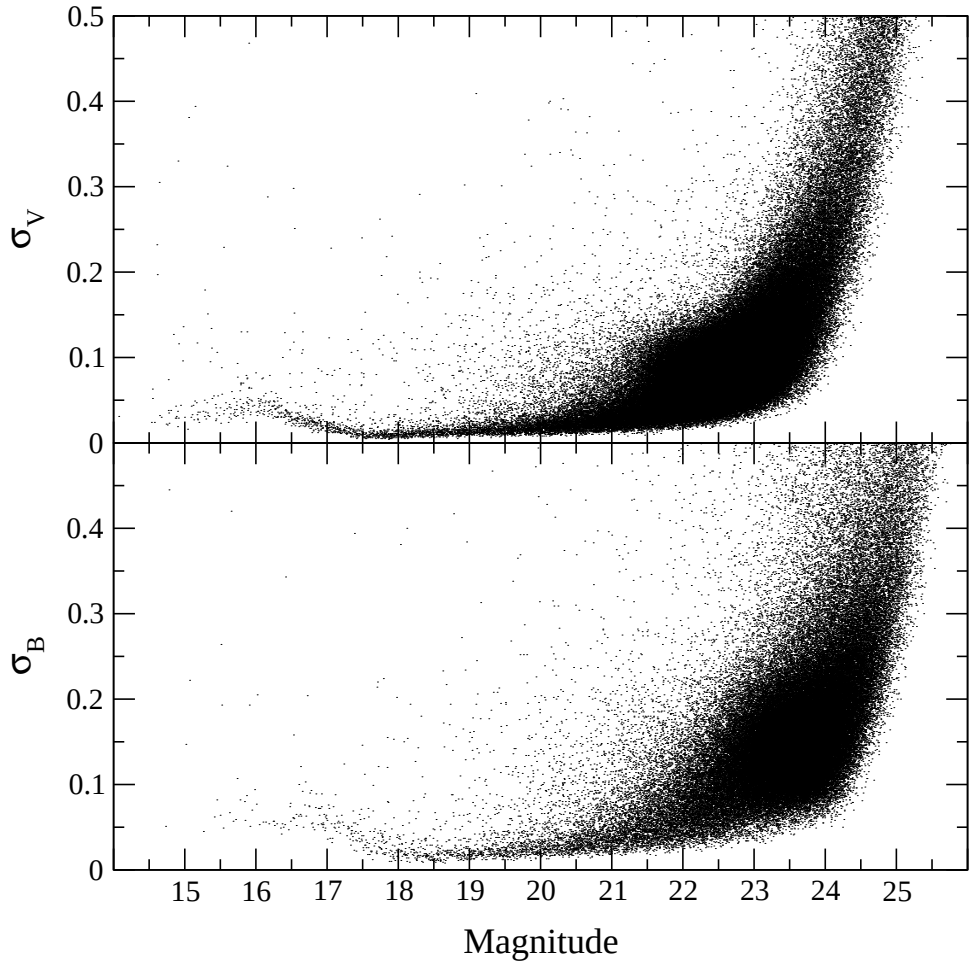

Figure 2.2. Standard errors as a function of magnitude for the entire photometric catalog containing 236 238 objects with photometry in both *V* and *B* passbands.

been included in the reference catalog, providing standard photometry for 236 238 objects. Of these, 37 241 objects have errors below 0.1 mag in both passbands (Fig. 2.2). The limiting magnitudes of the photometric catalog are around $V \simeq 25.5$ mag and $B \simeq 26.0$ mag, and it is estimated to be complete up to $V \simeq 22.3$ mag and $B \simeq 23.5$ mag (see Fig. 2.3). Including only the objects with photometry in both passbands introduces a bias in the *V* band completeness because stars usually have positive $B - V$ values. Therefore, some faint stars in *V* were not included in the catalog because their *B* magnitudes were beyond the detection limit. Since the standard color is needed to obtain the *V* standard magnitude, this procedure ensures that all the photometry in the reference catalog uses the same transformation coefficients.

Finally, the same coefficients used in the reference images were applied to transform the m_i values in Eq. 2.1 to standard photometry in both *B* and *V* passbands for a total of 3 964 variable stars.

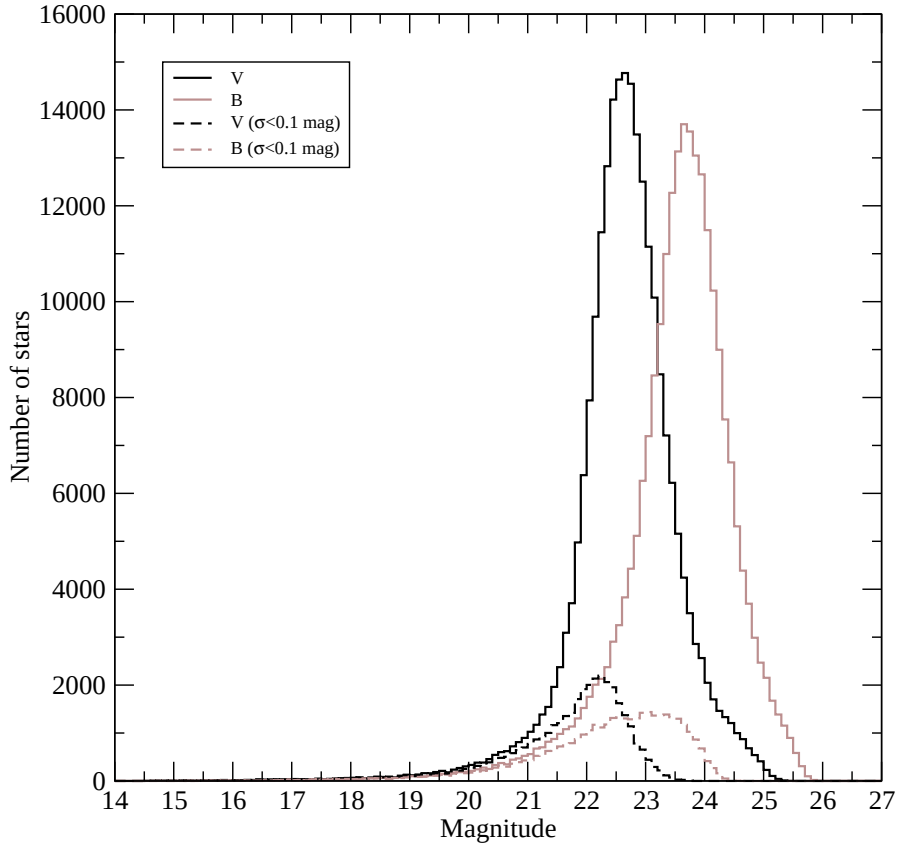

Figure 2.3. Number of stars as a function of the standard magnitudes for the two passbands (*B* and *V*). Number of stars with errors below 0.1 mag are also shown.

2.2.4 Astrometry

Standard coordinates for all detected objects were computed from several reference stars in the GSC 2.2.1[4]. To ensure that the reference stars are uniformly distributed, each CCD was divided into 3×6 sectors. Three reference stars (with $V \simeq 18$) were identified manually in each sector, yielding an initial list of 54 reference stars per CCD. Fits using third-order linear equations with 2σ scatter clipping were applied to determine the transformation of coordinates. After the iterative process, at least two reference stars had to remain in each sector. Otherwise, an additional reference star was selected in the corresponding sector and the entire process was repeated.

The resulting coordinates were compared with those in the GSC 2.2.1 catalog. A total of 724 objects with a position difference of less than 3″ in the two catalogs were identified. As can be seen in Fig. 2.4, no systematic trends appear in the comparisons, which have dispersions of $\sigma_\alpha = 0\farcs16$ and $\sigma_\delta = 0\farcs12$.

[4]Data obtained from: `http://cdsweb.u-strasbg.fr/viz-bin/Vizier`

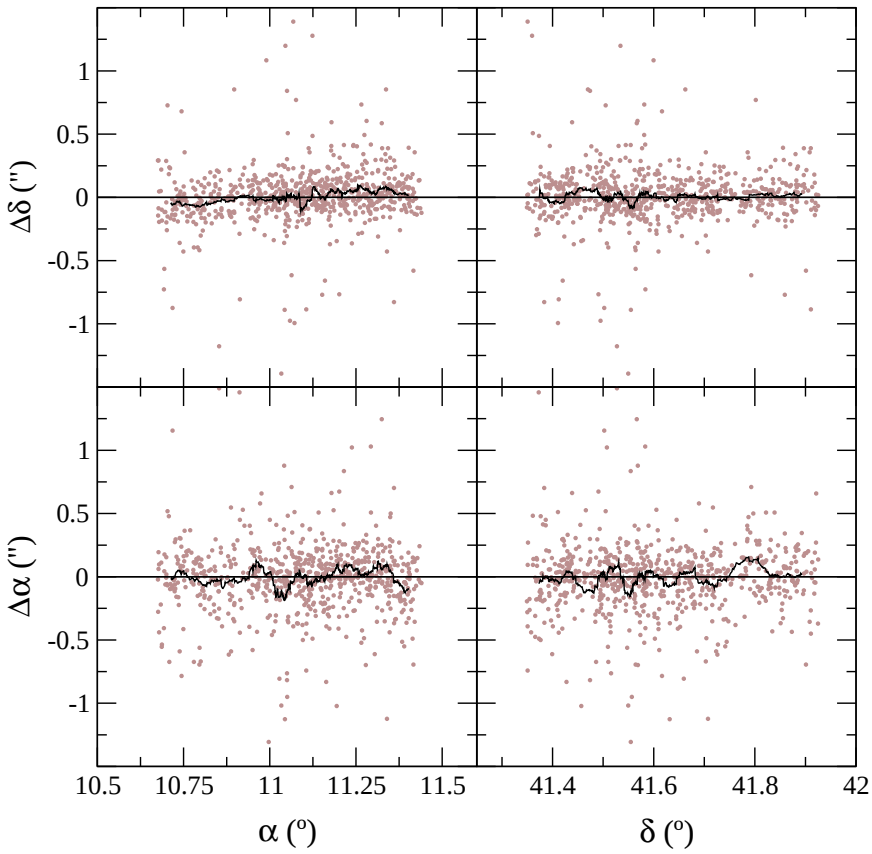

Figure 2.4. Differences between the coordinates obtained from our procedure and the coordinates from the GSC 2.2.1 catalog for 724 identified stars (circles). The line represents a running average.

2.2.5 Periodicity search

Since the observations were performed in five annual observing seasons, the data are very unevenly sampled. To overcome this major drawback in determining periodicities, a program based on the analysis of variance (Schwarzenberg-Czerny, 1996) was used to compute the periodograms for each variable star and filter (*B* and *V*). The periodograms were computed with 7 harmonics, because this setup was found to provide optimal results for the detection of EB systems, which constitute the main objective of the present survey. The lower limit in the period search was set to one day from the consideration that EBs with periods below one day are likely to be foreground contact systems and therefore not of interest for this survey. In addition, given the relatively long exposure time for each observation in the present survey (15 minutes), important brightness variations during the integration time could occur for the short-period variables. These factors make the computational effort of extending the period search below 1 day not worthwhile. On the opposite end, an upper limit of 100 days was selected to detect as many

long-period Cepheids as possible.

For each variable star, two periodograms (one in B and one in V) were used to obtain a consistent period determination. The resulting light curves were visually inspected to locate well-defined variability patterns, thus leading to the identification of a total of 437 EBs and 416 Cepheids. For several EBs and Cepheids, the period determination was a multiple of the true period and, therefore, it was recomputed. Finally, the times of minimum of both light curves (B and V), which were computed from Fourier series ($F^{(7)}(t)$ in Schwarzenberg-Czerny, 1996), were used to compute a reference time for all the light curves.

2.3 The catalogs

As a result of the data reduction process, two catalogs were obtained. The first one includes all the detected objects in the field. The second one contains the data for all the variable stars.

2.3.1 Reference catalog

The photometry of the 236 238 objects detected in the reference images was grouped into the reference catalog (Table 3)[5], which contains the object identifier, the right ascension, the declination, the V standard magnitude in the reference image, the V standard error, the B standard magnitude in the reference image, the B standard error, and, in case there is a previous identification, the corresponding identifier. The catalogs cross-matched with our reference catalog are GSC 2.2.1, DIRECT, LGGS (Massey et al., 2006), and Todd et al. (2005, hereafter T05). Photographic catalogs are identified in the previous works, specially in LGGS, and they are not cross-identified here.

According to the IAU recommendations, the identifier was built from the object position and considering the observational angular resolution. The resulting format is M31 JHHMMSSss+DDMMSSs. For the variable stars, the acronym was changed from M31 to M31V to indicate that they can be found (with the same identifier) in the variable star catalog (see Sect. 2.3.2).

To show the general photometric properties of the obtained catalog, the color-magnitude diagram for the 37 241 objects with a photometric error below 0.1 mag in both B and V is shown in Fig. 2.5. It can be seen from this diagram that most of the stars in this catalog are stars at the top end of the main sequence, with some foreground giants and stars at the tip of the red giant branch.

[5]Table 3 is available in electronic form at the CDS via anonymous ftp to
`cdsarc.u-strasbg.fr (130.79.128.5)` or via
`http://cdsweb.u-strasbg.fr/cgi-bin/qcat?J/A+A/459/321`

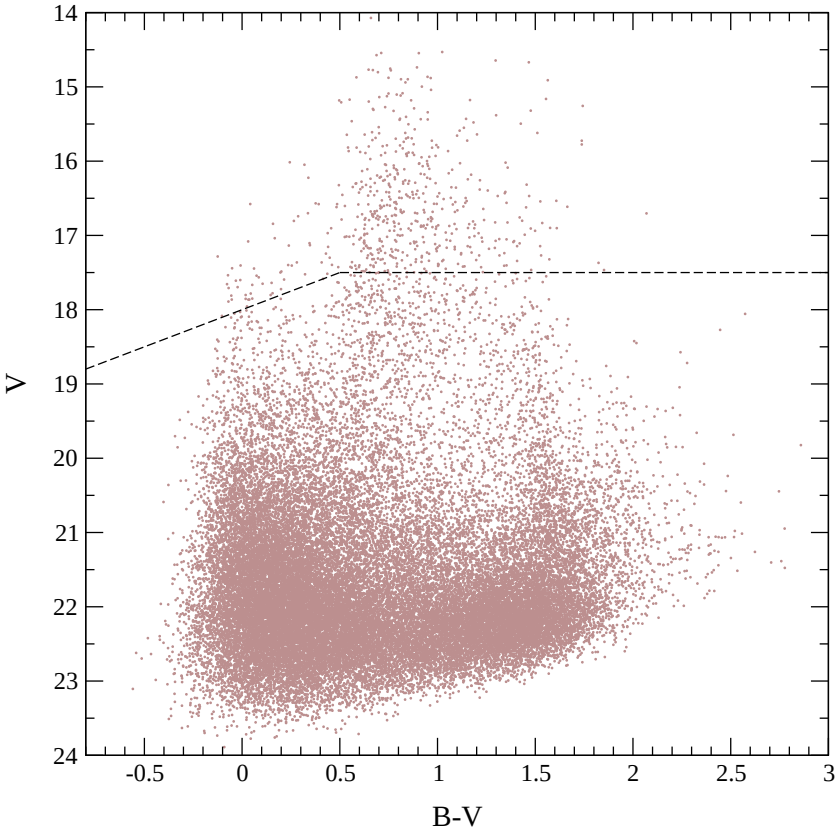

Figure 2.5. Color–magnitude diagram for 37 241 objects with photometric errors lower than 0.1 mag in both *B* and *V* in the reference catalog. Stars above the dashed lines are saturated.

The standard photometry depends on a certain number of zero-point calibrations (Sect. 2.2.2 and Sect. 2.2.3). Considering that an error in the standard magnitudes has a direct impact on the distance determination, it is extremely important to ensure that no systematic errors affect the photometry. For this reason, it is worthwhile checking the consistency of the standard magnitudes given here. Fortunately, there are two CCD surveys with *B* and *V* photometry of a large number of stars that overlap with the field under study: DIRECT (Macri, 2004) and LGGS (Massey et al., 2006). The non-saturated objects of our survey ($V > 17.5$ and $B > 18.0$) were cross-identified with the magnitudes reported by the DIRECT group[6] and by the LGGS group[7]. For the DIRECT survey, a total of 14 717 and 7 499 objects were identified in *V* and *B* passbands, respectively (see Fig 2.6). The comparison with the LGGS survey provided 36 353 common objects (see Fig. 2.7).

Although some trend is observed for the DIRECT *B* magnitudes, the LGGS *B*

[6]Data source: `ftp://cfa-ftp.harvard.edu/pub/kstanek/DIRECT/`
[7]Data source: `http://www.lowell.edu/users/massey/lgsurvey/`

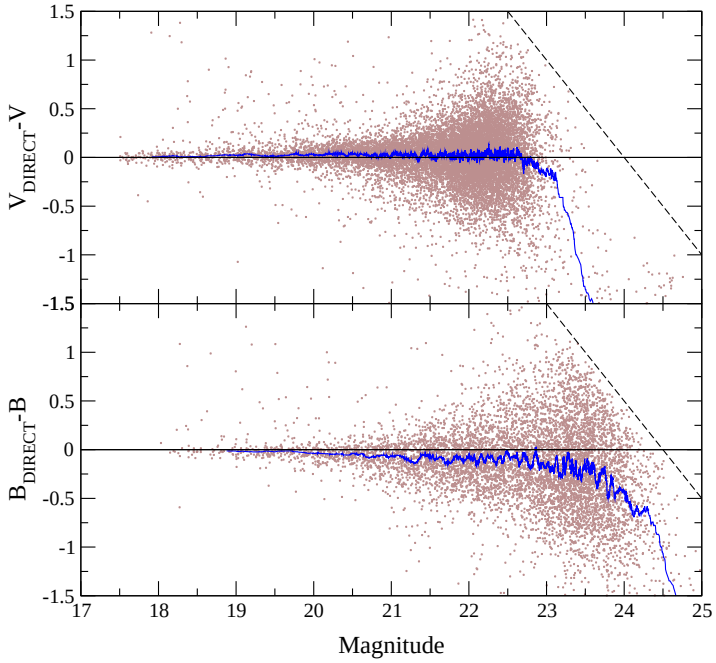

Figure 2.6. Differences with DIRECT standard magnitudes versus the magnitudes in the reference catalog. The comparison has 14 717 stars in *V* and 7 499 in *B*. The dashed lines show the limiting magnitudes. The solid line is a running average.

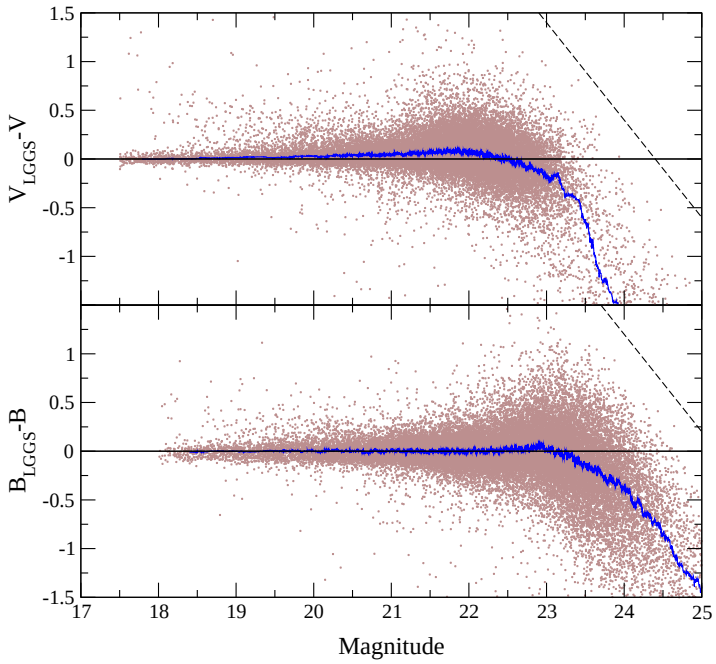

Figure 2.7. Differences with LGGS standard magnitudes versus the magnitudes in the reference catalog for a total amount of 36 353 stars in each passband. The dashed lines show the limiting magnitudes. The solid line is a running average.

magnitudes are completely consistent with the magnitudes in our survey. Therefore, the *B* standard magnitudes in the present catalog are expected to have no systematic error. Regarding the *V* magnitudes, some low-level systematics have been observed with the two catalogs. The DIRECT *V* magnitudes are larger by about 0.02 mag than the values in the reference catalog, and the LGGS comparison shows an increasing trend towards larger magnitudes. The 5 768 objects with *V* magnitudes in the three catalogs were used to study the observed systematics. The comparisons between the three catalogs always reveal some kind of trend and, so it was impossible to conclude whether there are any (low-level) systematics affecting the *V* standard magnitudes. In any case, the differences for the brightest stars ($V < 20.5$ mag) are well below 0.03 mag. Taking into account that all the EBs that can be used for distance determination have $V < 20.5$ (Sect. 2.4.1), this is the maximum systematic error that can exist in their *V* standard magnitudes.

2.3.2 Variable star catalog

The 3 964 variable stars identified in the reduction process were included in the variable star catalog (Table 4)[8]. For each variable star, we provide the corresponding identifier (see Sect. 2.3.1), the right ascension, the declination, the intensity-averaged *V* magnitude (Eq. (9) in Saha & Hoessel, 1990), the mean *V* error, the intensity-averaged *B* magnitude, the mean *B* error, the number of observations in *V*, the number of observations in *B*, the reference time computed in Sect. 2.2.5 (in HJD), the period (in days) and a label, indicating whether the variable star was identified as an EB or a Cepheid.

Although a period estimate is given for each variable star, obviously not all the variable stars are periodic. When comparing the window function with the period distribution for all variable stars (see Fig. 2.8), it is clear that many of the period determinations are just an alias introduced by the window function, especially for those over five days (frequency below 0.2 days^{-1}). Therefore, a significant number of the variable stars are, in fact, non-periodic variables or variables with a period out of the studied range (1–100 days). All light curves (time series photometry) are also provided (Table 5)[9], together with the variable star catalog. For each variable star and observation, the time of observation (in JD), the standard magnitude (*V* or *B*) and the standard error are given.

Part of the images in the present survey were also reduced by T05 who reported 127 EB systems. Therefore, the photometry on the variable star catalog

[8]Table 4 is available in electronic form at the CDS via anonymous ftp to
`cdsarc.u-strasbg.fr (130.79.128.5)` or via
`http://cdsweb.u-strasbg.fr/cgi-bin/qcat?J/A+A/459/321`

[9]Table 5 is available in electronic form at the CDS via anonymous ftp to
`cdsarc.u-strasbg.fr (130.79.128.5)` or via
`http://cdsweb.u-strasbg.fr/cgi-bin/qcat?J/A+A/459/321`

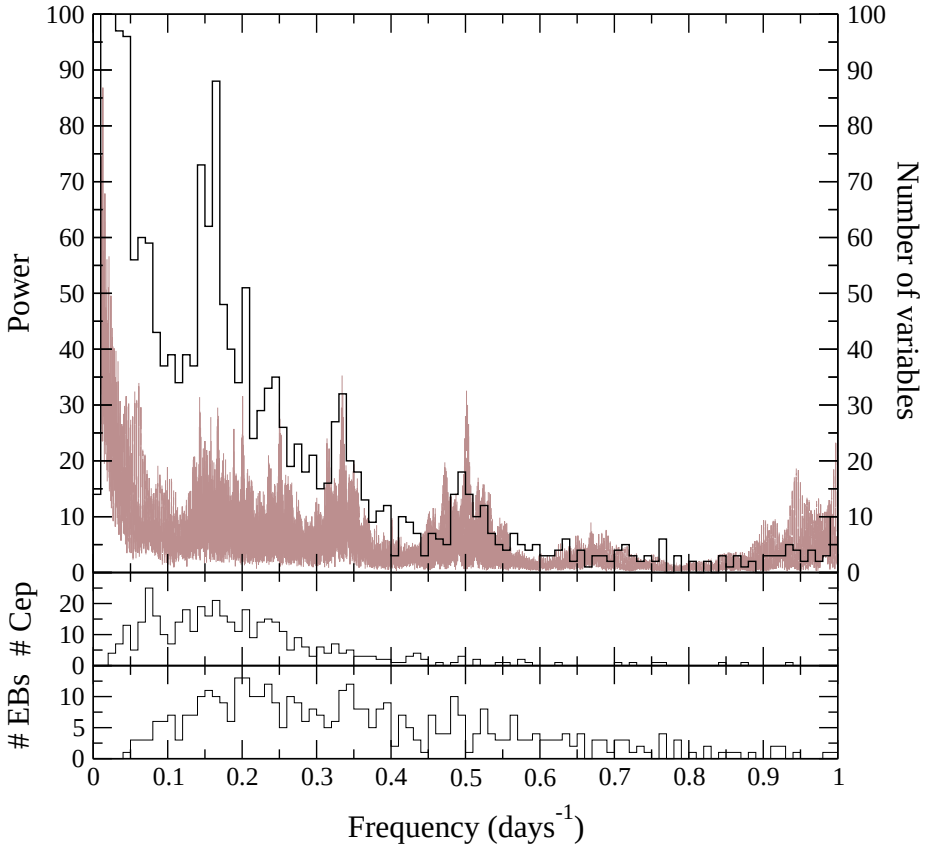

Figure 2.8. Top: Window function for the studied period range (lines) and frequency distribution for all the stars in the variable star catalog (histogram). **Middle:** Frequency distribution for the Cepheids in the variable star catalog. **Bottom:** Frequency distribution for the eclipsing binaries in the variable star catalog.

can be directly compared. Of the reported sample of 127 EBs, 123 stars have been detected in our reference catalog, 92 are in the variable star catalog and 90 have also been classified as EBs. The maximum $V^{\max}$ and $B^{\max}$ values for the 90 systems identified were matched with the magnitudes presented in T05 (see Fig. 2.9). A systematic trend can be observed in the V filter. In addition, Fig. 2.9 also reveals that the $B^{\max}_{\rm T05}$ magnitudes are lower than our $B^{\max}$ values.

When inspecting the origin of such a discrepancy, we observed that *all* the EBs labeled f2BEB and f3BEB in T05 had lower magnitude values than the EBs in our variable star catalog. Since 14 of these EBs also have DIRECT $V^{\max}$ magnitudes and 5 of them have DIRECT $B^{\max}$ values (Kaluzny et al., 1998; Stanek et al., 1998, 1999; Bonanos et al., 2003), we computed the mean differences (Table 2.2). Although the number of cross-matched EBs is small, their mean differences seem to indicate that the magnitudes reported in T05 for the f2BEB and f3BEB EBs suffer from a systematic offset. On the other hand, the magnitude values for the remaining EBs (f1BEB and f4BEB) are compatible in the three catalogs.

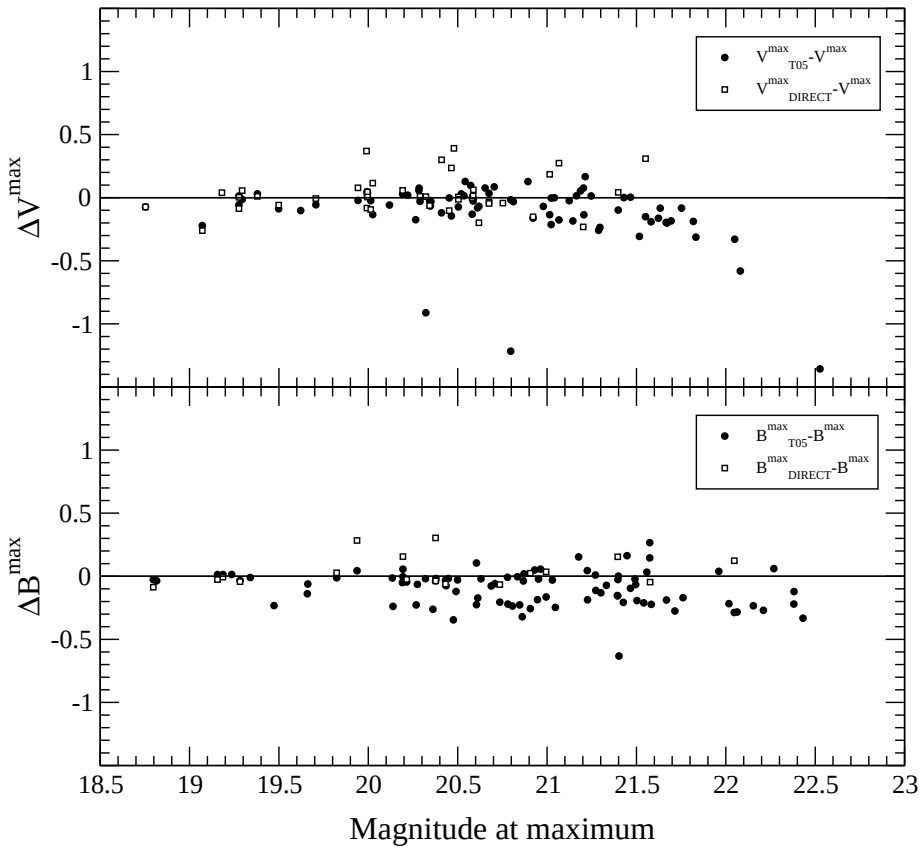

Figure 2.9. Differences between the DIRECT maximum magnitudes (open squares), the T05 maximum magnitudes (filled circles) and the maximum magnitudes for all the crossed EBs of the variable star catalog.

2.4 Selection of variable stars suitable for distance determination

Following the main goal of the present work, the variable star catalog was inspected to identify variable stars suitable for distance determination. Two populations were clearly identified: EBs and Cepheids.

2.4.1 Eclipsing binaries

In order to further characterize the EB sample in the variable star catalog, a neural network algorithm was used (Sarro et al., 2006). After some attempts, it was observed that the neural network still needed some further training to properly classify our EB sample in M 31. Since the training is an arduous effort that demands a large number of well known templates, the classification with neural

Table 2.2. Mean differences for the magnitudes at maximum of the EBs labeled f2BEB and f3BEB in T05.

Comparison	Differences
$V^{\max}_{\rm DIRECT} - V^{\max}$	0.062±0.047
$V^{\max}_{\rm T05} - V^{\max}$	-0.104±0.015
$V^{\max}_{\rm T05} - V^{\max}_{\rm DIRECT}$	-0.166±0.057
$B^{\max}_{\rm DIRECT} - B^{\max}$	0.054±0.039
$B^{\max}_{\rm T05} - B^{\max}$	-0.214±0.026
$B^{\max}_{\rm T05} - B^{\max}_{\rm DIRECT}$	-0.268±0.046

networks was withdrawn. Therefore, all the efforts were centered in identifying EBs suitable for distance determination.

Only those systems with a precise determination of their fundamental properties can be used as distance determination targets. In particular, radii with an error of around 4% result in distances with an error larger than 8%, since the absolute magnitude of a star and, hence, the distance, scales as $M_{\rm bol} \propto R^2$. The absolute radius of a star is obtained from the product of the semi-major axis ($a \sin i$, obtained from radial velocity curves) and the relative radius ($r = R/a$, directly determined from the light curves, Table 1.2). Therefore, an error around 2% is required for each quantity ($\sin i \sim 1$ for EBs). The desired precision in the relative radius can be achieved with photometry on the order of 0.01 mag and the precision in the semi-major axis can be achieved with errors in the semi-amplitudes on the order of 2%. The color–magnitude diagram (see Fig. 2.10) reveals that most of the detected EB systems contain high-mass components on the top of the main sequence. In addition, most of the systems have periods shorter than 10 days (and all of them have periods shorter than 30 days). The expected semi-amplitudes for massive stars with such short periods are on the order of a few hundred kilometers per second. In order to achieve 2% errors in these semi-amplitudes, radial velocities (RVs) with errors on the order of 10 km s^{-1}are required, implying spectral resolutions of R~3 000 at optical wavelengths. Therefore, considering that medium-resolution spectra are needed to obtain precise fundamental properties and that the largest currently available facilities are the 8–10 m class telescopes, only the brightest EB systems (with $V^{\rm mean} < 20.5$ mag) were selected for further study. In addition, the most precise fundamental properties (such as relative radii) can be achieved only for those systems with deep eclipses, so we further selected only those EBs with $\Delta B \geq 0.2$ mag and $\Delta V \geq 0.2$ mag.

The criteria listed above provided a list of 29 systems from the initial sample of 437 EBs. Of these, 5 systems were rejected because of the large scatter in their light curves (probably from the contamination of a brighter nearby star), leaving a total amount of 24 EBs selected for detailed further analysis.

The particular properties of each EB can have a strong influence on the pre-

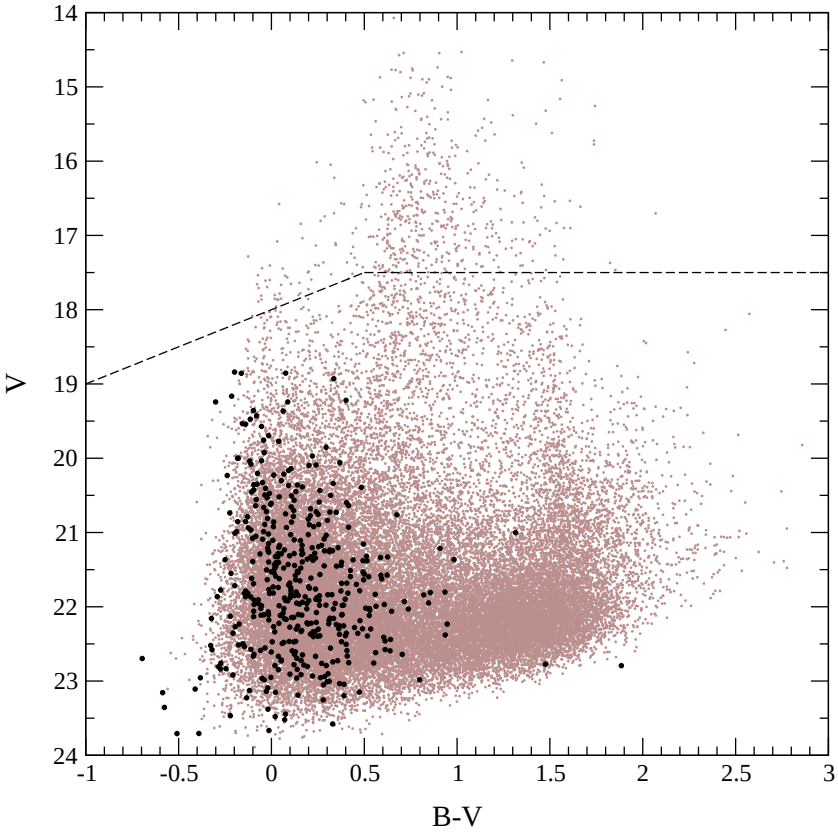

Figure 2.10. Color–magnitude diagram for 37 241 objects with photometric errors lower than 0.1 mag in both *B* and *V* in the reference catalog (gray dots) and 437 EBs (black circles). Stars above the dashed lines are saturated.

cise determination of its fundamental parameters. Therefore, to obtain the best distance determination targets, a preliminary fit was performed with the 2003 version of the Wilson & Devinney (1971) program (hereafter W&D) to the selected sample of 24 EBs. The fitting process was carried out in an iterative manner by considering both light curves (*B* and *V*) simultaneously. For those systems previously identified by the DIRECT group, their *V* light curve was also included in the fitting process. This provided an additional check on the consistency of the resulting photometry, because the DIRECT photometry was calculated from a PSF rather than using a DIA algorithm and, therefore, any possible systematics on the DIA photometry (Sect. 2.2.2) can be checked. Once a converging solution was achieved, a 4σ clipping was performed on all the light curves to eliminate (normally a few) outlier observations.

It is important to emphasize that, in the obtained light curves, the primary component has been defined to be the one eclipsed in the primary (deeper) eclipse. This convention has been maintained during the entire work.

In order to obtain more stable solutions, and to decrease the correlation among

the fitted parameters, the W&D assumes a certain configuration for each solution. The different configurations in W&D consider different scenarios where both, one or none of the eclipsing components fill the Roche lobe (the largest closed equipotential around a given star, so there is loss of matter to the companion if one star exceeds its lobe even slightly; Wilson & Wyithe, 2003). As previously mentioned, most of the observed systems seem to be composed by high mass components with relatively short periods. Therefore, a large fraction of the detected EBs are non-detached systems.

Two basic configurations were considered for each EB system: detached and semi-detached. Generally, the final fit in each one of the configurations provided some clues to the real configuration of the EB system. However, all systems showing non-zero eccentricity (secondary eclipse phase not exactly at 0.5) or unequal eclipse widths were considered to be detached EB systems. In some specific cases, a sinusoidal $O - C$ was observed when studying the fit residuals as a function of phase, with one quadrature brighter than the other. This is known as the O'Connell effect (O'Connell, 1951; Davidge & Milone, 1984). In the case of interacting high-mass systems, such effect can be explained by the presence of an equatorial hot spot on the surface of one of the components. This hot spot is supposed to be the consequence of impacting material arising from mass transfer between the components in a Roche-lobe filling configuration (semi-detached). The exact parameters of the spot cannot be obtained from the available data (strong degeneracies exist; Fitzpatrick et al., 2003) and, therefore, the spot parameters presented here are not necessarily physically valid but only capable of providing a good fit to the variations in the light curves.

Each EB needs to be treated as a particular case and careful selection of the adjustable parameters was performed individually. In general, the parameters fitted with W&D for our M 31 EBs are: the time of minimum ($t_{\rm min}$), the period (P), the inclination (i), the effective temperature of the secondary ($T_{{\rm eff},S}$), the normalized potential of primary (Ω_P), the normalized potential of secondary (Ω_S, for detached systems only), and the luminosity of the primary (L_P). For the eccentric systems, in addition, the eccentricity (e) and the argument of the periastron (ω) were also fitted. In some cases of semi-detached systems, the mass ratio (q) was treated as a free parameter. The limb-darkening coefficients (square-root law) were computed at each iteration from Kurucz ATLAS9 atmosphere models and the gravity brightening coefficients, as well as the bolometric albedos, were fixed to unity (assuming components with radiative envelopes). Finally, a third light (l_3) contribution was included for the final solutions of the EB systems. Since the field under study is extremely crowded, it is not surprising that some EBs may have a significant third light contribution (see Sect. 5.3.3 for a more extensive discussion on this topic). In addition, the obtained values of the third light contribution provide a first check on the realistic determination of the fundamental properties and give an indication of whether the scaling factor determinations (a in Eq. 2.1) are correct. Indeed, an error in the scaling factor has exactly the same effect as a third

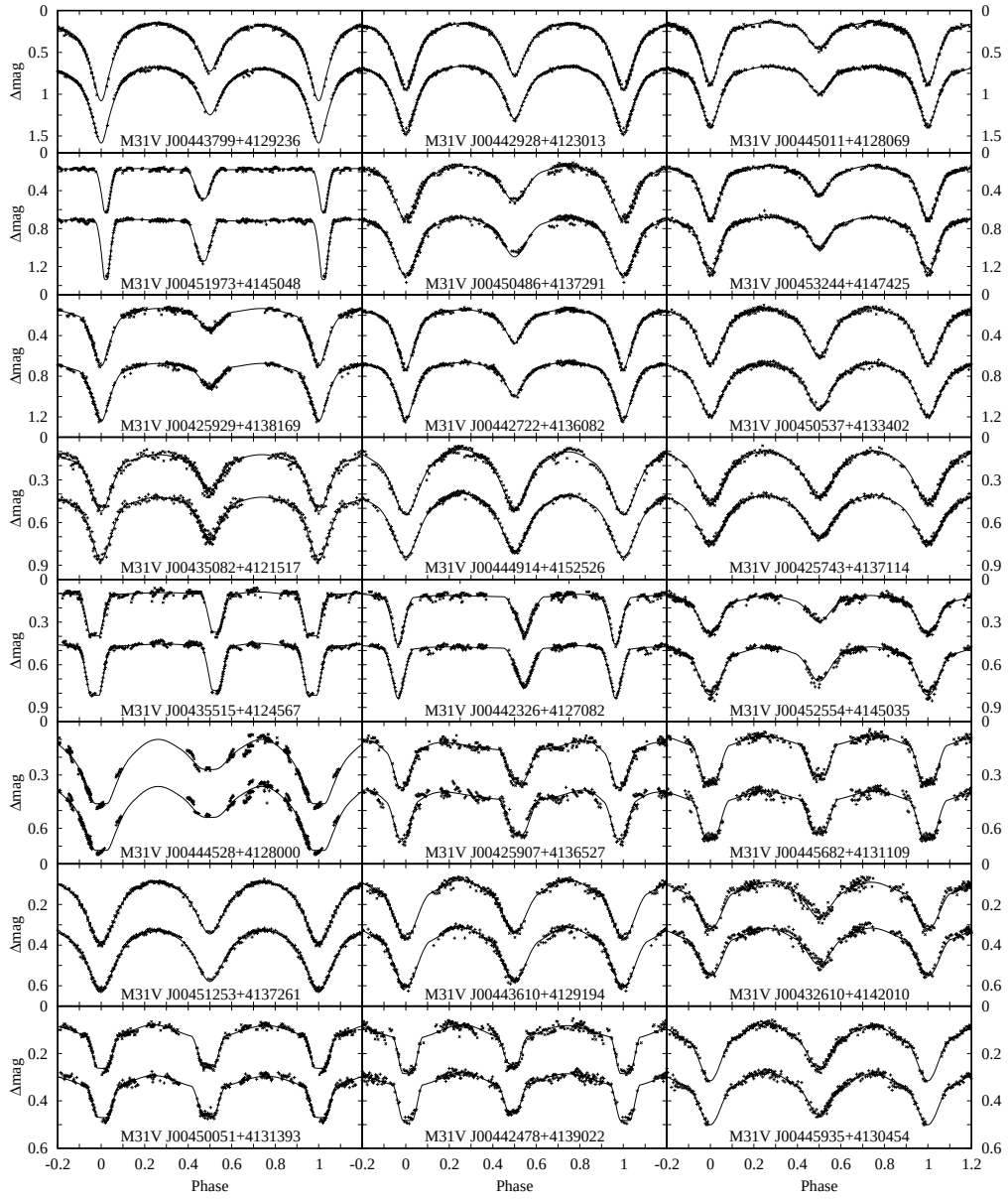

Figure 2.11. *B* (up) and *V* (down) light curves for the 24 fitted EBs. The corresponding W&D fits are also plotted (lines).

light contribution (either negative or positive).

Note that most of the solutions have a large number of free parameters. To some extent, the values presented here rely on the adoption of the mass ratio and, therefore, the fit results (in Table 2.3 and Fig. 2.11) should be regarded as preliminary until radial velocity curves are obtained. For some of the binaries, the values given in Table 2.3 need additional comments:

- M31V J00444528+4128000. This is the brightest EB system detected. A

converging fit could not be achieved because of variations in the light curve at the second quadrature. At this point, several possibilities could explain the observed variability, such as a varying hot spot, an accretion disk or the intrinsic variability of a supergiant component. This issue is further discussed in Sect. 4.1.3.

- M31V J00442326+4127082. The DIRECT light curve reveals a variation in the argument of periastron, thus indicating the presence of rapid apsidal motion ($\dot{\omega} = 1.9 \pm 0.6$ deg year^{-1}). Even taking the important third light contribution into account, the RV curves provide valuable information for studying the real nature of this detached, eccentric system (Sect. 4.1.4).

- M31V J00443799+4129236. From the fit residuals it became evident that the first quadrature is brighter than the other quadrature by about 0.025 mag in *B* and 0.020 mag in *V*. We modeled this effect in W&D by including a hot spot on the primary component. Assuming such a circular spot to be 40% hotter than the photosphere, its predicted radius is 16 ± 1 deg, and it is located at a longitude of 277 ± 6 deg (measured counterclockwise from the line of star centers). This system is further analyzed in Sect. 4.1.1.

- M31V J00451973+4145048. A largely negative *V* third light contribution is observed. However, the resulting error is also very large due to the lack of observations at the bottom of the primary eclipse. Considering that the *V* light curve is the only data set having no observations at the bottom of the primary eclipse and that positive third light contributions are observed for the other light curves, the derived fundamental parameters are expected to be accurate.

- M31V J00444914+4152526. An equatorial hot spot was assumed for this EB system. The best fit yields a spot with a temperature ratio of 1.2, at a longitude of 246 ± 14 deg and a size of 17 ± 3 deg.

- M31V J00442478+4139022. The large scatter of the DIRECT *V* light curve prevented a reliable fit from being achieved. Consequently, the DIRECT light curve was not used.

- M31V J00445935+4130454. A very slight O'Connell effect was observed in this EB system, suggesting the presence of a hot spot. The best fit, with a temperature ratio of 1.1, yields a spot at 280 ± 60 deg and a size of 21 ± 11 deg.

The obtained values provide a good estimation of the potential of each EB system to become a good distance determination target. In general, the best targets should have low third light contribution and a luminosity ratio close to unity. On one hand, a strong third light contribution would lead to underestimating the

Table 2.3. Fundamental properties of the 24 EBs with W&D fits (see text for nomenclature). Targets selected for observation with GMOS at Gemini-North are highlighted.

Identifier [M31V]	Conf.[a]	$V^{\rm mean}$ [mag]	P [days]	i [deg]	e	ω [deg]	R_P/a[b]	R_S/a[b]	$T_{\rm eff,S}/T_{\rm eff,P}$	$(L_S/L_P)^B$	$(L_S/L_P)^V$	$(L_S/L_P)^D$	l_3^B	l_3^V	l_3^D
J00444528+4128000	**SD**	**18.854**	**11.543654±0.000211**	**78.0±1.3**	**0.0**	**–**	**0.556±0.009**	**0.277±0.002**	**0.453±0.033**	**0.0513±0.0003**	**0.0575±0.0004**	**0.0575 ±0.0004**	**0.0**	**0.0**	**0.0**
J00435515+4124567	D	19.164	6.816191±0.000067	89.1±4.4	0.105±0.010	327.4± 7.8	0.160±0.007	0.281±0.012	0.911±0.018	2.69±0.09	2.70±0.08	–	0.055±0.032	−0.005±0.030	–
J00442326+4127082	**D**	**19.242**	**5.752689 ±0.000037**	**87.3±2.4**	**0.189 ±0.019**	**51.3 ± 4.7**	**0.215±0.017**	**0.267±0.025**	**0.890±0.027**	**1.25 ±0.13**	**1.27±0.14**	**1.27 ±0.15**	**0.329 ±0.039**	**0.336±0.043**	**0.328±0.051**
J00451253+4137261	SD	19.366	2.358359±0.000010	75.4±3.0	0.0	–	0.369±0.023	0.372±0.007	0.885±0.020	0.80±0.08	0.82±0.09	0.82±0.12	0.285±0.056	0.308±0.059	0.325±0.070
J00443799+4129236	**SD**	**19.428**	**3.549696 ±0.000012**	**83.3±0.6**	**0.0**	**–**	**0.330±0.019**	**0.390±0.006**	**0.772±0.012**	**0.88 ±0.04**	**0.90±0.04**	**0.90 ±0.04**	**0.0**	**0.0**	**0.0**
J00442928+4123013	SD	19.475	3.168969±0.000006	86.4±2.5	0.0	–	0.329±0.014	0.403±0.005	0.857±0.011	1.17±0.05	1.19±0.05	1.19±0.06	0.042±0.035	0.027±0.032	0.022±0.034
J00450486+4137291	SD	19.536	3.094681±0.000013	75.7±3.0	0.0	–	0.316±0.021	0.390±0.008	0.787±0.015	1.01±0.12	1.03±0.12	1.03±0.13	0.016±0.098	−0.041±0.093	−0.033±0.096
J00451973+4145048	D	19.572	8.130670±0.000087	87.2±2.4	0.252±0.027	109.1± 1.8	0.216±0.014	0.149±0.012	0.894±0.016	0.34±0.06	0.35±0.06	0.34±0.07	0.041±0.077	−0.136±0.096	0.115±0.096
J00450051+4131393	D	19.756	5.211976±0.000044	81.7±1.2	0.040±0.015	120.0±14.1	0.128±0.005	0.349±0.011	0.993±0.005	7.67±0.35	7.74±0.38	7.73±1.47	0.063±0.025	0.069±0.024	0.055±0.086
J00444914+4152526	SD	19.772	2.626992±0.000010	72.5±1.5	0.0	–	0.340±0.015	0.384±0.005	0.957±0.026	1.20±0.09	1.21±0.09	–	0.003±0.046	0.009±0.047	–
J00442478+4139022	D	20.034	4.762310±0.000068	79.9±1.2	0.027±0.008	188.8±33.4	0.105±0.003	0.333±0.014	0.848±0.004	7.48±0.34	7.65±0.35	–	0.0	0.0	–
J00443610+4129194	**SD**	**20.038**	**2.048644 ±0.000006**	**70.6±1.7**	**0.0**	**–**	**0.290±0.018**	**0.369±0.007**	**0.946±0.020**	**1.51 ±0.18**	**1.52±0.18**	**1.52 ±0.22**	**0.067 ±0.034**	**0.051±0.032**	**0.016±0.047**
J00425907+4136527	D	20.060	5.874724±0.000069	81.0±1.1	0.163±0.016	70.8± 2.2	0.344±0.013	0.157±0.011	1.046±0.021	0.22±0.02	0.22±0.02	0.22±0.02	0.053±0.017	0.051±0.029	0.034±0.023
J00452554+4145035	SD	20.090	5.009412±0.000047	82.3±3.4	0.0	–	0.247±0.020	0.393±0.008	0.810±0.018	1.72±0.13	1.78±0.13	1.78±0.27	0.169±0.014	0.162±0.023	0.227±0.029
J00442722+4136082	SD	20.098	4.518795±0.000016	86.1±1.7	0.0	–	0.308±0.018	0.344±0.009	0.747±0.008	0.72±0.05	0.76±0.05	0.76±0.06	0.109±0.009	0.130±0.010	0.119±0.014
J00453244+4147425	SD	20.141	2.787856±0.000010	78.4±1.7	0.0	–	0.238±0.012	0.342±0.007	0.728±0.009	1.14±0.11	1.20±0.12	1.20±0.17	0.036±0.022	0.018±0.026	0.093±0.090
J00445935+4130454	SD	20.166	2.668419±0.000023	68.1±1.9	0.0	–	0.277±0.025	0.347±0.013	0.857±0.063	1.22±0.24	1.25±0.25	–	0.169±0.079	0.219±0.082	–
J00450537+4133402	SD	20.326	1.769903±0.000005	75.4±2.5	0.0	–	0.351±0.025	0.350±0.010	0.940±0.015	0.88±0.10	0.89±0.10	0.89±0.13	−0.055±0.110	−0.027±0.102	−0.037±0.117
J00432610+4142010	SD	20.340	4.274429±0.000065	75.9±3.6	0.0	–	0.206±0.027	0.413±0.014	0.838±0.028	3.15±0.77	3.23±0.79	–	0.243±0.043	0.309±0.061	–
J00445682+4131109	D	20.360	4.207679±0.000036	87.2±4.5	0.0	–	0.345±0.015	0.158±0.015	0.891±0.024	0.18±0.03	0.18±0.03	0.18±0.04	0.118±0.076	0.129±0.087	0.153±0.117
J00435082+4121517	D	20.367	2.176672±0.000011	79.6±4.1	0.0	–	0.305±0.026	0.358±0.031	0.789±0.019	0.89±0.18	0.93±0.19	–	0.245±0.074	0.211±0.091	–
J00425743+4137114	SD	20.388	1.916302±0.000008	73.9±2.9	0.0	–	0.364±0.019	0.379±0.006	0.921±0.014	0.94±0.11	0.96±0.11	–	0.165±0.063	0.219±0.070	–
J00425929+4138169	D	20.450	5.591515±0.000045	85.5±4.0	0.0	–	0.340±0.011	0.264±0.016	0.548±0.011	0.17±0.02	0.19±0.02	0.19±0.02	0.195±0.042	0.203±0.049	0.139±0.045
J00445011+4128069	**D**	**20.456**	**2.861046 ±0.000009**	**80.2±2.4**	**0.0**	**–**	**0.347±0.013**	**0.286±0.013**	**0.603±0.016**	**0.25 ±0.03**	**0.26±0.03**	**0.26 ±0.04**	**−0.012±0.090**	**−0.004±0.080**	**0.001±0.105**

[a] Configuration. (D): Detached, (SD): Semi–detached.

[b] R_P/a and R_S/a are the relative radii of the components, where a is the semi-major axis of the system.

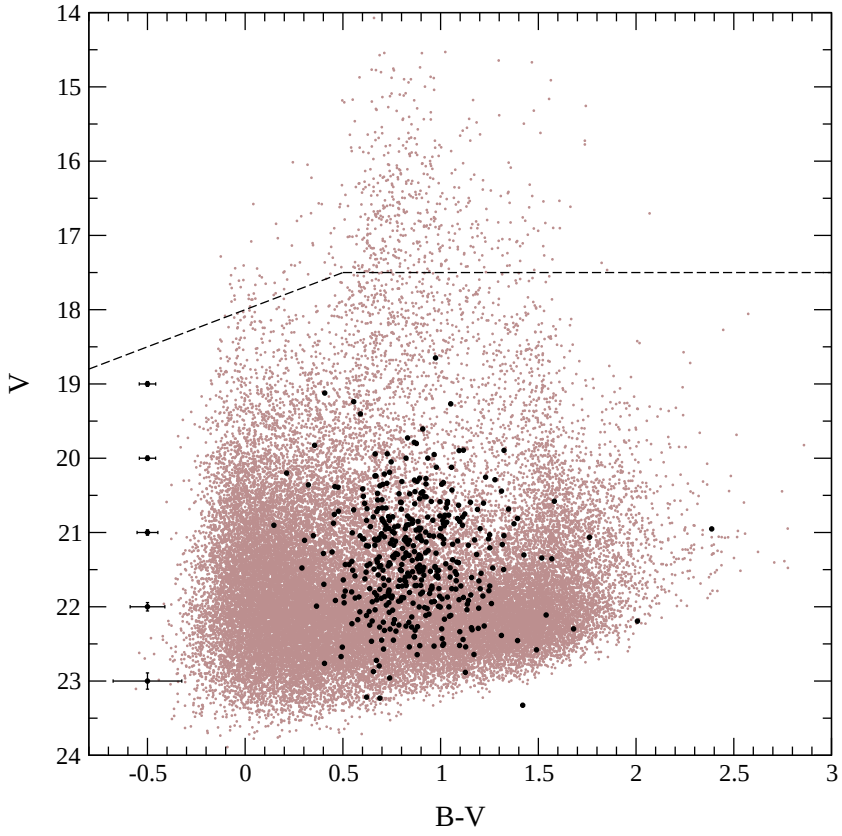

Figure 2.12. Color–magnitude diagram for 37 241 objects with photometric errors lower than 0.1 mag in both B and V in the reference catalog (gray dots) and 416 Cepheids (black circles). Stars above the dashed lines are saturated. Error bars on the left indicate the mean error, in magnitude and color, at different magnitude values.

observed standard magnitudes for the EB system. Although the third light can be modeled, the resulting values may have uncertainties that are large enough to have a sizeable negative effect on the accuracy of the distance determination (Wilson & Wyithe, 2003). On the other hand, EBs with luminosity ratios close to unity will have spectra with visible lines for the two components, thus making the determination of accurate fundamental properties possible.

2.4.2 Cepheids

Although the main targets of this work are EBs, the variable stars most commonly used for distance determination are Cepheids (Chap. 1). The visual inspection of the variable star catalog revealed a total amount of 416 Ceheids with $\sim$ 250 measurements in both B and V passbands. The standard errors in the V (and $B-V$) passband range from 0.03 mag (0.04 mag) at $V \sim 19$ mag to 0.11 mag

(0.18 mag) at $V \sim 23$ mag (Fig. 2.12). As will be shown in Sect. 5.3.1, the line-of-sight absorption is computed from the observed color. Therefore, it is obvious that fainter Cepheids will have large uncertainties in their absolute magnitudes and will have low significance in the distance determination to M 31. However, their periods are still very accurate and therefore, the full sample can be used to study the completeness and the presence of any possible bias (Sect. 5.1). So, the entire Cepheid sample was selected to determine the characteristics of the Cepheid population (Chap. 5).

3 Spectroscopy and spectrophotometry

The second necessary ingredient to fulfill the project goals is the acquisition of spectra. Spectral information is essential because it provides another basic ingredient for distance determination: radial velocities. Therefore, spectroscopy was obtained for five of the 24 EBs selected in Sect. 2.4.1 as suitable candidates for distance determination (Sect. 3.1). Observations were carried out with the Gemini-North telescope and the GMOS detector. The field of view includes four Cepheids, however the S/N and the spectral resolution of the acquired spectra is too low for extracting meaningful information.

Following the procedure used to determine a distance to LMC (Sect. 1.3.2), we obtained spectrophotometry of two of the main targets with the Hubble Space Telescope (HST). Unfortunately, the low quality of the acquired spectra and several technical problems prevented the use of this method to determine the temperature of the components. As shown in Sect. 4.1, the GMOS spectra can also be used to determine the temperature of the components through the fitting of synthetic models. Therefore, the spectrophotometric observations were used to ensure the consistency of the temperature determination (Sect. 3.2).

3.1 Spectroscopy

3.1.1 Observations

The magnitude of the brightest EBs in the photometric catalog is $V \sim 19$ mag. In order to obtain spectroscopy of such objects with the required resolution and S/N for accurate radial velocity determinations a 8–10 m class telescope is required. Considering the position of M 31 in the Northern Hemisphere, we selected the

Table 3.1. Observed targets within the GMOS field of view with the corresponding mean magnitudes and period.

Identifier [M31V]	Var. type	$V^{\rm mean}$ [mag]	$B^{\rm mean}$ [mag]	Reference time [HJD]	Period [days]
J00444528+4128000	EB	18.854 ± 0.021	18.931 ± 0.011	2451814.4644	11.543696
J00442326+4127082	EB	19.242 ± 0.031	19.331 ± 0.021	2452546.4031	5.752609
J00443799+4129236	EB	19.428 ± 0.020	19.348 ± 0.013	2452204.3793	3.549696
J00443610+4129194	EB	20.038 ± 0.031	19.920 ± 0.020	2452908.7081	2.048644
J00445011+4128069	EB	20.456 ± 0.031	20.349 ± 0.011	2452910.5780	2.861049
J00442183+4129492	Cepheid	20.670 ± 0.030	21.391 ± 0.021	2452546.3920	8.246601
J00442951+4130314	Cepheid	21.098 ± 0.035	21.911 ± 0.035	2452546.7483	7.772483
J00444374+4128354	Cepheid	21.499 ± 0.047	22.822 ± 0.068	2452550.7378	14.650850
J00443379+4125219	EB	21.550 ± 0.062	21.333 ± 0.048	2452203.5319	1.739561
J00443928+4130078	Cepheid	21.600 ± 0.068	22.648 ± 0.058	2452906.4932	8.505991

8 m telescope Gemini-North (in Mauna Kea, Hawaii) since it has a multi-object spectrograph (GMOS) that fulfills our requirements.

We used the GMOS spectrograph with a custom mask designed to deliver spectroscopy of a number of targets in a $5\farcm5 \times 5\farcm5$ field of view. The instrument was set to the highest possible resolution of R=3744 ($\sim$ 80km s^{-1} per resolution element) using a slit width of $0\farcs5$. The observations were performed in service mode during four GMOS runs in September, October and November 2004 and February 2005 (program ID GN-2004B-Q-9).

Since the GMOS field of view ($5\farcm5 \times 5\farcm5$) is much smaller than the INT photometric field of view ($33\farcm8 \times 33\farcm8$), a selection of the optimum area to be studied was performed. Considering the spatial distribution of the EBs selected as suitable candidates for distance determination (see Sect. 2.4.1), a field containing five of the selected EBs at the South-East of the studied region was chosen (Fig. 3.1). Together with the selected binaries, four Cepheids and a fainter EB happen to be within the GMOS field of view (Fig. 3.2) and were also selected for observation (Table 3.1).

The observation strategy consisted in the acquisition of two spectra with an exposure time of 2050 sec. Between the two spectra, a spectroscopic flat-field image and a wavelength calibration arc images were obtained. The two spectra were combined in the data reduction process (Sect. 3.1.2) to produce a combined spectrum. A total amount of eight exposures of 4100 sec and one (obtained in February 2005) with a shorter exposure time (3240 sec) were obtained. All the observations were timed to cover both quadratures of two of the brightest EBs in the field: M31V J00443799+4129236 and M31V J00442326+4127082. The brightest EB (M31V J00444528+4128000) was excluded from the timing constraints because it presents some intrinsic variability and it was estimated (and confirmed afterwards) to be a single-line system from the light curve analysis (Sect. 4.1.3). Therefore, each one of the two main targets has, at least, four observations at

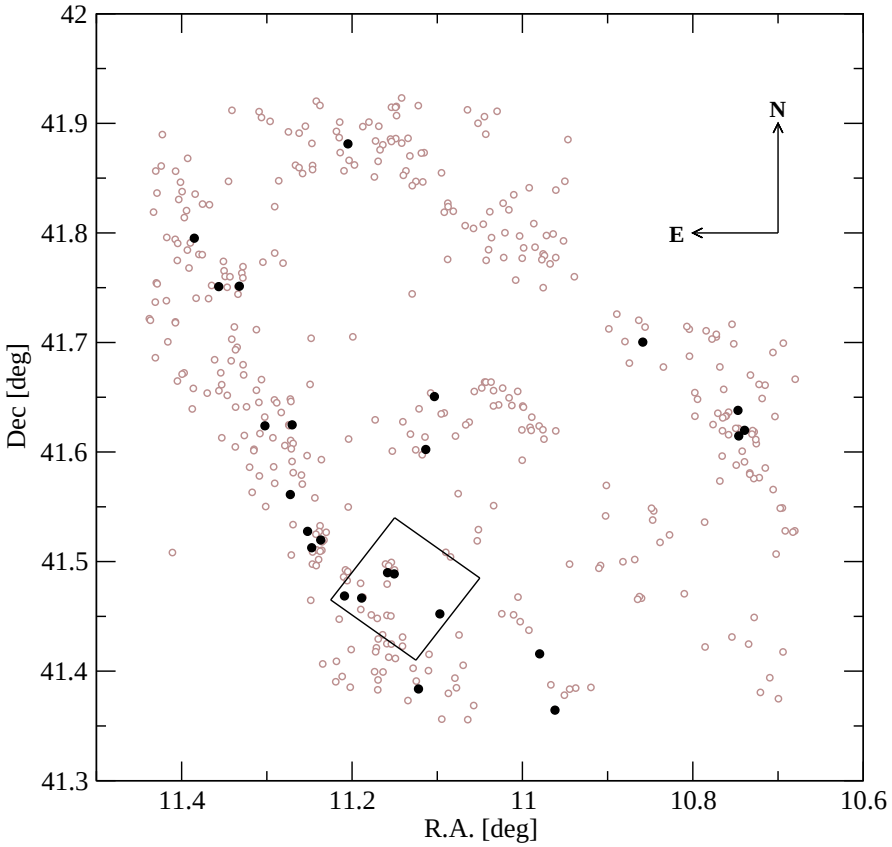

Figure 3.1. Position of the 437 EBs identified in the photometric catalog (gray circles) and the 24 eclipsing binaries most suitable for distance determination (black circles). The area of $5\farcm5 \times 5\farcm5$ selected for Gemini-N/GMOS observations is also indicated (square).

quadratures (two observations per quadrature) and the remaining observations at random phases.

3.1.2 Data reduction

We carried out the reduction of the raw CCD frames with the IRAF Gemini package version 1.7. For each GMOS observing run, several bias (and other calibration data) are automatically obtained out of the scientific program time. From the various possible GMOS configurations, our observations used a binning of 2×2 pixels and the entire field of view was read out. All the bias frames obtained in the same GMOS run, and having the same configuration as the observations, were combined (with a mean and 3σ clipping) to produce a master bias. The corresponding master bias was subtracted from each exposure image.

Before any further corrections could be applied, the position of the spectra in

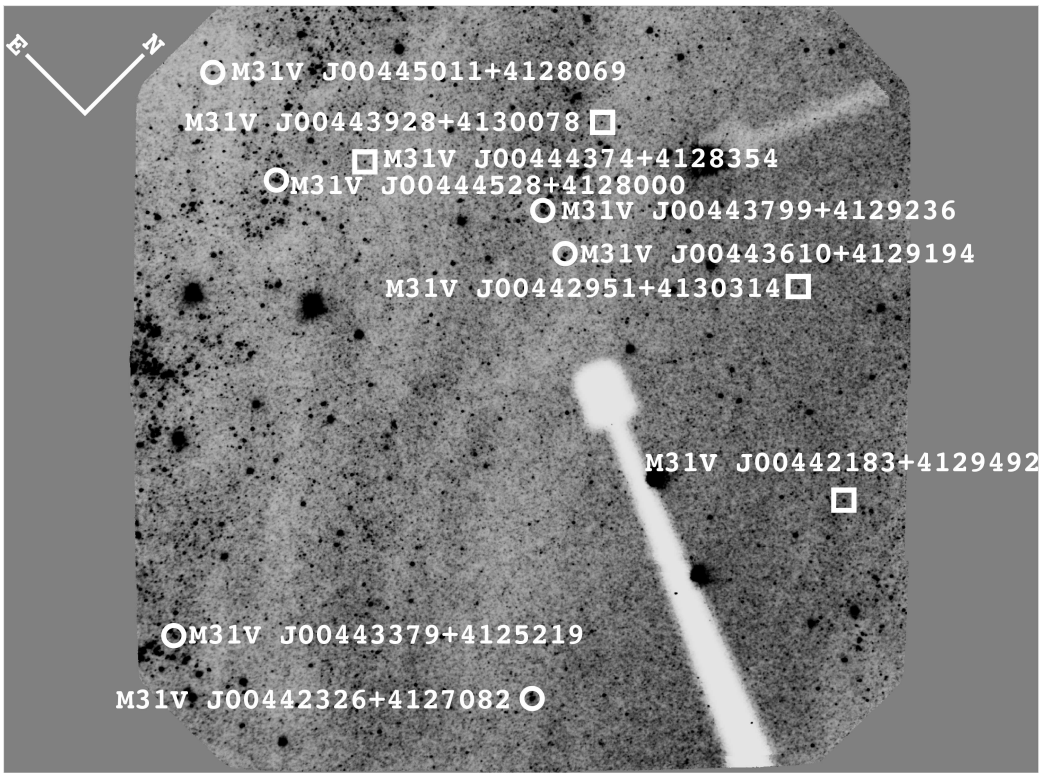

Figure 3.2. GMOS field of view with the 6 EBs (white circles) and 4 Cepheids (white squares) selected for observation. The white area is the wavefront sensor.

the detector had to be identified. Although the relative position between spectra is known (from the custom mask), the exact position of the spectra on the detector can vary slightly from run to run. Therefore, for each exposure, we first reduced the arc images to derive the displacement of the spectra with respect to the center of the slit.

Once the offsets were known, the wavelength calibration arc and the two spectra in each exposure were flux-corrected with the corresponding flat-field image. Bad pixels and cosmic ray hits were automatically identified (from the neighboring pixels) and each slit was extracted.

Calibration arcs were obtained with a Cu-Ar (Copper-Argon) lamp, providing a wavelength calibration with less than 0.01 nm rms. The wavelength-calibrated spectra were sky subtracted (using the neighboring pixels) and extracted to obtain one dimensional spectra. The across dispersion aperture used to extract each exposure (between 1″and 2″) was found iteratively to obtain the lowest number of bad pixels and the best fit to the spectrum trace. The two one dimensional spectra of each exposure were finally combined (with a mean) and normalized (with a polynomial fit to the continuum), providing the final 4100-second exposures.

With a sampling of about 2.5 pixels per resolution element, all the spectra

Table 3.2. Type of variability, wavelength range, position gaps and signal-to-noise range for each one of the targets observed with GMOS.

Name [M31V]	Type	Range [nm]	Blue gap [nm]	Red gap [nm]	S/N
J00444528+4128000	EB	360.8 – 506.8	408.2 – 409.4	457.4 – 458.5	16 – 30
J00442326+4127082	EB	387.6 – 533.6	435.0 – 436.2	484.2 – 485.3	15 – 35
J00443799+4129236	EB	389.2 – 535.2	436.6 – 437.8	485.8 – 486.9	14 – 39
J00443610+4129194	EB	391.6 – 537.6	439.0 – 440.2	488.2 – 489.3	8 – 24
J00445011+4128069	EB	353.5 – 499.5	400.9 – 402.1	450.1 – 451.2	6 – 12
J00442183+4129492	Cepheid	420.0 – 566.0	467.4 – 468.6	516.6 – 517.7	5 – 12
J00442951+4130314	Cepheid	415.5 – 561.5	462.9 – 464.1	512.1 – 513.2	4 – 9
J00444374+4128354	Cepheid	370.3 – 516.3	417.7 – 418.9	466.9 – 468.0	1 – 6
J00443379+4125219	EB	349.4 – 495.4	396.8 – 398.0	446.0 – 447.1	3 – 6
J00443928+4130078	Cepheid	395.1 – 541.1	442.5 – 443.7	491.7 – 492.8	2 – 6

include the Balmer lines (except Hα at 656.3 nm). The wavelength range was chosen to include Balmer lines because they are almost the only visible (and the strongest) lines for late-O and early-B stars (see Fig. 3.3). Due to the instrument design, the wavelength ranges vary slightly, depending on the position of each EB in the field of view (Table 3.2). In addition, there are two inter-chip gaps in the spectral direction that also vary with the position of each target. For some of the observed targets, one of these gaps happens to be close to the Hβ Balmer line at 486.1 nm.

The spectra obtained (Fig. 3.3) have a S/N ratio that depends on the magnitude of the target and the phase of observation (Table 3.2). Considering the quality of the spectroscopic data acquired, we only selected the five brightest EBs (suitable candidates for distance determination) for further analysis (Chap. 4).

3.2 Spectrophotometry

3.2.1 Observations

Spectrophotometric observations were performed with the Advanced Camera for Surveys (ACS) on board the HST. Two HST orbits were granted in the year 2005 to obtain spectrophotometry of two of the main EBs in the GMOS field of view: M31V J00442326+4127082 and M31V J00443799+4129236. Two ACS detectors were used to observe the desired wavelength interval (from 115 to 1050 nm): the Solar Blind Channel (SBC), with the PR110L prism, and the High Resolution Camera (HRC), with the PR200L prism and the G800L grism (see Table 3.3 for details).

Observations were finally performed in September and November 2006 (Ta-

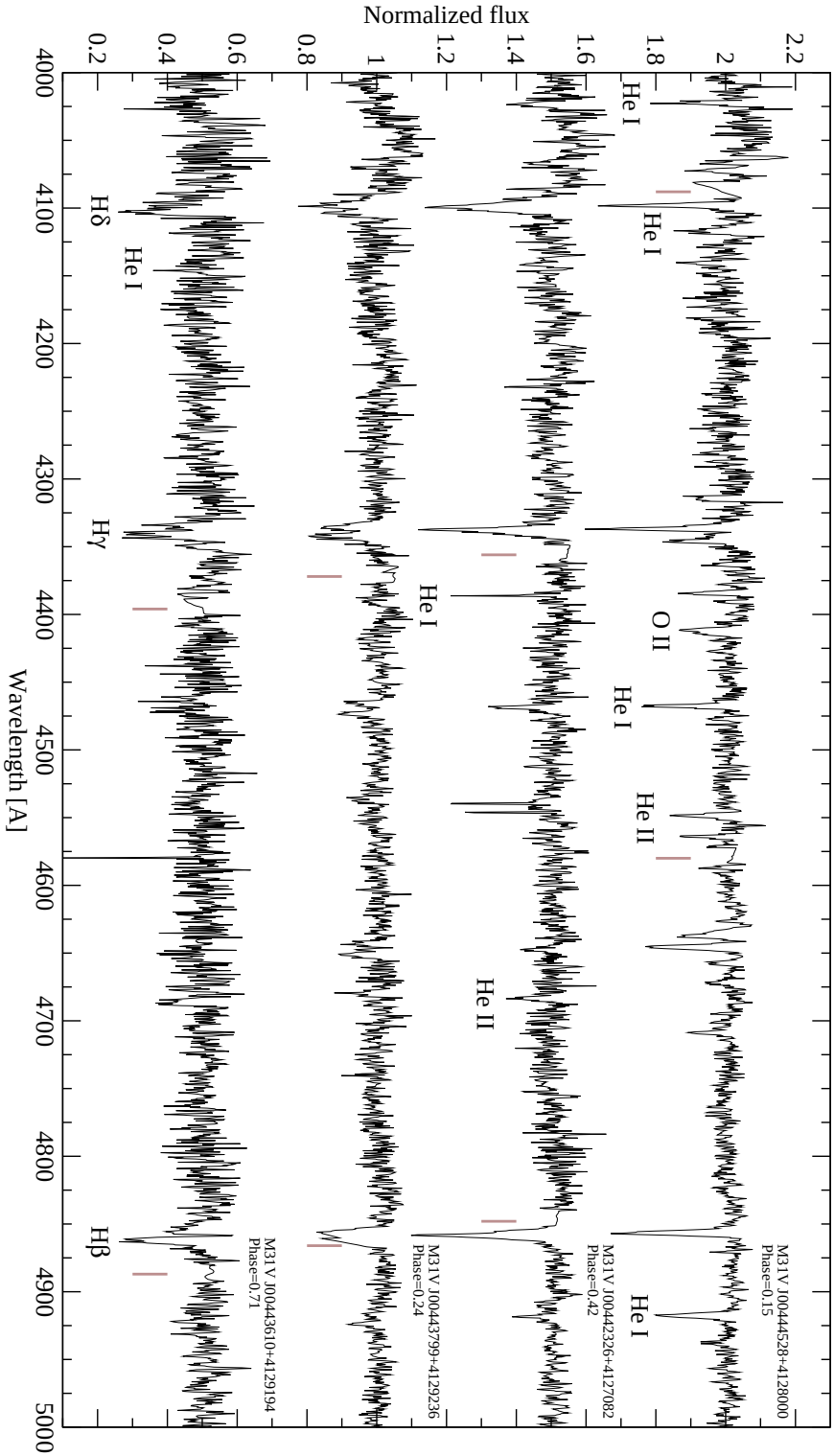

Figure 3.3. Highest quality spectra for the four brightest EBs. The most representative spectral lines are identified, as well as the gaps in the spectra (gray lines).

Table 3.3. Characteristics of the HST instrumentation used to obtain spectrophotometry.

Detector	Field of view	Disperser	Wavelength interval [nm]	Minimum resolution $\lambda/\Delta\lambda$@[nm]	Maximum resolution $\lambda/\Delta\lambda$@[nm]
SBC	$34\farcs6 \times 30\farcs5$	PR110L	115 – 180	40@180	300@115
HRC	29" × 26"	PR200L	170 – 390	13@390	135@170
HRC	29" × 26"	G800L	550 – 1050	70@550	130@1050

Table 3.4. Observations obtained with the ACS camera on board the HST.

Target	Date observed	Orbital phase	Detector	Direct image		Prism/Grism image	
				Filter	Exposure time [seconds]	Disperser	Exposure time [seconds]
[M31V]	[2006]						
J00443799+4129236	September 3	0.77	HRC	F606W	40	G800L	2×117.5
J00443799+4129236	September 3	0.76	HRC	F330W	138	PR200L	2×101
J00443799+4129236	September 17	0.75	SBC	F125LP	113	PR110L	711
J00442326+4127082	November 29	0.56	SBC	F125LP	113	PR110L	711

ble 3.4). Of the two granted targets, only M31V J00443799+4129236 was completely observed, while the other target (M31V J00442326+4127082) was observed only with SBC. Although the underlying reason was never revealed to us, the most likely explanation for the missing data is a failure in ACS, which ceased observations just a few weeks after our run. In addition, although observations were timed to observe both targets at quadratures, the SBC observation of M31V J00442326+4127082 was obtained in the middle of the secondary eclipse (Table 3.4), decreasing the signal of the obtained data and reducing the scientific outcome.

For each spectrophotometric observation a direct image of the selected field of view was obtained (Table 3.4). The obtained data was used in the reduction process (Sect. 3.2.2) to obtain the required zero-points for an accurate wavelength calibration. In addition, for the HRC observations, the spectroscopic data was obtained in two consecutive exposures, enabling the identification and removal of cosmic ray hits. Both exposures were combined in the data reduction process (Sect. 3.2.2).

3.2.2 Data reduction

The data obtained with ACS are automatically processed by the CALACS package. Correction for overscan, bias, darks, flats and some cosmic ray hits is performed. The resulting images were the initial products retrieved from MAST (Multimission Archive Space Telescope science institute) for further analysis. Standard routines in Source Extractor (Bertin & Arnouts, 1996), IRAF (version 2.13.beta) and PyIRAF[1] (version 1.4), including the specific packages for ACS

[1]PyIRAF is a product of the Space Telescope Science Institute, which is operated by AURA for NASA.

data reduction (Multidrizzle and aXe), were used. The reduction procedure is somewhat different for each one of the three different dispersers (HRC G800L, HRC PR200L and SBC PR110L) and, therefore, each procedure is explained separately. In the three cases, calibration and standardization data are provided by the STECF[2] (Space Telescope European Coordination Facility).

3.2.2.1 HRC G800L

The HRC detector is considerably out of the optical axis of HST. Therefore, the obtained images are distorted and had to be corrected (with Multidrizzle). Since two grism images were obtained, the cosmic ray hits were also automatically identified and marked. The lack of contaminating stars in the G800L spectra (present in other images) allowed the application of Multidrizzle with the images obtained just after the CALACS automatic pipeline (either direct images and spectra).

The following step was the identification of the stars in the field. Source Extractor was run on the corrected direct image, identifying the magnitude and position of the EB and nearby companions. Once the stars were identified on the direct image, the spectroscopic images (Fig. 3.4) were background subtracted with a master sky image and bad pixels were automatically identified and removed.

Once the spectra are free from instrumental defects, the extraction of the individual spectra can be performed. The direct image was used to define the reference PSF and zero-point of the wavelength calibration. With the zero-point and the dispersion coefficients provided by STECF, the spectra were wavelength calibrated. The wavelength calibrated spectra were flat fielded (using a wavelength dependent flat field), extracted from the individual exposures and combined to form a single two dimensional spectrum. Each one of the two dimensional spectra was extracted by averaging all the values within 3 times the PSF FWHM and transformed into a one dimensional spectrum. The last step in the reduction of G800L spectra is the transformation of the instrumental flux values into standard ones (using standard calibration data). The applied flux transformations were obtained from two white dwarfs (2MASS J12570233+2201526 and 2MASS J05053062+5249519) and are reported (by STECF) to be accurate to within 5% for all the points between 600 and 900 nm (region between dashed lines in Fig. 3.4).

3.2.2.2 HRC PR200L

The standard procedures in PyIRAF are unable to combine observations obtained in prism mode with HRC. Therefore, considering the lack of atmosphere and the excellent pointing accuracy (with jitters around 6 milliarcsec or 0.2 pixels),

[2] Needed calibration data was obtained from:
`http://www.stecf.org/instruments/ACSgrism/`

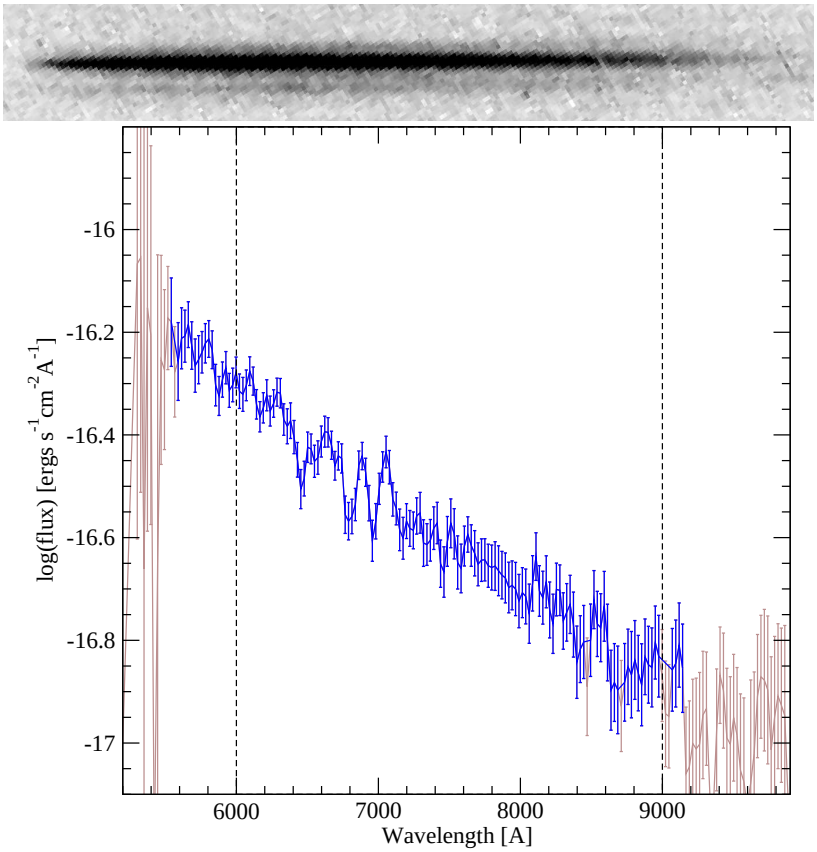

Figure 3.4. Spectroscopic observations obtained with HRC G800L. **Top:** Raw spectrum of M31V J00443799+4129236. **Bottom:** Reduced spectrum (gray lines) with the points having a total error (calibration and random) below 20% indicated (black lines). The area with a calibration error in flux below 5% is also indicated (within the dashed lines).

the pair of HRC prism images were combined (with a weighted mean) after the CALACS automatic procedure and before the correction for image deformation. The combination method is optimal in the sense that the noise is reduced and, at the same time, diminishes the effect of cosmic ray hits.

Unfortunately, the PR200L spectrum of the studied binary is severely contaminated by the presence of a nearby companion (Fig. 3.5). Note that the G800L spectrum is not affected by this contaminating star because the dispersion direction is different. In addition, the contaminating star is much fainter in the optical region, where G800L data was obtained. The instrumental design of the PR200L prism also makes that most of the flux is detected at longer wavelengths and the short wavelength region of the binary spectrum is close to the long wavelength region of the contaminating star, being both equally bright (Fig. 3.5).

In order to avoid negative effects on the extraction of the desired spectrum,

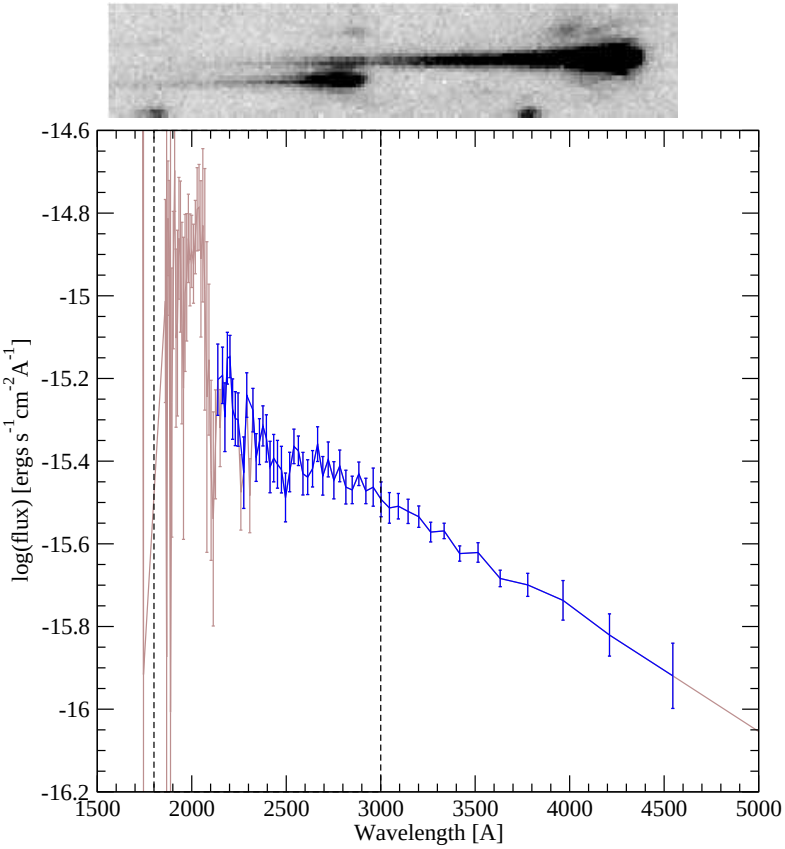

Figure 3.5. Spectroscopic observations obtained with HRC PR200L. **Top:** Raw spectrum of M31V J00443799+4129236. **Bottom:** Reduced spectrum (gray lines) with the points having a total error (calibration and random) below 20% indicated (black lines). The area with a calibration error in flux below 5% is also indicated (within the dashed lines). The effect of contamination is clearly observed at short wavelengths.

the contaminating star was subtracted. Another star in the field of view was used to subtract the contaminating star. In order to ensure that the flux distributions of both stars were similar, the instrumental photometry obtained in the three direct images (with Source Extractor) was used to select the most suitable star. Even when the contaminating star was subtracted, the spectral region affected by contamination was unsuitable for flux determination, but this process ensured that the extraction direction of the spectrum of the EB (automatically detected for the extraction algorithm) is accurate.

Once the binary spectrum was cleaned from contamination, the PR200L data reduction was similar to that used for G800L. The geometric distortions were corrected (with Multidrizzle) and the stars in the field were identified (with Source Extractor). Contrary to the G800L reduction, each individual spectrum was background subtracted from the neighboring pixels (with a median) since no master

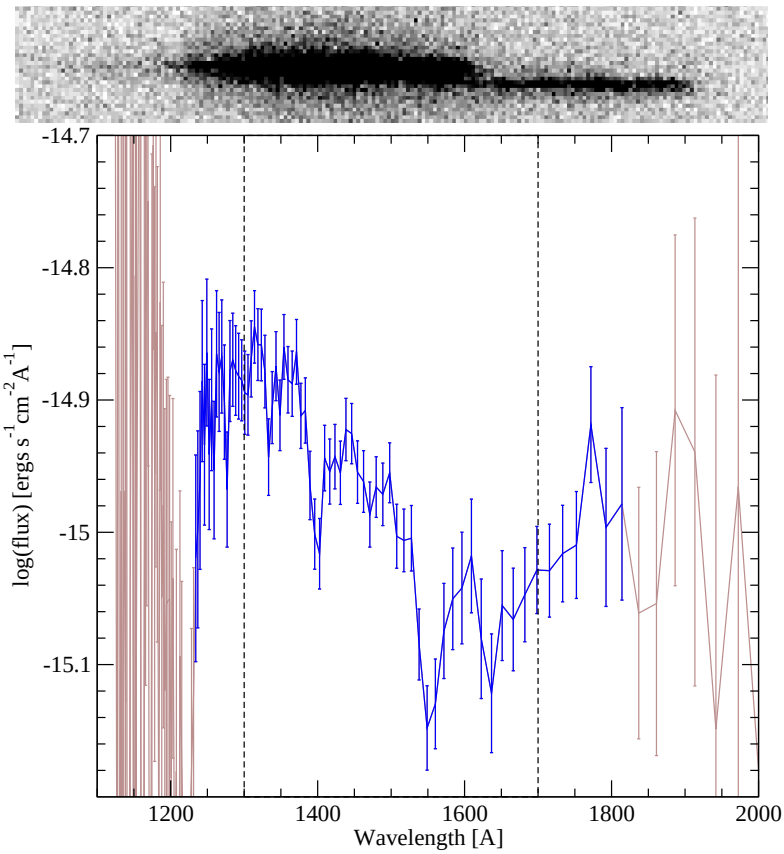

Figure 3.6. Spectroscopic observations obtained with HRC PR110L. **Top:** Raw spectrum of M31V J00443799+4129236. **Bottom:** Reduced spectrum (gray lines) with the points having a total error (calibration and random) below 20% indicated (black lines). The area with a calibration error in flux below 5% is also indicated (within the dashed lines).

sky image is available. The background-subtracted spectra were finally extracted (with an aperture of 0.″5), transformed into one dimensional data, wavelength calibrated and converted to flux standard values using standard calibration data. The applied flux transformations are reported (by STECF) to be accurate within 5% from 180 to 350 nm, but the contaminating star makes that errors larger than 20% are obtained for wavelengths shorter than 215 nm (Fig. 3.5).

3.2.2.3 SBC PR110L

The data reduction process of both targets observed with the SBC detector followed similar steps. The only exception is the treatment of contamination for the M31V J00443799+4129236 data. Contrary to HRC PR200L data, the spectrum of the observed EB is only slightly affected by the contaminating star (Fig. 3.6).

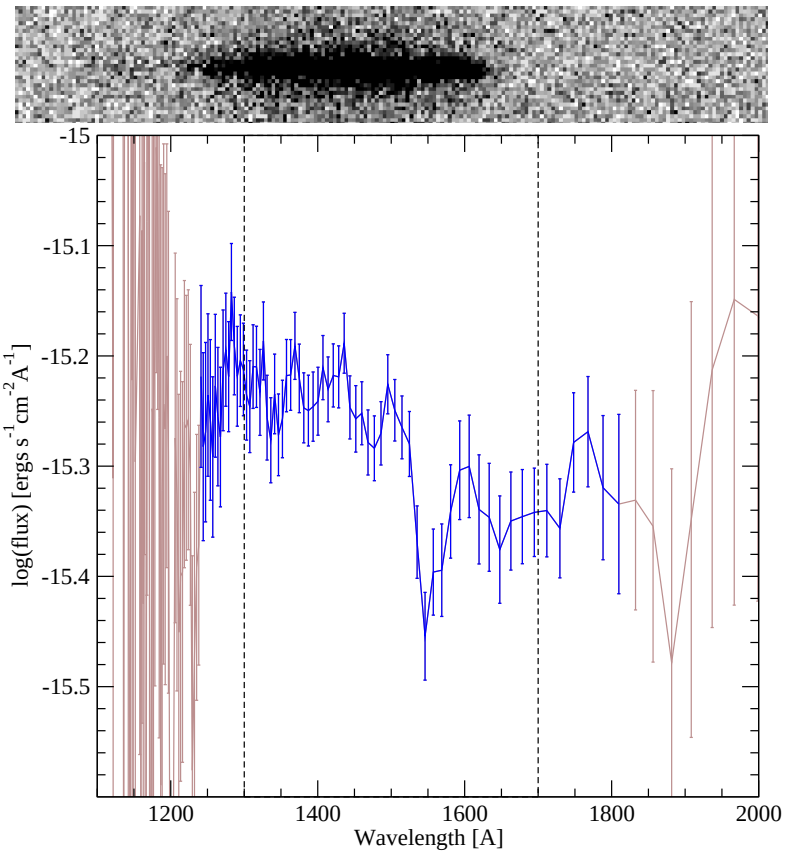

Figure 3.7. Spectroscopic observations obtained with HRC PR110L. **Top:** Raw spectrum of M31V J00442326+4127082. **Bottom:** Reduced spectrum (gray lines) with the points having a total error (calibration and random) below 20% indicated (black lines). The area with a calibration error in flux below 5% is also indicated (within the dashed lines).

Therefore, the subtraction procedure (described for the PR200L data) provided a clean spectrum where the contamination from the nearby companion is well within the observational errors.

For both targets the geometric distortions were corrected (with Multidrizzle) and the stars in the field were identified (with Source Extractor). Contrary to previous reductions, an offset had to be applied to the obtained position of stars in order to use the standard wavelength calibration coefficients. The reason is that coefficients are valid for images taken with the F165LP filter, whereas our direct images were obtained with the F125LP filter. According to the STECF guidelines[3], the required offset in the position of stars is 0.97 pixels in the along dispersion direction and −2.44 pixels in the across dispersion direction. After

[3]Offsets are available at:
`http://www.stecf.org/instruments/ACSgrism/calibration/sbc_pr110l.php`

careful examination of the resulting spectra, it was concluded that the SiIV line at 140 nm and the CIV line at 155 nm were displaced by ∼1 pixel. On the contrary, after the application of the recommended across dispersion offset, it was observed that the extracted spectrum was well centered in the extraction zone. Therefore, no offset in the along dispersion direction was applied and the recommended offset in the across dispersion direction was used.

Once the observed stars were properly identified in the field, the spectra were background subtracted (from the neighboring pixels), and transformed into one-dimensional spectra with an aperture of $0''.5$. The observations were finally transformed into flux values with the standard calibration data (Fig. 3.6 and Fig. 3.7). The applied flux transformation is reported (by STECF) to be accurate within 5% for all the values between 130 nm and 170 nm.

4 Eclipsing binaries⋆

Five of the 24 EBs selected as suitable distance indicators (Sect 2.4.1) were observed with GMOS at Gemini-North (Sect. 3.1.1). The preliminary analysis performed (Sect. 2.4.1) indicates that two of the observed targets are optimum for obtaining a precise distance determination to M 31: M31V J00443799+4129236 and M31V J00443610+4129194. Therefore, both EBs were modeled in order to determine the physical properties of their components (Sect. 4.1) and to derive a direct distance to M 31 (Sect. 4.2). Two of the other observed targets have some particular characteristics that diminish their value for distance determination. One of them is a single-line EB (M31V J00444528+4128000) and the other one has a strong third light contribution (M31V J00442326+4127082). In spite of that, these EBs were also modeled in order to constrain the fundamental properties of massive stars in M 31 (Sect. 4.1). The fifth target observed with GMOS (M31V J00445011+4128069) is the faintest target in Table 2.3 and, after thorough investigation, no meaningful results could be obtained because of the low signal-to-noise ratio (S/N) of the obtained spectra (Table 3.2). Therefore, future observations with a larger telescope are required for this target.

In order to facilitate the identification to the reader, shorter identifiers have been used to refer to the four analyzed EBs (Table 4.1). According to the number of system components, the two double-line EBs have been referred to as SB2A and SB2B, the single-line EB as SB1 and the triple-line EB as SB3.

Table 4.1. Equivalence between the identifier in the variable star catalog and the shorter name given in the course of the present chapter.

M31V J00443799+4129236	SB2A
M31V J00443610+4129194	SB2B
M31V J00444528+4128000	SB1
M31V J00442326+4127082	SB3

⋆Part of the contents of this chapter were published in Ribas et al. (2005).

4.1 Physical properties

As in the case of the selection of targets (Sect. 2.4.1), each EB needs to be modeled as a particular case and a specific approach was followed for each one of them. In general, the treatment of all the targets consists of the following steps:

- Acquisition of RVs from the observed spectra,
- Determination of the masses and radii of the components from the modeling of the light and the RV curves,
- Determination of the temperature of the components and line-of-sight absorption, and
- Comparison with stellar evolutionary models.

The detailed approach used for each one of the four studied targets is explained below.

4.1.1 M31V J00443799+4129236 (SB2A)

4.1.1.1 Radial velocities

For double-line EBs, RV determinations involve the precise determination of the center of the (usually) blended spectral lines. To derive RVs of these stars, we considered several approaches on both spectral disentangling and two-dimensional cross-correlation. We carried out numerous tests with the spectral disentangling codes TANGLE (Harries et al., 2003) and KOREL (Hadrava, 1995), and considering different wavelength intervals. Using a grid search method we observed that the obtained solutions had a relatively large spread and it was not possible to establish a definitive solution because of the noisy χ^2 surface.

Alternatively, we used the TODCOR two-dimensional cross-correlation algorithm (Zucker & Mazeh, 1994). We calculated individual RVs for each spectrum by cross-correlating with synthetic templates from Kurucz ATLAS9 models[1] and the TLUSTY libraries (OSTAR2002 and BSTAR2006) of Lanz & Hubeny (2003, 2007)[2]. In both sets of models we considered templates with solar metallicity, different temperatures and gravities (Fig. 4.1), and rotational velocities in steps of 40 km s^{-1}, starting at 80 km s^{-1} (the wavelength resolution of the spectra is $\sim$ 80 km s^{-1}). The microturbulent velocity was set to 2 km s^{-1} for the ATLAS9 and BSTAR2006 models and to 10 km s^{-1} for the OSTAR2002 models, since these velocity values provide the maximum temperature and gravity coverage.

[1] Available at: `http://kurucz.cfa.harvard.edu/`
[2] Available at: `http://nova.astro.umd.edu/`

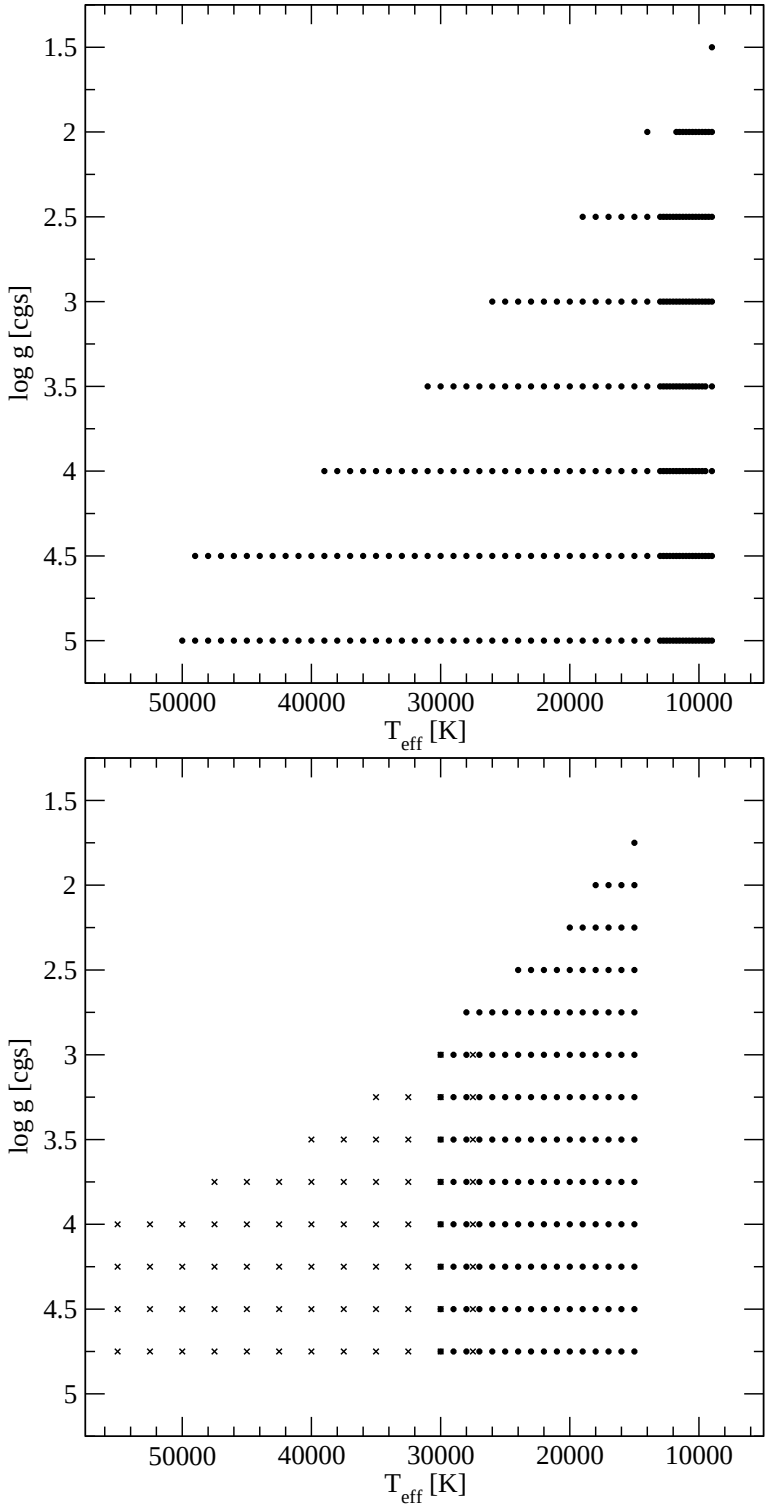

Figure 4.1. Effective temperature and gravity coverage for the two sets of models used for RV determination. **Left:** Kurucz ATLAS9 models. **Right:** TLUSTY OSTAR2002 (crosses) and BSTAR2006 models (circles).

Table 4.2. Radial velocity determinations for the EB M31V J00443799+4129236 (SB2A).

Time [HJD]	Phase	Primary [km s^{-1}]	Secondary [km s^{-1}]
2 453 262.874	0.1812	-338.1± 7.5	88.4± 7.5
2 453 319.879	0.2403	-349.1± 7.6	116.4± 6.2
2 453 260.910	0.6278	-52.9±10.8	-382.0±11.7
2 453 321.820	0.7871	10.5±13.9	-426.4±10.2
2 453 321.872	0.8016	-1.1± 9.3	-417.9± 8.6

The RVs obtained with TODCOR depend on the pair of synthetic templates used. Given the huge number of possible pairs of models resulting from the TLUSTY and ATLAS9 grids, two different procedures were used to determine the pair of models providing the best synthetic templates. The first procedure used the values derived from the light curve fitting (Sect. 2.4.1) and the observed colors $(B-V)$ to determine preliminary temperatures, surface gravities and rotational velocities for an initial pair of models. The RVs derived from these models were used to disentangle the observed spectra and to determine a temperature for each component (see Sect. 4.1.1.3). The resulting temperatures and gravities were then used to choose the final pair of models, to compute the corresponding RVs and to derive the fundamental properties of the studied stars. The second procedure (further explained in Sect. 4.1.2.1) consisted in computing the RVs with several pairs of models. The pair of models providing velocities that best fit to a RV curve model was considered to be the optimum pair. In both cases, the obtained RVs were corrected to the heliocentric reference frame using standard IRAF routines.

Both procedures provide equivalent results, and the RVs computed with the first procedure (involving disentangling) were adopted for SB2A (Table 4.2). Of the nine observed spectra, only five are shown in Table 4.2. The remaining spectra (phases are shown in Fig. 4.2) were excluded during the W&D fit by sigma clipping (see Sect. 4.1.1.2). We found that, in general, rejected observations were obtained during eclipses or correspond to the spectrum having a shorter exposure time (observed in February 2005, Sect. 3.1.1). In both cases TODCOR failed to identify a maximum of correlation in these spectra.

4.1.1.2 Mass and radius determination

The light and RV curves were modeled using the W&D code in order to derive the individual masses and radii of the components of each studied EB. Initial tests suggested that the light and RV curves should be modeled separately because of the very few RV measurements available and the possibility of inducing a bias in the mass ratio of the studied systems. Therefore, the light curve solutions of

Table 4.3. Fundamental properties of M31V J00443799+4129236 (SB2A) derived from the analysis with W&D.

System properties				
B magnitude at maximum light ($B_{\max}$)[a]	19.19±0.02			mag
V magnitude at maximum light ($V_{\max}$)[a]	19.27±0.02			mag
Period (P)	3.549694±0.000010			days
Time of minimum ($t_{\min}$)	2 452 204.421±0.003			HJD
Inclination (i)	89.3±1.8			deg
Systemic velocity (γ)	-173±4			km s^{-1}
Semi-major axis (a)	33.0±0.7			$R_\odot$
Mass ratio ($q = \mathcal{M}_S/\mathcal{M}_P$)	0.65±0.03			
Temperature ratio ($T_{\mathrm{eff},S}/T_{\mathrm{eff},P}$)	0.817±0.015			
Flux ratio in B ($F_{B,S}/F_{B,P}$)[a]	0.49±0.02			
Flux ratio in V ($F_{V,S}/F_{V,P}$)[a]	0.50±0.02			
Flux ratio in V_{DIRECT} ($F_{D,S}/F_{D,P}$)[a]	0.50±0.03			
Component properties	Primary		Secondary	
Radius (R)	13.1±0.3	$R_\odot$	11.3±0.3	$R_\odot$
Mass ($\mathcal{M}$)	23.1±1.3	$M_\odot$	15.0±1.1	$M_\odot$
Surface gravity ($\log g$ in cgs)	3.57±0.03		3.51±0.04	
Radial velocity semi-amplitude (K)[b]	185±6	km s^{-1}	285±6	km s^{-1}
Synchronized rotational velocity ($v_{\mathrm{sync}} \sin i$)	187±4	km s^{-1}	161±4	km s^{-1}

[a] Out of eclipse average: $\Delta\phi = [0.14 - 0.36, 0.64 - 0.86]$

[b] Including non-Keplerian corrections

Sect. 2.4.1 were used as the initial values for the RV curve fits. The obtained results were then used to fit the light curves. Fitting was carried out iteratively until full consistency was achieved.

For each light curve fit, the procedure described in Sect. 2.4.1 was followed. In the case of RVs, the adjustable parameters were the orbital semi-major axis (a), the mass ratio (q), and the systemic velocity (γ). Convergence in the fits was reached rapidly, and tests from different starting points indicated the uniqueness of the solution. For each converging solution, a 3σ clipping was performed on both RV curves to eliminate observations having outlier RVs. The final rms (root mean square) residuals in the light curves are 0.013 mag in B, 0.013 mag in V, and 0.046 mag in the DIRECT V light curve. The residuals of the RVs are 5.2 and 4.6 km s^{-1} for the primary and secondary components, respectively.

The light and RV curves, with their respective fits superimposed are shown in Fig. 4.2. It is worth to remark that the O'Connell effect observed in the light curves identify this EB as semi-detached (with the secondary filling the Roche lobe, see Sect. 2.4.1). The resulting best-fitting elements are listed in Table 4.3. Two massive stars are observed, with masses (and radii) of $\mathcal{M}_P = 23.1 \pm 1.3$ $M_\odot$ ($R_P = 13.1 \pm 0.3$ $R_\odot$) and $\mathcal{M}_S = 15.0 \pm 1.1$ $M_\odot$ ($R_S = 11.3 \pm 0.3$ $R_\odot$), for the primary and the secondary components, respectively.

One possible concern with light curves measured using DIA photometry is the

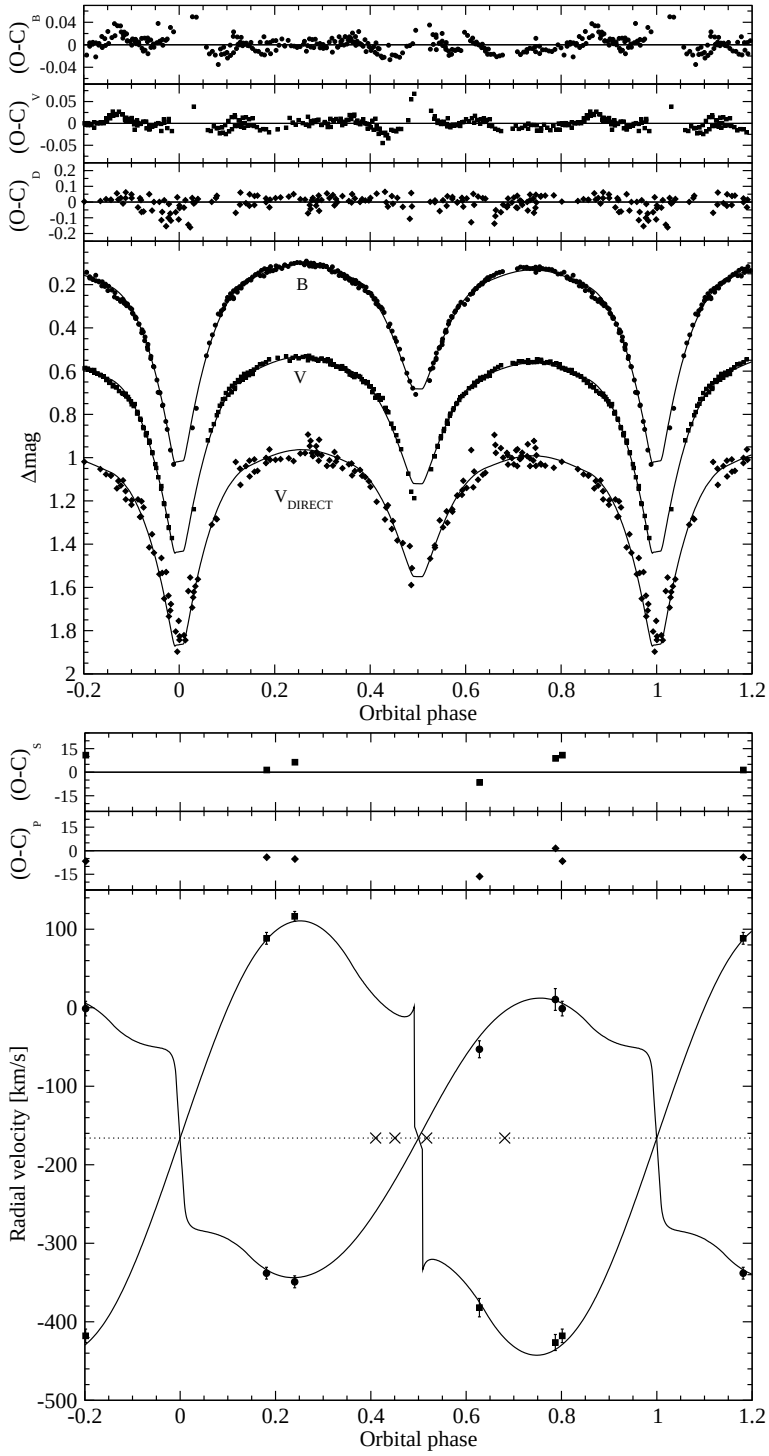

Figure 4.2. Observations for M31V J00443799+4129236 (SB2A) and corresponding W&D fits. **Top:** Light curve fits and corresponding residuals. **Bottom:** RV curve fits with RVs for the primary (circles) and secondary (squares) components with corresponding residuals. The phases of rejected RV observations are also indicated (crosses).

effect of an incorrect reference flux, which may cause a bias in the scale of the light curves (Michalska & Pigulski, 2005). Careful tests were carried out to ensure that this was not the case (Sect. 2.2.2). The excellent agreement between the fits to our DIA photometry and the fits to the DIRECT PSF photometry suggests that the flux zero-point is correct. In addition, we ran light-curve fits with a variable third-light contribution (l_3). A nonzero value (either positive or negative) of l_3 might indicate problems with the flux scale, but this did not occur, and the solutions converged to $l_3 \sim 0$. Such result has another interesting consequence of ruling out possible blends with unresolved companions. The absence of positive l_3 is not unexpected, since the light curves have the maximum possible depth ($i \sim 90$ deg) and preclude the existence of any additional light.

4.1.1.3 Temperature and distance determination

The last required ingredient to obtain a direct distance determination to M 31 is the temperature and absorption determination of SB2A. The photometric data available (i.e., B and V) are, by themselves, insufficient to determine the temperatures and reddening of the system. Therefore, two different approaches were attempted: modeling the spectra used for RV determinations and modeling the spectrophotometry.

Modeling of the optical spectra

The currently available stellar atmosphere models and line lists provide highly reliable synthetic spectra. These spectra, when compared with those observed, can provide accurate values of temperature, surface gravity, metallicity, etc. Therefore, we modeled the optical spectra with available stellar atmosphere models in order to derive the stellar temperature of the components in SB2A.

In EB systems, the spectra of both components are merged into a single spectrum and, therefore, the individual spectrum of each component has to be disentangled to accurately model the optical spectra. To perform this, we ran the KOREL program (Hadrava, 1995) by fixing all the parameters to the orbital solutions described in Sect 4.1.1.2. The resulting spectra are shown in Fig. 4.3.

Using a code developed by Edward L. Fitzpatrick at the Villanova University (Philadelphia), we then modeled the disentangled spectra using TLUSTY atmosphere models. Fits were constrained by the temperature ratio, surface gravities, and brightness ratio determined from the binary analysis. We solved for the constrained temperatures, a single metallicity for both components and individual values of $v_{\rm rot} \sin i$. The obtained values are listed in Table 4.4, and the best-fitting models are shown in Fig. 4.3, below each of the stellar spectra. Table 4.4 also lists values of M_V and $(B-V)_0$ for the components of the system. These values were

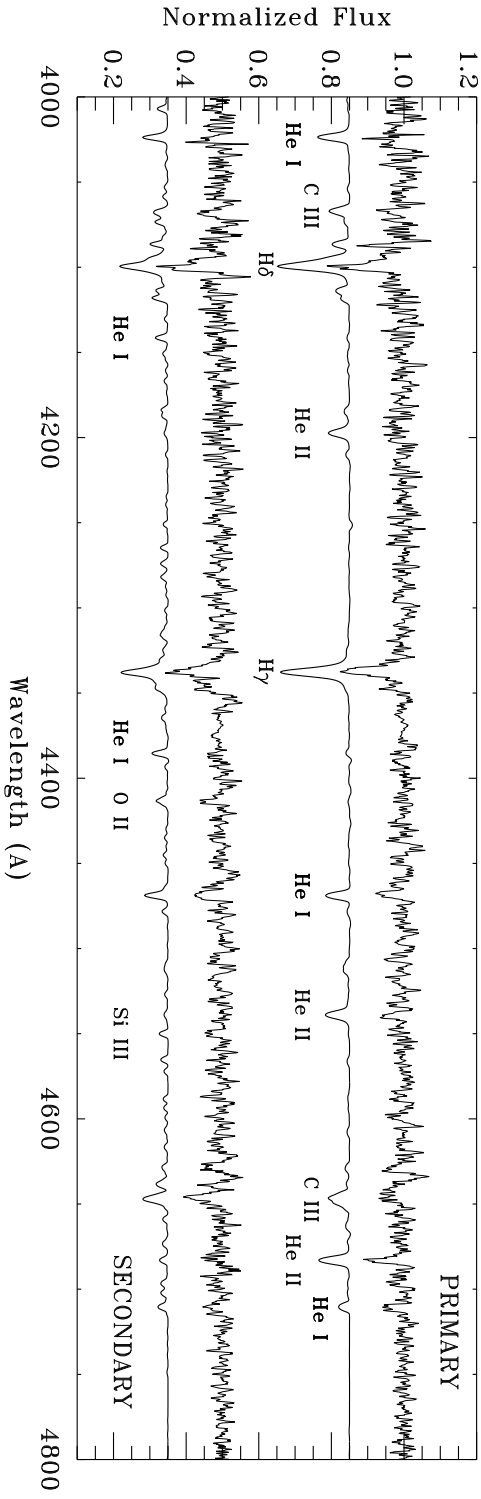

Figure 4.3. Comparison of the individual disentangled spectra for the EB M31V J00443799+4129236 (SB2A) with TLUSTY synthetic spectra. Some of the most intense spectral lines are labeled.

Table 4.4. Fundamental properties for M31V J00443799+4129236 (SB2A) and resulting distance determination, derived from the modeling of the optical spectra using TLUSTY atmosphere models and the values in Table 4.3.

System properties				
Metallicity ($[m/H]$)		-0.01±0.06		
Absolute V magnitude (M_V)		-5.77±0.06		mag
Color excess ($E(B-V)$)		0.19±0.03		mag
Line-of-sight absorption (A_V)		0.60±0.10		mag
Distance modulus ($(m-M)_0$)		24.44±0.12		mag
Component properties	Primary		Secondary	
Effective temperature ($T_{\rm eff}$)	33 900±500	K	27 700±500	K
Rotational velocity ($v_{\rm rot}\sin i$)	230±10	km s^{-1}	145±8	km s^{-1}
Absolute V magnitude (M_V)	-5.29±0.07	mag	-4.66±0.07	mag
Intrinsic color ($(B-V)_0$)	-0.28±0.01	mag	-0.27±0.01	mag

computed by scaling the surface fluxes predicted by the TLUSTY models with the observed radii of the stars and performing synthetic photometry on the resultant energy distributions. The photometry was calibrated as described in Fitzpatrick & Massa (2005).

The 1σ uncertainties in the results of the spectral analysis were determined by a Monte Carlo technique. First, we created simulations of the spectra by combining our pair of best-fit models with 50 different random noise realizations, corresponding to S/N=40. For each simulated spectrum pair, we generated a simulated set of binary parameters (e.g., $T_{{\rm eff},S}/T_{{\rm eff},P}$) by combining the best-fit values with Gaussian noise, based on the 1σ uncertainties for each value. Finally, we fitted each pair of simulated spectra as described above, and adopted the standard deviations of the parameters among the 50 simulations as our uncertainties.

Once the fundamental properties are found, the calculation of the distance is straightforward, because the spectral analysis yields values for the absolute magnitudes of the components and also the combined M_V of the system (see Table 4.4). The distance modulus follows directly from the equation:

$$(m-M)_0 = V - M_V - A_V \tag{4.1}$$

To estimate the interstellar extinction (A_V), we compared the observed color ($B-V$) for the system with the intrinsic color ($(B-V)_0$) resulting from the spectral fit. Then we computed the total extinction from Eq. 1.10, with a total-to-selective extinction ratio of $\mathcal{R}_V = 3.1 \pm 0.3$ (Fitzpatrick & Massa, 2007). The overall procedure avoids the use of bolometric corrections and is self-consistent, as it employs the best-fitting model atmospheres (i.e., with the appropriate surface gravity and metallicity) to calculate the absolute M_V magnitudes and $(B-V)_0$ colors.

One basic point is a reliable estimation of the error budget. With the uncer-

tainty in M_V accounting for the full correlations of the intervening parameters, the rest of the quantities in the distance modulus equation are essentially uncorrelated. Thus, the contributions from the observed V magnitude (0.02 mag), M_V (0.06 mag), and A_V (0.10 mag) can be combined quadratically. From the parameters in Table 4.4 our calculation of the distance modulus to SB2A results in a value of $(m - M)_0 = 24.44 \pm 0.12$ mag or, equivalently, $d = 772 \pm 44$ kpc. This distance also corresponds to the center of M 31 itself, because the correction due to the location of the EB is negligible ($\sim 0.3\%$).

Spectrophotometry

We used the HST spectrophotometric measurements (reduced in Sect. 3.2) as an alternative approach to derive the temperature and absorption of the observed target. Following Fitzpatrick et al. (2003), the flux at a certain wavelength ($f_\lambda^\oplus$) of the observed EB is given by Eq. (1.13). The surface fluxes were obtained from TLUSTY atmosphere models and the normalized extinction curve was modeled as in Fitzpatrick & Massa (2007).

Some tests were performed in order to assess the capability of the obtained data to provide accurate temperature and extinction parameters. The results revealed that errors in the data were too large to obtain an accurate determination of the fitted parameters. In addition, the contamination of nearby stars in some of the observed spectra prevented from an accurate spectrophotometric modeling. Therefore, we decided to use the spectrophotometric data to check the accuracy of the temperature determinations resulting from the spectral fitting (described above) and, at the same time, to validate the procedure used.

All the parameters required to model the spectral energy distribution were fixed to the values resulting from the spectroscopic and photometric analysis. In order to introduce the effect of absorption, the mean galactic interstellar extinction curve was used (Fitzpatrick & Massa, 2007). As it is shown in Fig. 4.4, the model is compatible with the observations (that have errors in the range of 10–20%), but some systematics (of the order of 1σ) can be seen in the ultraviolet region (125–160 nm and around 200 nm) and in the infrared (600-1000 nm). On the one hand, some tests performed at the Villanova University with spectrophotometric standards reveal that the HRC/G800L calibration coefficients tend to provide standard fluxes that are too low, introducing the systematics in the infrared. When using a new set of coefficients (provided by a new recalibration with spectrophotometric standards) the observed systematics are corrected (as shown in the bottom panel of Fig. 4.4). On the other hand, the mean galactic extinction curve is affected by large uncertainties ($\sim$10%) in the ultraviolet part of the spectrum. Large differences in the extinction curve, depending on the line-of-sight, are the underlying reason for these uncertainties. Correspondingly, the modeled spectral energy distribution is affected by the same uncertainties, resulting in a systematic offset be-

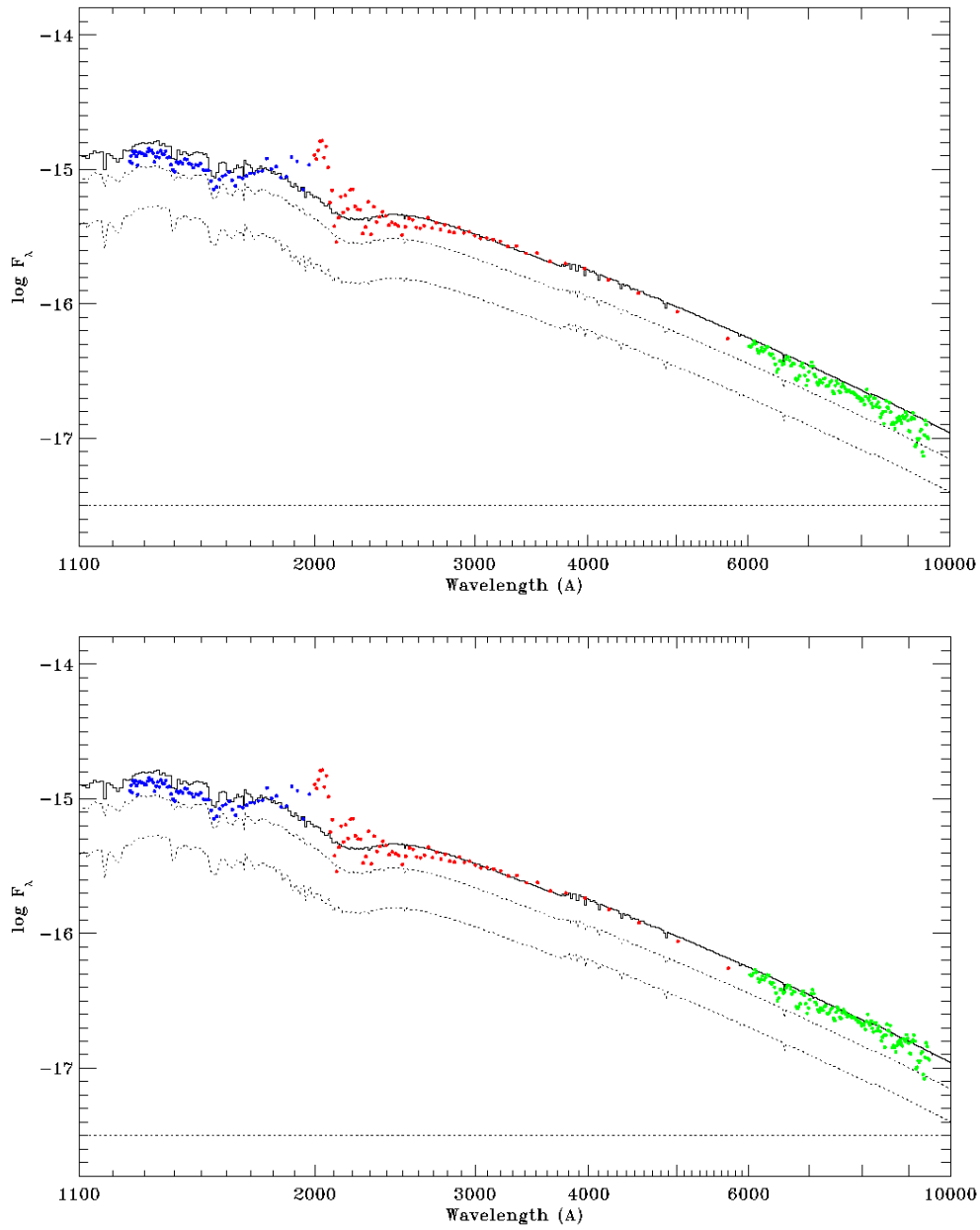

Figure 4.4. Spectral energy distribution for M31V J00443799+4129236 (SB2A). Dots correspond to the observations with the three ACS grisms used. Dotted lines represent the spectral energy distribution of each component, modeled according to the solutions derived from the spectroscopic and photometric analysis. The solid line is the combination of both components. **Top:** Calibrated values resulting from the implementation of the coefficients in the standard ACS reduction pipeline. **Bottom:** Calibrated values resulting from the implementation of a new set of coefficients provided by a new recalibration with spectrophotometric standards.

tween 110 and 160 nm. Finally, as shown in Sect 3.2.2.2, the large offset around 200 nm cannot be considered significant because of the large errors introduced by a contaminating star in this region. Therefore, although some well understood systematics ($\sim 1\sigma$) can be observed in the modeled spectrophotometry, the obtained spectrophotometry can be considered to be compatible with the parameters derived from the spectroscopic analysis and provides an independent confirmation (within the relatively large uncertainties) of the fundamental properties of SB2A (Table 4.3 and Table 4.4).

4.1.1.4 Comparison with stellar evolutionary models

The final step towards the characterization of SB2A is the comparison of the derived physical properties with stellar evolutionary models. The comparison has been mainly performed with the Geneva models of Lejeune & Schaerer (2001), considering solar metallicity (according to the metallicity in Table 4.4). Other models have been considered (Claret, 2004) without any major variations on the derived conclusions. It is important to emphasize that the evolutionary tracks are build for isolated stars. In close binary systems, the evolution of both stars can be largely modified, with respect to their isolated evolutionary tracks, when one of the components fills the Roche lobe and mass transfer takes place (see, e.g., Vanbeveren, 1993).

In order to take into account the effects of mass loss (due to stellar wind), the mass of each component at the Zero-Age Main Sequence (ZAMS) was determined by fitting different evolutionary tracks in the mass–radius diagram (Fig. 4.5, top). The fitted tracks reveal that a 23.9 $M_{\odot}$ isolated star (i.e., with no mass transfer) would have lost around 0.8 $M_{\odot}$ (comparable to the obtained error in mass) at the current evolutionary stage. Therefore, mass loss is an important effect that has to be considered when analyzing the evolutionary tracks of massive stars.

Once the evolutionary tracks are adopted, the Hertzsprung-Russell (hereafter H-R) diagram can be studied (Fig. 4.5, bottom). The resulting locations of the observed components reveal that both stars are overluminous for their masses. In addition, the secondary component seems to be more evolved than the primary. These results are in agreement with results obtained in other post-mass transfer semi-detached systems (e.g., Fitzpatrick et al., 2003). In these systems, the originally more massive component (currently the secondary) evolves beyond the Roche lobe and some fraction of its mass is transferred to the companion star. The mass transfer continues nowadays, when the mass-accreting component has become the currently most massive component.

The proposed scenario is in agreement with the fact that the primary component rotates faster than synchronization (see Table 4.3 and Table 4.4), since the accreting mass also implies a transfer of angular momentum from the secondary (which is tidally locked, as can be assumed from the rotational velocities and 2σ

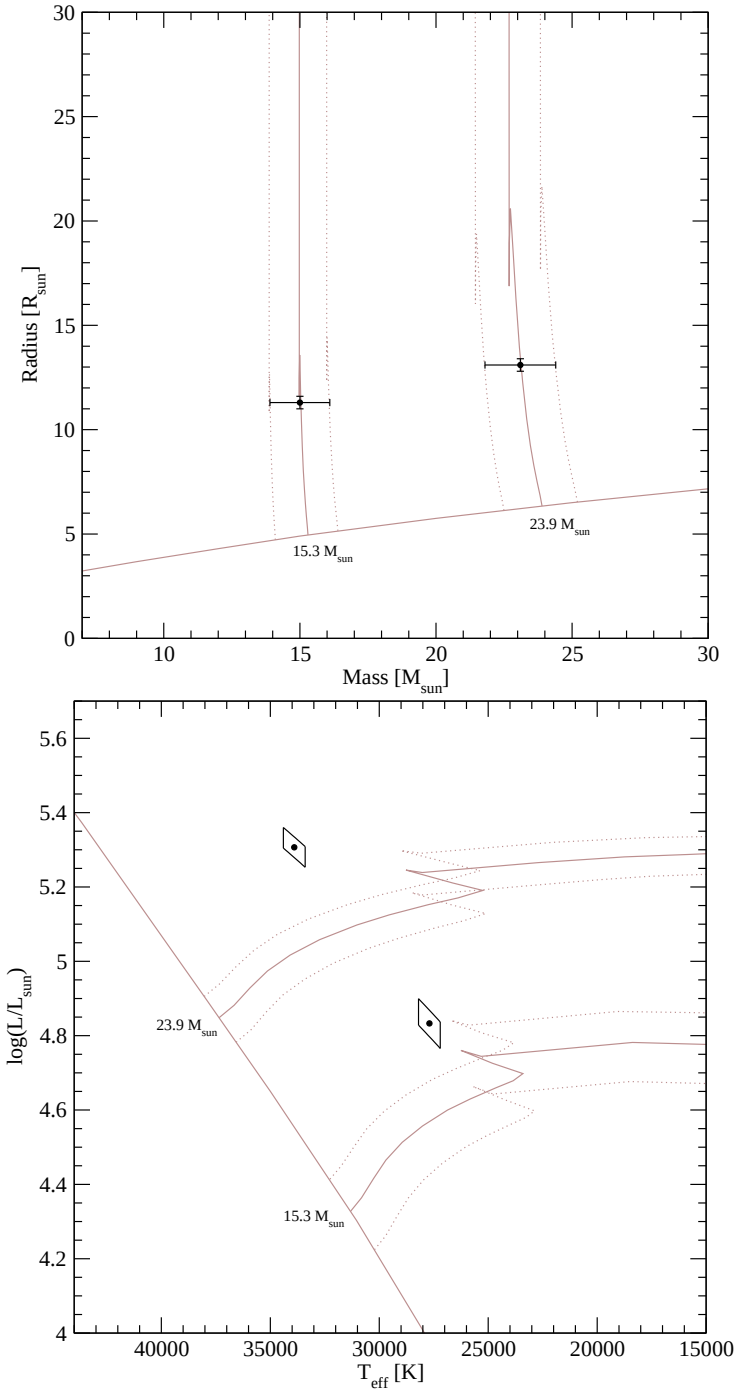

Figure 4.5. Comparison of stellar evolutionary models with derived physical properties of M31V J00443799+4129236 (SB2A). Gray solid lines correspond to the ZAMS and the evolutionary tracks (initial masses are labeled). Gray dotted lines denote the uncertainties in the derived masses. **Top:** Mass–radius diagram. **Bottom:** H-R diagram. The skewed rectangular boxes correspond to 1σ error loci.

error bars) to the primary. In other observed systems, the primary component is usually in better agreement with the corresponding evolutionary track. However, the mass transfer in SB2A seems to be really intense, with a bright hot spot that is synchronized with the rotational period of the system (as observed in the light curve). Since the primary component rotates $\sim 25\%$ faster than synchronization, the material from the secondary component will impact the surface of the primary at different points. Therefore, the impacting material, combined with the proximity of both components, could increase the overall temperature (and luminosity) of the primary component.

4.1.2 M31V J00443610+4129194 (SB2B)

4.1.2.1 Radial velocities

The determination of RVs was performed, as in the case of SB2A (Sect. 4.1.1.1), with TODCOR and the ATLAS9 and TLUSTY synthetic models. In this case, the best pair of synthetic spectra was determined with a different iterative approach. As a first step, the preliminary W&D fit (Sect. 2.4.1) was used to define an initial list with pairs of models having a temperature ratio, gravity ratio and rotational velocities compatible with the W&D parameters. All the model pairs in the initial list were then used to determine RVs and a simple RV curve model was fitted to the obtained values. The free parameters in the fit were the semi-major axis (a), the systemic velocity (γ) and the mass ratio (q), whereas the period and reference time was fixed from the W&D solution. From all the derived solutions, the models having a lower dispersion around the fitted RV curve were selected and all the neighboring models in the space of parameters were also attempted. The process was repeated until the local minimum was found, (i.e., none of the neighboring models has a scatter lower than the selected pair of models).

Since the resulting RVs depend, to some extent, on the W&D fit, the obtained values were used to find a new solution with the W&D (Sect. 4.1.2.2). The resulting W&D solution was then used to determine new RVs. The process was repeated until the pair of synthetic models providing the best fit was the same in two iterations. The final solution shown in Table 4.5 contains all the RVs (corrected to the heliocentric reference frame) that remained after the W&D fit (with 3σ clipping). Rejected observations shown in Fig. 4.6 were obtained during eclipses (one of them correspond to the spectrum of February 2005 with a shorter exposure time).

The rejected observation close to phase 0.9 cannot be explained neither by the proximity to the nodes (since other observations are obtained at larger phases) nor by a lower S/N of the observed spectrum. Therefore, additional tests were performed. They revealed that the rejected observation could be recovered with different pairs of templates at the cost of losing other spectra close to the nodes and a larger dispersion of the fit. The obtained solutions had systemic velocities

Table 4.5. Radial velocity determinations for the EB M31V J00443610+4129194 (SB2B).

Time [HJD]	Phase	Primary [km s^{-1}]	Secondary [km s^{-1}]
2 453 316.931	0.2719	-370.1±8.2	143.5±30.3
2 453 321.820	0.6586	14.3±13.9	-414.1±25.5
2 453 321.872	0.6836	57.3±13.5	-448.2±24.8
2 453 319.879	0.7111	30.6±9.9	-455.5±17.4
2 453 260.910	0.9265	-69.7±18.1	-309.2±19.4
2 453 295.776	0.9456	-58.1±24.2	-271.7±22.9

and semi-amplitudes in perfect agreement with the solution presented here. In addition, solutions with different W&D fits converged to the same pair of templates. The final reason for the incorrect RV determinations was found to be a casual correlation of the spectrum of the secondary with noise, which introduces a false correlation peak and biased RVs for this particular observation.

4.1.2.2 Mass and radius determination

The mass and radius determination was performed following the fitting procedure described for SB2A in Sect. 4.1.1.2. A configuration where the primary (instead of the secondary) fills the Roche lobe was used in this case. Both semi-detached configurations (with either the primary or the secondary filling the Roche lobe) provide fits with the same residuals. Therefore, the final configuration was adopted after the temperature determination analysis (Sect. 4.1.2.3). The spectra resulting from the disentangling indicate that the secondary is much fainter than the primary, whereas supposing that the secondary fills the Roche lobe provides a flux ratio of $F_{V,S}/F_{V,P} = 0.85$.

In order to ensure the viability of the adopted scenario, and to rule out any other possible configurations, additional fits supposing a detached configuration were performed. The resulting parameters revealed that, depending on the initial value of the surface potential of the secondary component, either the primary or the secondary tended to fill their respective Roche lobes.

With the adopted configuration, the final rms residuals are 0.014 mag in *B*, 0.015 mag in *V*, and 0.047 mag in the DIRECT *V* light curve. The residuals of the RVs are 13 and 6 km s^{-1} for the primary and secondary components, respectively. The light and RV curves, with their respective fits superimposed, are shown in Fig. 4.6. The resulting best-fitting elements listed in Table 4.6 reveal two components with masses very similar to those of SB2A, but smaller radii. The resulting masses (radii) are $\mathcal{M}_P = 21.7 \pm 1.7$ M$_\odot$ ($R_P = 9.2 \pm 0.2$ R$_\odot$) and $\mathcal{M}_S = 15.4 \pm 1.2$ M$_\odot$ ($R_S = 5.6 \pm 0.4$ R$_\odot$).

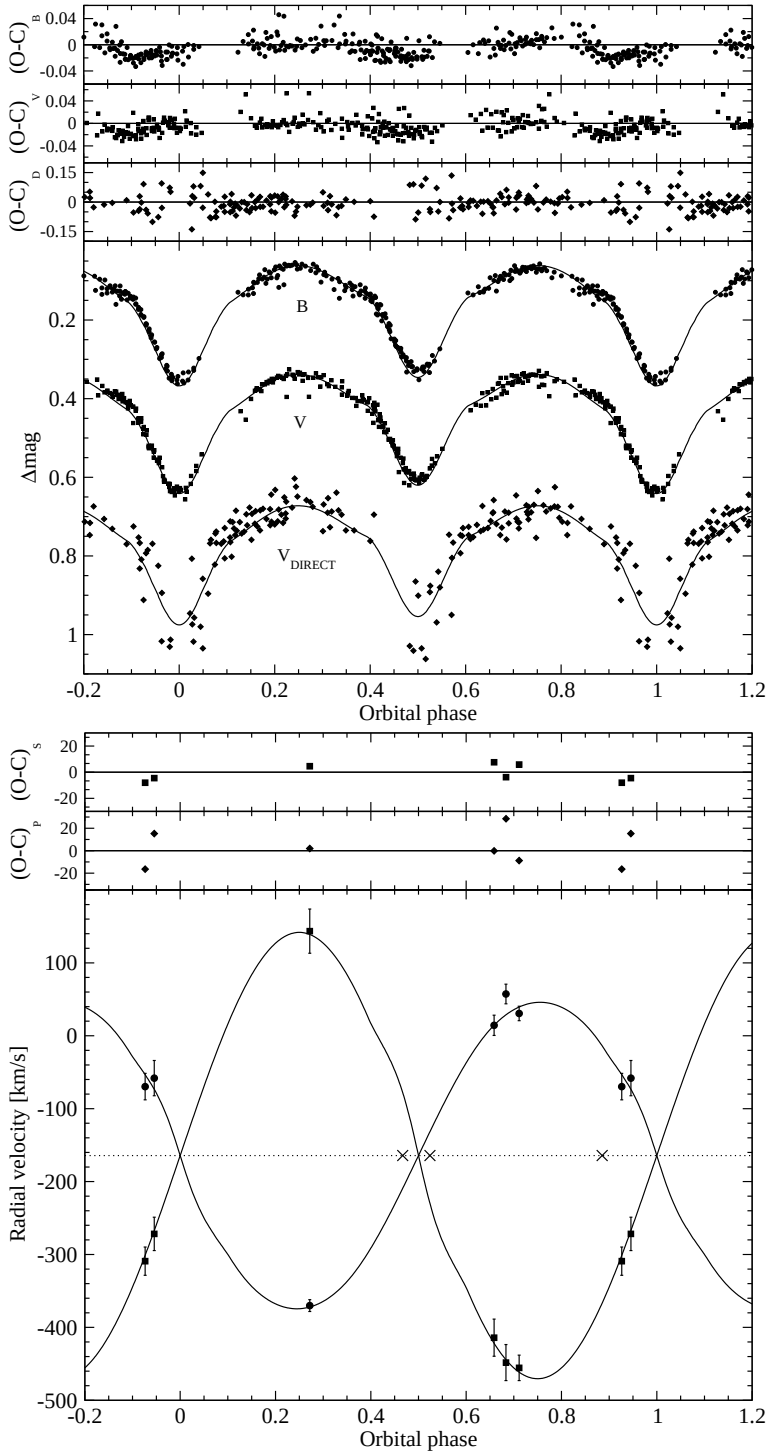

Figure 4.6. Observations for M31V J00443610+4129194 (SB2B) and corresponding W&D fits. **Top:** Light curve fits and corresponding residuals. **Bottom:** RV curve fits with RVs for the primary (circles) and secondary (squares) components with corresponding residuals. The phases of rejected RV observations are also indicated (crosses).

Table 4.6. Fundamental properties of M31V J00443610+4129194 (SB2B) derived from the analysis with W&D.

System properties				
B magnitude at maximum light ($B_{\max}$)[a]	19.832±0.013			mag
V magnitude at maximum light ($V_{\max}$)[a]	19.948±0.015			mag
Period (P)	2.048644±0.000007			days
Time of minimum ($t_{\min}$)	2 452 908.694±0.004			HJD
Inclination (i)	69.9±1.6			deg
Systemic velocity (γ)	-164±5			km s^{-1}
Semi-major axis (a)	22.6±0.5			$R_\odot$
Mass ratio ($q = \mathcal{M}_S/\mathcal{M}_P$)	0.71±0.04			
Temperature ratio ($T_{\mathrm{eff},S}/T_{\mathrm{eff},P}$)	0.897±0.019			
Flux ratio in B ($F_{B,S}/F_{B,P}$)[a]	0.33±0.03			
Flux ratio in V ($F_{V,S}/F_{V,P}$)[a]	0.33±0.03			
Flux ratio in V_{DIRECT} ($F_{D,S}/F_{D,P}$)[a]	0.33±0.05			
Component properties	Primary		Secondary	
Radius (R)	9.2±0.2	$R_\odot$	5.6±0.4	$R_\odot$
Mass ($\mathcal{M}$)	21.7±1.7	$M_\odot$	15.4±1.2	$M_\odot$
Surface gravity ($\log g$ in cgs)	3.85±0.02		4.12±0.05	
Radial velocity semi-amplitude (K)[b]	210±9	km s^{-1}	306±11	km s^{-1}
Synchronized rotational velocity ($v_{\mathrm{sync}} \sin i$)	213±6	km s^{-1}	131±8	km s^{-1}

[a] Out of eclipse average: $\Delta\phi = [0.20 - 0.30, 0.70 - 0.80]$

[b] Including non-Keplerian corrections

Following the reasoning in Sect. 4.1.1.2, several light-curve fits were performed with a variable third-light contribution (l_3). Again, the excellent agreement between the DIRECT light curve to our photometry and the convergence of the fits to $l_3 \sim 0$, ensures that the flux zero-point is correct and rules out any possible blends with unresolved companions.

4.1.2.3 Temperature and distance determination

The only data available for SB2B to perform a temperature determination are the GMOS spectra. Therefore, as in Sect. 4.1.1.3, we determined the temperature of the components by modeling the disentangled spectra from the KOREL program. The parameters obtained in Sect. 4.1.2.2 were used for performing the disentangling. It is important to emphasize that the RV curve depends only slightly on the configuration adopted. Therefore, the disentangled spectra (Fig. 4.7) can be considered the same for the case when the primary or the secondary fills the Roche lobe.

The disentangling provided an spectrum for the secondary component mainly dominated by noise. This is not surprising considering the derived flux ratio ($F_{V,S}/F_{V,P} = 0.33$) and the S/N of the observed spectra, resulting in a spectrum

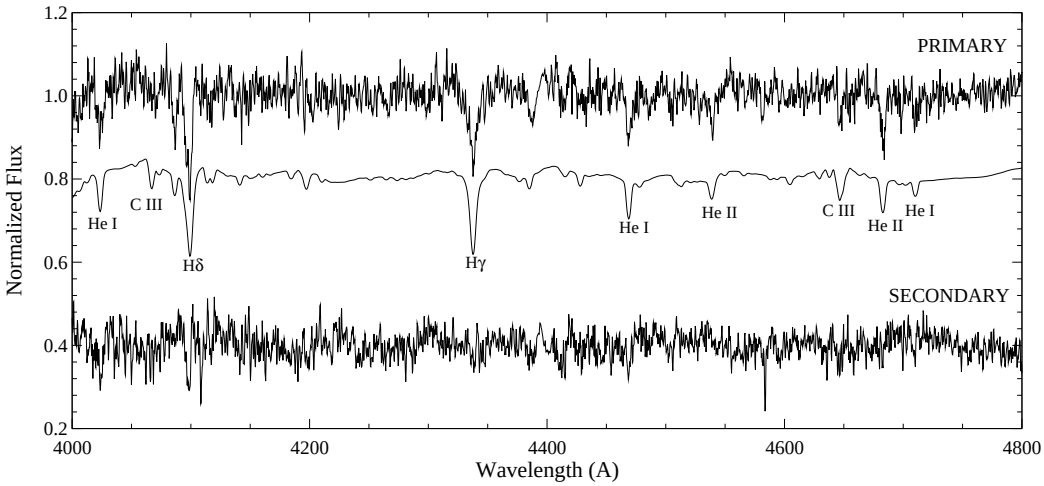

Figure 4.7. Comparison of the individual disentangled spectrum for the primary component of M31V J00443610+4129194 (SB2B, above) with the TLUSTY synthetic spectrum (middle). The bottom spectrum shows the disentangled spectrum of the secondary component.

for the secondary with a S/N∼10. In a system where both components are equally bright, each component has a similar contribution to the combined spectrum, resulting in disentangled spectra that have a similar S/N. Therefore, the disentangled spectra indicate that the secondary component is clearly fainter than the primary component. As previously mentioned (Sect. 4.1.2.2), supposing that the secondary fills the Roche lobe results in a flux ratio $F_{V,S}/F_{V,P} = 0.85$, which is clearly in contradiction with the results provided by the disentangling. Then, the scenario where the secondary fills the Roche lobe can be excluded, since a flux ratio of $F_{V,S}/F_{V,P} = 0.85$ should result in a spectrum with a S/N∼25 for the secondary, similar to the best quality observed spectra.

Considering the low S/N of the secondary, the fitting procedure was restricted to the primary component. The temperature ($T_{\rm eff}$), surface gravity ($\log g$) and rotational velocity ($v_{\rm rot} \sin i$) were fitted considering TLUSTY templates with solar metallicity. The resulting values are listed in Table 4.7 together with the values of absolute luminosity (M_V) and intrinsic color ($(B-V)_0$). These values were computed by scaling the absolute magnitude in the models of Lejeune & Schaerer (2001) (for a given temperature and gravity) with the observed radii of the stars. When needed, the values resulting from the W&D fit were used (e.g., to determine the temperature of the secondary). This procedure is equivalent to the one used in Sect. 4.1.1.3, where instead of performing the synthetic photometry to obtain the surface fluxes (as in the case of SB2A), they were obtained from the models.

Finally, once the absolute magnitudes of the components are determined, the determination of the distance is straightforward (Sect. 4.1.1.3). The resulting distance modulus to SB2B is $(m-M)_0 = 24.30 \pm 0.11$ mag or, equivalently,

Table 4.7. Fundamental properties of M31V J00443610+4129194 (SB2B) and resulting distance determination, derived from the modeling of the optical spectrum of the primary component, using TLUSTY atmosphere models and the values in Table 4.6.

System properties				
Absolute V magnitude (M_V)		-4.90±0.08		mag
Color excess ($E(B-V)$)		0.18±0.02		mag
Line-of-sight absorption (A_V)		0.55±0.08		mag
Distance modulus ($(m-M)_0$)		24.30±0.11		mag
Component properties	Primary		Secondary	
Effective temperature ($T_{\rm eff}$)	33 600±600	K	30 100±900	K
Surface gravity ($\log g$ in cgs)	3.86±0.12		—	
Rotational velocity ($v_{\rm rot} \sin i$)	189±12	km s^{-1}	—	
Absolute V magnitude (M_V)	-4.59±0.07	mag	-3.38±0.12	mag
Intrinsic color ($(B-V)_0$)	-0.295±0.002	mag	-0.286±0.004	mag

$d = 724 \pm 37$ kpc.

4.1.2.4 Comparison with stellar evolutionary models

In order to compare the derived properties of SB2B with stellar evolutionary models, the procedure described in Sect. 4.1.1.4 was followed. The location of the studied components on the H-R diagram (Fig. 4.8) reveals that both components agree with their predicted evolutionary tracks.

The derived properties seem characteristic of a detached system. However, as explained in Sect. 4.1.2.2, the W&D solutions supposing a detached configuration converge to solutions where either the primary or the secondary fill their respective Roche lobes. In addition, the disentangled spectra seem to favor the case where the primary is filling the Roche lobe, since it is much brighter than the secondary. All these observations can be explained supposing that SB2B is a pre-mass transfer EB system, where the primary component is *almost* filling its Roche lobe.

In a pre-mass transfer EB, both components are detached and basically follow the evolution of single stars. This explains why the observed properties agree with the evolutionary tracks, since each component has evolved without any major interaction with the other component. This could also explain why the most massive component can be assumed to be filling the Roche lobe. What is generally observed in semi-detached EBs is the Algol paradox, where the donor is the less massive component (as in the case of SB2A, described in Sect. 4.1.1.4). The reason of this phenomenon (Paczyński, 1971) is that, when the donor is more massive than the companion, the mass transfer is very rapid, taking place on a thermal time scale ($\sim 10^5$ yr). On the contrary, when the donor is less massive

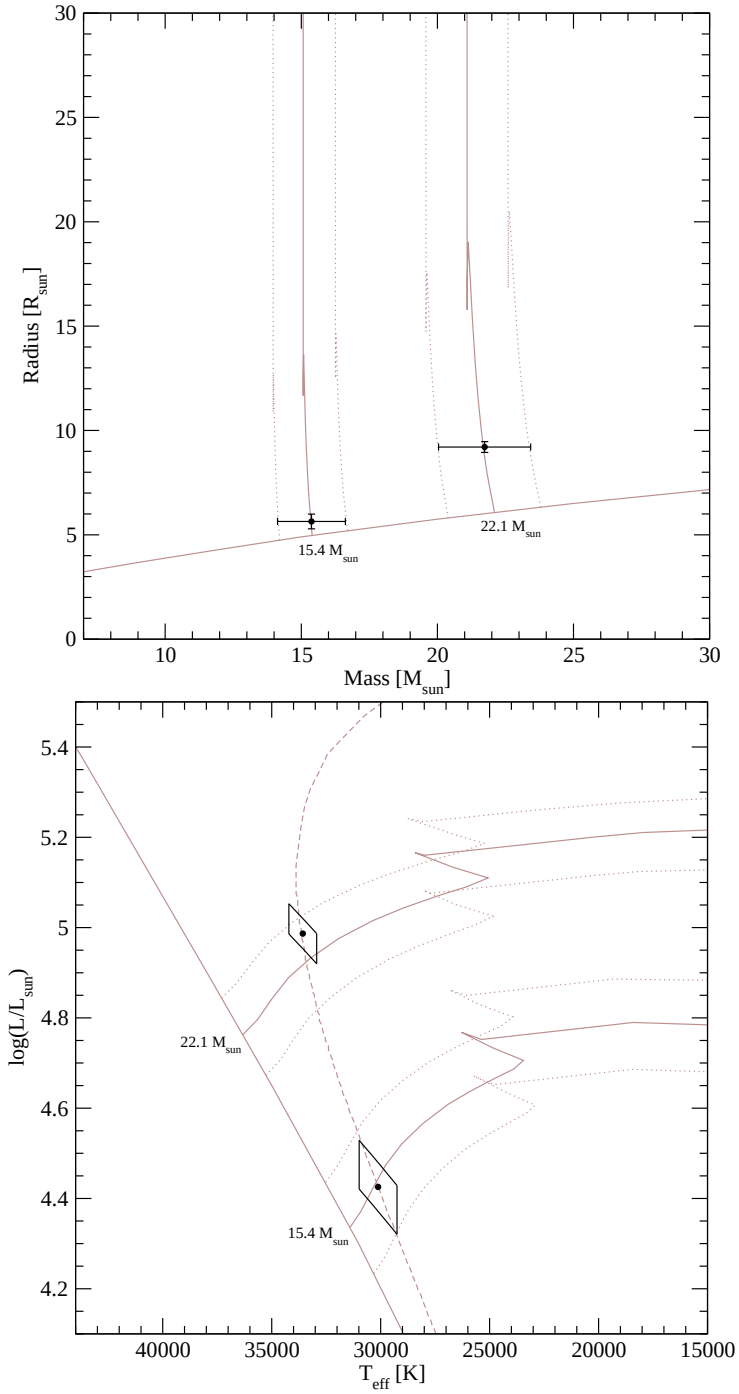

Figure 4.8. Comparison of stellar evolutionary models with derived physical properties of M31V J00443610+4129194 (SB2B). Gray solid lines correspond to the ZAMS and the evolutionary tracks (initial masses are labeled). The best fitting isochrone of 4.2 Myr is also shown (gray dashed line). Gray dotted lines denote the uncertainties in the derived masses. **Top:** Mass–radius diagram. **Bottom:** H-R diagram. The skewed rectangular boxes correspond to 1σ error loci.

than the companion, the mass transfer can last as long as the main-sequence lifetime of the donor. The lack of any signature of intense mass transfer (such an O'Connell effect in the light curves), combined with the short timescale of the process, makes that a situation where the most massive component is filling the Roche lobe is unlikely. In addition, the time spent in a situation where a massive star (like the ones observed) can be almost filling the Roche lobe is somewhat longer than the thermal timescale ($\sim$ 0.5 Myr), making the situation more likely to be observed.

The close agreement of the observations with the theoretical models, apart from clarifying the evolutionary stage of SB2B, also allowed the fitting of an isochrone, resulting in an estimated coeval age of 4.2 ± 0.4 Myr.

4.1.3 M31V J00444528+4128000 (SB1)

4.1.3.1 Radial velocities

A close look at the acquired spectra of SB1 (the brightest EB in the variable star catalog) revealed no signs of features belonging to the secondary component. In addition, several attempts were performed to determine RVs (with TODCOR) assuming that SB1 has double lines, with no physically valid results. Therefore, SB1 was assumed to be a single-line EB.

The brightness of SB1 has made that the GMOS spectra have a relatively high S/N, allowing the use of algorithms to determine the RVs that are independent of synthetic templates. Therefore, a specific algorithm (called TIRAVEL, Zucker & Mazeh, 2006) was used to determine the RVs. The most important advantage of using TIRAVEL (with respect to cross-correlation algorithms) is that no assumption has to be made, either on the EB model nor on the atmosphere of the star. Radial velocities are determined from the relative displacement of the lines among the obtained spectra and, hence, no information on the absolute RVs is obtained. However, TIRAVEL is capable to provide a merged spectrum (with higher S/N) from all the observed spectra. The merged spectrum is analyzed in the temperature determination process (Sect. 4.1.3.2) and, as a by-product, its absolute RV is obtained. Since the merged spectrum has a null relative RV, the derived RV corresponds to the difference between the absolute RVs and the relative RVs provided by TIRAVEL.

It is worth mentioning that TIRAVEL can only use 2048 points of each spectrum. Therefore, the observed GMOS spectra were split into two parts (361.1–456.8 nm and 410.9–506.5 nm) and independent radial velocities were obtained (Table 4.8). Both RVs were averaged to obtain the RVs for the primary component (corrected to the heliocentric reference frame) shown in Table 4.8.

In order to estimate the uncertainties of the RVs provided by TIRAVEL, a

Table 4.8. Relative radial velocity determinations for M31V J00444528+4128000 (SB1). For each spectrum, two RVs were derived: one for the part with shorter wavelengths (361.1–456.8 nm, blue part) and one for the part with longer wavelength (410.9–506.5 nm, red part). The RVs of the primary component are the mean of both results.

Time [HJD]	Phase	Blue RVs km s^{-1}	Red RVs km s^{-1}	Primary [km s^{-1}]
2 453 316.931	0.1461	-70.1	-63.6	-66.9±4.4
2 453 260.910	0.2931	-72.3	-63.7	-68.0±4.3
2 453 295.776	0.3135	-84.5	-84.6	-84.6±4.4
2 453 319.879	0.4015	-44.6	-42.5	-43.6±4.4
2 453 262.874	0.4633	-5.3	-11.6	-8.4±4.5
2 453 413.734	0.5319	25.6	33.6	29.6±3.9
2 453 264.066	0.5665	79.4	62.4	70.9±4.5
2 453 321.820	0.5697	53.4	51.9	52.7±4.3
2 453 321.872	0.5741	57.7	57.6	57.6±4.5

program performing simple cross-correlation was applied to each one of the nine observed spectra. The cross-correlation technique requires a template. In this case, a TLUSTY spectrum with properties similar to those derived after the temperature determination (Sect. 4.1.3.2) was used as template. The uncertainties derived from the correlation were considered to be the uncertainties in the RVs of the primary component. As shown in Table 4.8, the derived uncertainties make the two independent RVs provided by TIRAVEL fully compatible. Finally, the RVs resulting from the correlation program also enabled an independent check on the RV determinations provided by TIRAVEL, confirming the obtained values within the error bars.

4.1.3.2 Temperature determination

As previously mentioned (Sect. 4.1.3.1), we used the combined spectrum provided by TIRAVEL to determine the temperature of the primary component. The combined spectrum was modeled using TLUSTY model atmospheres (Fig. 4.9). The good quality of the spectrum (S/N~70) allowed a complete characterization of the fundamental properties of the primary component (Table 4.9), including metallicity ($[m/H]$), microturbulent velocity ($v_{\rm micro}$) and rotational velocity ($v_{\rm rot} \sin i$). These quantities have a small effect on the final temperature and absolute magnitude of the modeled star, but provide additional information on the fundamental properties of the system. Of particular interest is the low surface gravity derived ($\log g = 2.57 \pm 0.03$ dex), indicating that the primary component of SB1 is evolved. This was expected, since the comparison of the spectrum with that of other blue supergiants (e.g, HD 38771, HD 152234) already classified this star as evolved.

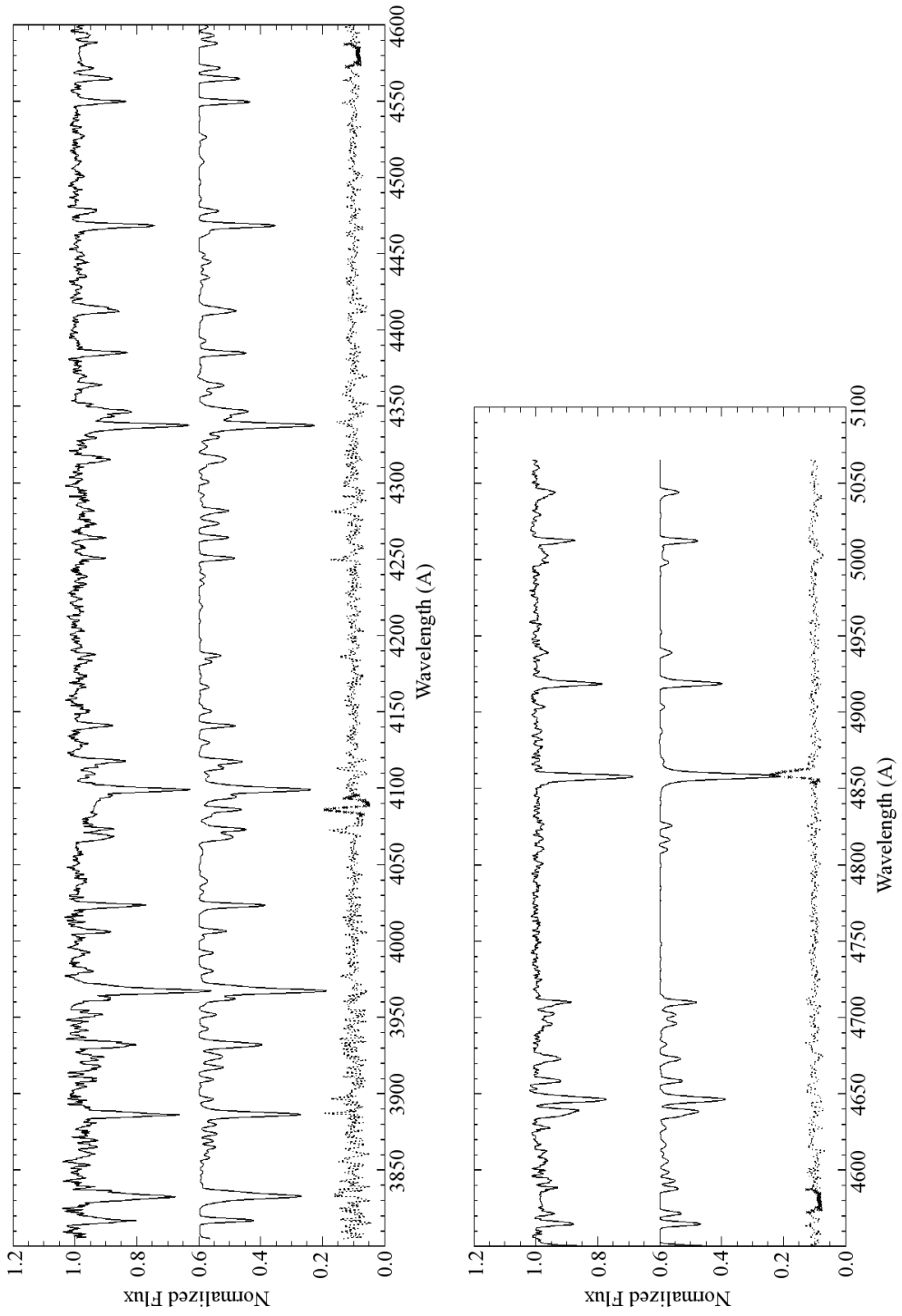

Figure 4.9. Comparison of the combined spectrum of the primary component of M31V J00444528+4128000 (SB1, up) with TLUSTY synthetic spectra (middle). The residuals of the fit are also shown (below, dotted line). Dark zones in the residuals (around 409 nm, 458 nm and 486 nm) show areas excluded from the fit.

Table 4.9. Parameters derived from the modeling of the merged spectrum for M31V J00444528+4128000 (SB1). TLUSTY atmosphere models and the values in Table 4.10 were used.

System properties				
Merged spectrum RV		-205.2±1.8		km s^{-1}
Metallicity ($[m/H]$)		-0.24±0.06		
Absolute magnitude (M_V)		-6.6±0.2		mag
Color excess ($E(B-V)$)		0.29±0.05		mag
Absorption (A_V)		0.90±0.17		mag
Component properties	Primary		Secondary	
Effective temperature ($T_{\rm eff}$)	21 200±300	K	11 200±700	K
Surface gravity ($\log g$ in cgs)	2.57±0.03		—	
Rotational velocity ($v_{\rm rot} \sin i$)	127±3	km s^{-1}	—	
Microturbulent velocity ($v_{\rm micro}$)	24.9±1.5	km s^{-1}	—	
Absolute V magnitude (M_V)	-6.4±0.2	mag	-4.6±0.3	mag
Intrinsic color ($(B-V)_0$)	-0.232±0.002	mag	-0.096±0.031	mag

Table 4.9 also lists values of M_V and $(B-V)_0$ for the system. The absolute magnitude of the primary component was derived after determining the absorption to primary component (Eq. 1.10) and correcting the observed V magnitude at maximum (Table 4.10) for the distance modulus of $(m-M)_0 = 24.44 \pm 0.12$ mag[3] (Table 4.4) and the flux ratio in V (Table 4.10). The intrinsic color was derived from the temperature and surface gravity, and using intrinsic colors tabulated in Lejeune & Schaerer (2001). The flux ratio in V passband and the temperature ratio (Table 4.10) were also used to determine the absolute luminosity of the secondary component. As in previous EBs, the reported uncertainties were obtained using the Monte Carlo technique with 20 different random noise realizations, corresponding to S/N=70.

4.1.3.3 Mass and radius determination

The mass and radius determination was performed following the fitting procedure described in Sect. 4.1.1.2. In this case, however, the lack of the signature of the secondary component (which is supposed to be filling the Roche lobe) in the spectra makes that the semi-major axis or the mass ratio have to be fixed in the W&D fit (Eq. 1.3). In our case, the relative radius of the primary can be obtained from the light curve fit and the absolute radius can be obtained from the absolute magnitude, since the effective temperature is known (Sect. 4.1.3.2). Therefore, the

[3]The distance modulus for SB2A is used instead of the mean value of Sect. 4.2 because the distance determination to SB2B was not available when this work was performed. In any case, the similarity of both results, well within the error bars, and the fact that SB2A has a temperature determination for both components, makes that the distance to SB2A can be considered highly accurate and capable, by itself, to fulfill the requirements of this analysis.

Table 4.10. Fundamental properties of M31V J00444528+4128000 (SB1) derived from the analysis with W&D.

System properties				
B magnitude at maximum light ($B_{\max}$)[a]	18.80±0.02			mag
V magnitude at maximum light ($V_{\max}$)[a]	18.73±0.03			mag
Period (P)	11.5435±0.0004			days
Time of minimum ($t_{\min}$)	2 451 814.55±0.03			HJD
Inclination (i)	66±2			deg
Systemic velocity (γ)	192±4			km s^{-1}
Semi-major axis (a)	74±5			$R_\odot$
Mass ratio ($q = \mathcal{M}_S/\mathcal{M}_P$)	0.51±0.09			
Temperature ratio ($T_{\mathrm{eff},S}/T_{\mathrm{eff},P}$)	0.53±0.03			
Flux ratio in B ($F_{B,S}/F_{B,P}$)[a]	0.17±0.02			
Flux ratio in V ($F_{V,S}/F_{V,P}$)[a]	0.19±0.03			
Flux ratio in V_{DIRECT} ($F_{D,S}/F_{D,P}$)[a]	0.19±0.03			
Component properties	Primary		Secondary	
Radius (R)	33±3	$R_\odot$	23±2	$R_\odot$
Mass ($\mathcal{M}$)	26±7	$M_\odot$	14±2	$M_\odot$
Surface gravity ($\log g$ in cgs)	2.82±0.05		2.84±0.04	
Radial velocity semi-amplitude (K)[b]	95±7	km s^{-1}	184±23	km s^{-1}
Synchronized rotational velocity ($v_{\mathrm{sync}} \sin i$)	132±13	km s^{-1}	92±5	km s^{-1}

[a] Out of eclipse average: $\Delta\phi = [0.20 - 0.32, 0.68 - 0.80]$

[b] Including non-Keplerian corrections

semi-major axis was fixed (after several iterations) so that the absolute radius of the primary was consistent with the value derived from the temperature determination process. The error in the radius determination was propagated to the derived quantities by performing several fits with the W&D using semi-major axis values in the range of the computed errors. The final rms residuals are 0.02 mag for the B light curve, 0.03 mag for both V light curves and 8 km s^{-1} for the RV curve. The light and RV curves, with their respective fits superimposed, are shown in Fig. 4.10.

The relatively large scatter in the resulting light curve fits cannot be explained entirely by the statistical error of the observations. In fact, the different clumps observed in the residuals (Fig. 4.10) correspond to observations taken during the same night, indicating that one of the components (or both) is intrinsically variable. Errors reported by W&D suppose that the dispersion of the fit is entirely due to random noise. Therefore, the variability observed in the light curves makes that the derived errors are likely not representative of the uncertainties in the derived parameters, even considering that a conservative value was adopted.

The resulting best fit elements for both components listed in Table 4.10 reveal two components with masses similar to those of SB2A and SB2B ($\mathcal{M}_P = 26 \pm 7$ $M_\odot$ and $\mathcal{M}_S = 14 \pm 2$ $M_\odot$). However, the derived radii are much larger ($R = 33 \pm 3$ $R_\odot$ and $R = 23 \pm 3$ $R_\odot$), which suggests that the components are evolved. In fact,

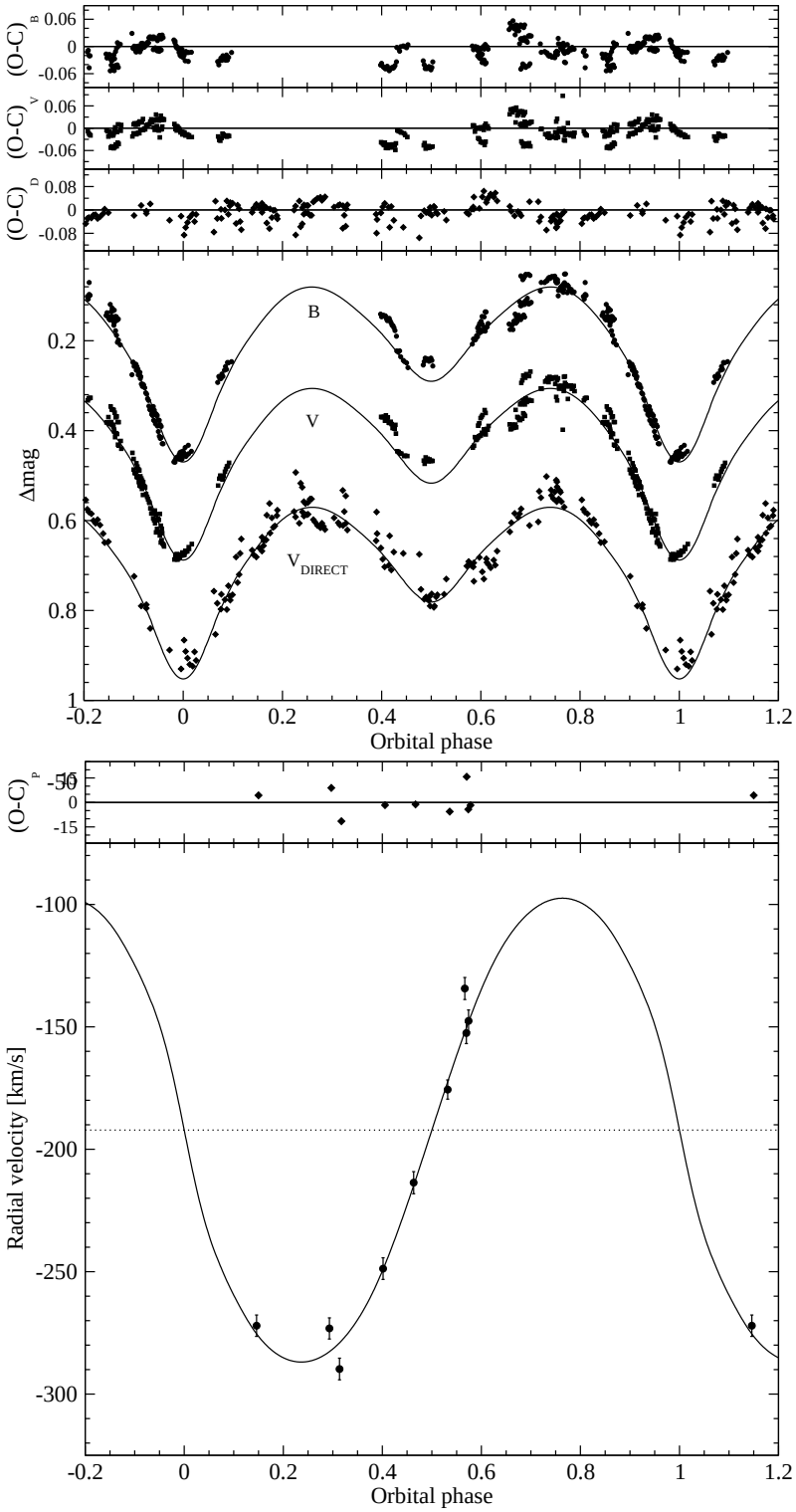

Figure 4.10. Observations for M31V J00444528+4128000 (SB1) and corresponding W&D fit. **Top:** Light curve fits and corresponding residuals. **Bottom:** RV curve fit with corresponding residuals.

the primary is almost filling the Roche lobe and, therefore, both components are almost in contact.

4.1.3.4 Comparison with stellar evolutionary models

As done in previous cases, the derived properties of M31V J00444528+4128000 (SB1) were compared with the stellar evolutionary models of Lejeune & Schaerer (2001). Again, the mass-radius diagram was used to consider the effect of mass loss and to derive evolutionary tracks with solar metallicity (Fig. 4.11).

The H-R diagram reveals that the primary component is at a phase of core helium burning. The derived evolutionary status is in agreement with the observed spectrum, which is typical of stars with luminosity class between Ia and Ib (Sect. 4.1.3.2. The supergiant nature of the primary component could well explain the observed scatter of ~ 0.02 mag in the residuals of the W&D fit (Sect. 4.1.3.3), since some of these stars are known to be variable (e.g., HD 86606, HD 148688, HD 169454). The derived radius, when compared with the rotational velocity (Table 4.9), indicates that the primary component rotational period is synchronized with the orbital period, which is expected since both components are almost in contact. The gravity value of $\log g = 2.82 \pm 0.05$ obtained with W&D for the primary component, is not consistent with the value of $\log g = 2.65 \pm 0.03$ derived from the spectroscopic fit (where the value of $\log g = 2.57 \pm 0.03$ was corrected from the centrifugal force, Fitzpatrick & Massa, 2005). However, there are two possible causes that could explain the difference between the observed and the modeled surface gravity. In first place, both components of SB1 are highly distorted by the presence of the nearby companion, with radius variations along their surfaces on the order of 10% (3 $R_\odot$ for the primary component) that greatly modify the surface gravity. Secondly, radiation pressure is known to have a non-negligible contribution in post-core-hydrogen-burning stars (see, e.g., Lamers & Fitzpatrick, 1988), making that the observed surface gravity of these stars is lower than expected for a given mass and radius. Therefore, all the derived properties identify this component as the first extragalactic blue supergiant with a dynamical determination of its mass and radius.

The secondary component is clearly underluminous for its mass. The low luminosity value cannot be explained by a circumstellar disk, since the secondary is filling its Roche lobe. In addition, supposing that the primary (instead of the secondary) fills the Roche lobe in the W&D fit results in parameters that are almost identical to the values presented in Table 4.10, excluding the possibility of a circumstellar disk. The disagreement with the evolutionary track cannot be explained by supposing that the luminosity of the secondary is in error, since a brighter secondary (with $F_{V,S}/F_{V,P} > 0.2$) would make that spectral lines were visible in the observed spectrum. Therefore, the most likely reason for the observed discrepancy is in the mass determination of the secondary. The mass of the secondary

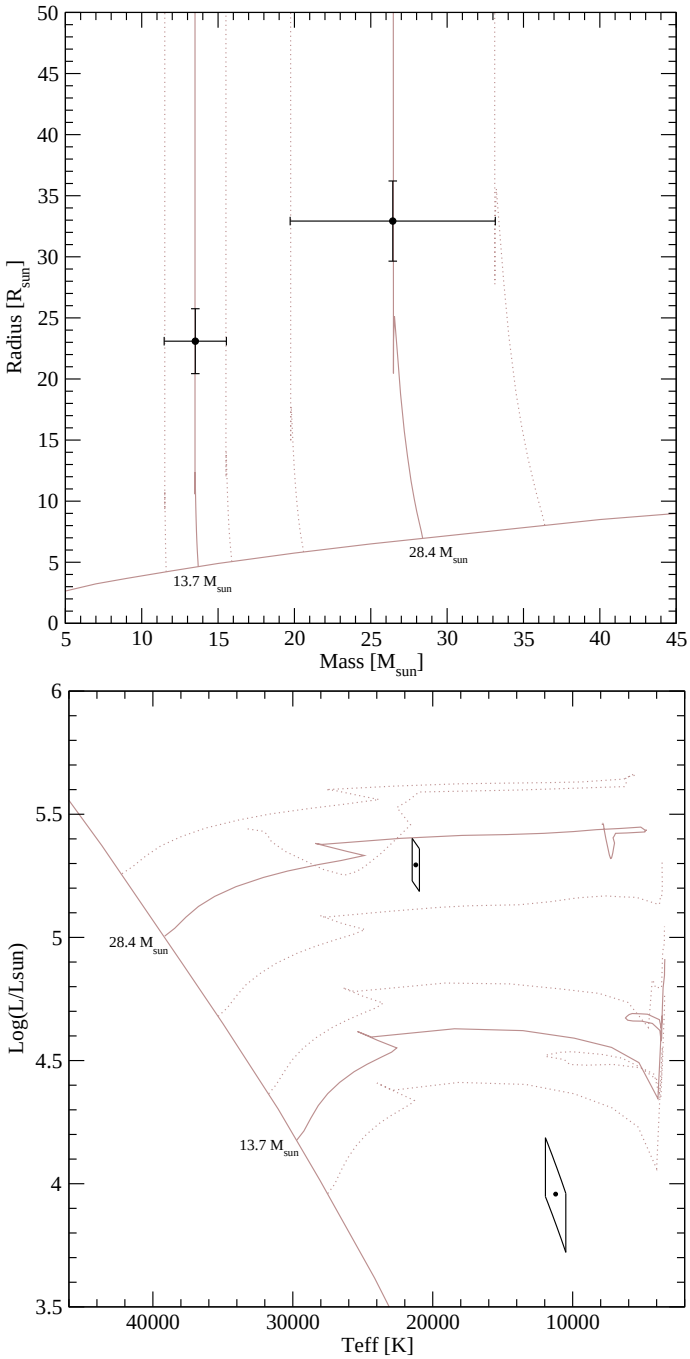

Figure 4.11. Comparison of stellar evolutionary models with derived physical properties of M31V J00444528+4128000 (SB1). Gray solid lines correspond to the ZAMS and the evolutionary tracks (initial masses are labeled). Gray dotted lines denote the uncertainties in the derived masses. **Top:** Mass–radius diagram. **Bottom:** H-R diagram. The skewed rectangular boxes correspond to 1σ error loci. Any possible systematic errors introduced by the variability observed in the light curves are not included.

is entirely derived from the mass ratio, which depends on the assumed value of the semi-major axis. In order to allow a different value of the semi-major axis without changing the absolute radius of the primary component (derived independently from the W&D fit), the relative radius of the primary should compensate the difference in the semi-major axis. In this sense, the relative radius of the primary could have some systematic error, since it is determined from light curves that present some variability. A systematic error ($\sim$ 10%) on the *relative* radius of the primary could explain the observed discrepancy between the evolutionary tracks and the derived properties of the secondary component. A light curve obtained during a single period (to reduce the effects of variability) could be worthy to clarify the real cause of the observed discrepancy. However, the identification of the lines of the secondary component would be definitive, since they would enable the determination of the mass ratio. Unfortunately, a telescope larger than Gemini-North is required.

4.1.4 M31V J00442326+4127082 (SB3)

4.1.4.1 Radial velocities

Three independent results support the idea that SB3 is a triple-line EB. First, the large third light contribution (l_3 = 0.33) derived from the preliminary light-curve analysis (Table 2.3). Second, the spectral lines are severely blended, even at quadratures (Fig. 4.12). And, finally, the RVs obtained supposing a double-line EB provide unphysical results or large residuals. Therefore, we decided to run a three-dimensional cross-correlation algorithm (TRIMOR) to determine the RVs of the three components.

TRIMOR (developed at the School of Physics of Astronomy of the Tel Aviv University in Israel) is a generalization of the TODCOR code used for the double-line EBs, prepared to perform three-dimensional cross-correlations for single-order or multi-order spectra. Therefore, the RV determination was performed following a similar procedure to that used for SB2B (Sect. 4.1.2.1). The main dif-

Table 4.11. Radial velocity determinations for M31V J00442326+4127082 (SB3).

Time [HJD]	Phase	Primary [km s^{-1}]	Secondary [km s^{-1}]	Tertiary [km s^{-1}]
2 453 260.910	0.1728	-444±26	62±17	-190±10
2 453 295.776	0.2336	-465±19	59±23	-210±10
2 453 264.066	0.7214	27±23	-503±19	-241±10
2 453 321.820	0.7610	70±14	-500±20	-235±11
2 453 321.872	0.7699	86±18	-495±13	-221± 9

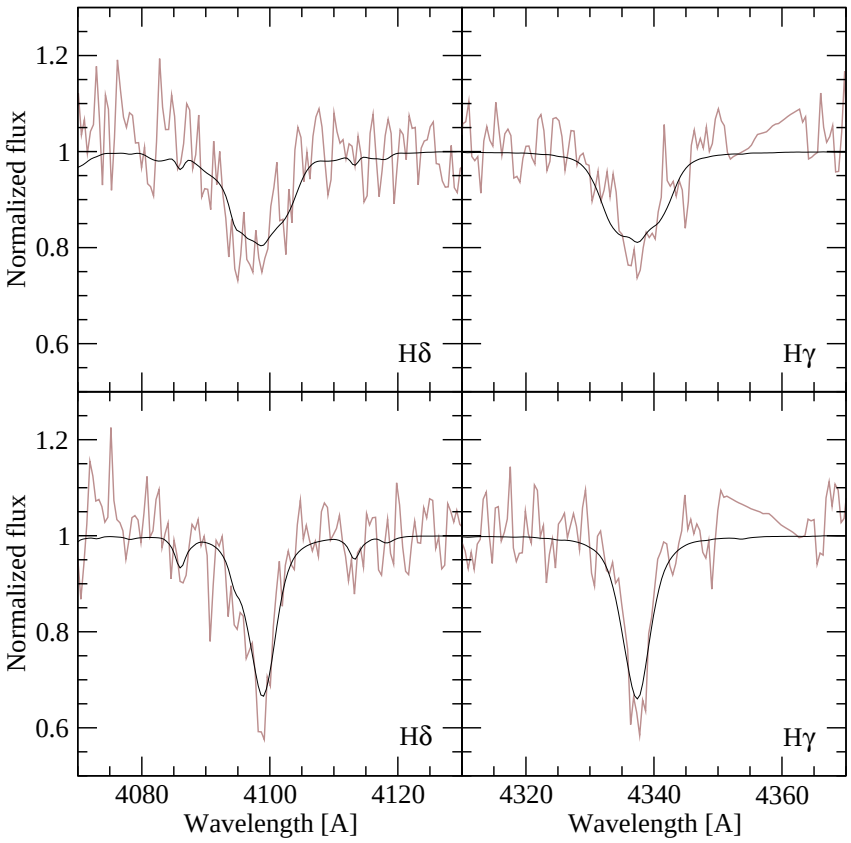

Figure 4.12. Balmer lines of M31V J00442326+4127082 (SB3) observed at two different orbital phases (0.23 top and 0.51 bottom). Gray lines correspond to the observed spectra and black lines correspond to the combination of three TLUSTY model spectra with the RVs, rotational velocities, luminosity ratios and surface gravities derived from the binary analysis (Sect. 4.1.4.2) and temperatures obtained from the comparison with stellar evolutionary models (Sect. 4.1.4.3).

ference is the number of attempted triplets of templates, somewhat lower, and the fact that only a single iteration was performed. The main reason for this is the large computational time required to obtain the RVs for each triplet of templates. The resulting RVs (Table 4.11) were corrected to the heliocentric reference frame (using standard IRAF routines) and rejected observations (after the W&D fit) are shown in Fig. 4.13. Again, all the rejected observations are close to the RV curve nodes or correspond to the spectrum with a shorter exposure time of February 2005.

4.1.4.2 Mass and radius determination

The RVs obtained for the two eclipsing components were used to derive their fundamental properties. The same procedure used for double-line EBs was followed,

Table 4.12. Fundamental properties of M31V J00442326+4127082 (SB3) derived from the analysis with W&D. Models of Lejeune & Schaerer (2001) were used for the tertiary.

System properties						
B magnitude at maximum light ($B_{\max}$)[a]			19.284±0.017			mag
V magnitude at maximum light ($V_{\max}$)[a]			19.195±0.014			mag
Period (P)			5.75268±0.00005			days
Time of minimum ($t_{\min}$)			2 452 546.586±0.008			HJD
Eccentricity (e)			0.17±0.02			
Argument of periastron (ω)			45±7			deg
Time derivative of ω ($\dot{\omega}$)			2.4±1.0			deg yr^{-1}
Inclination (i)			81.3±1.9			deg
Systemic velocity (γ)			-210±11			km s^{-1}
Semi-major axis (a)			62±2			$R_\odot$
Mass ratio ($q = \mathcal{M}_S/\mathcal{M}_P$)			0.94±0.07			
Temperature ratio ($T_{\rm eff,S}/T_{\rm eff,P}$)			0.97±0.02			
Flux ratio in B ($F_{B,S}/F_{B,P}$)[a]			0.9±0.2			
Flux ratio in V ($F_{V,S}/F_{V,P}$)[a]			0.9±0.2			
Flux ratio in $V_{\rm DIRECT}$ ($F_{D,S}/F_{D,P}$)[a]			0.9±0.2			
Third light contribution in B ($l_{B,3}$)			0.21±0.08			
Third light contribution in V ($l_{V,3}$)			0.20±0.09			
Third light contribution in $V_{\rm DIRECT}$ ($l_{D,3}$)			0.19±0.10			
Component properties	Primary		Secondary		Tertiary[c]	
Radius (R)	15.3±1.3	$R_\odot$	14.7±1.3	$R_\odot$	11±3	$R_\odot$
Mass ($\mathcal{M}$)	49±6	$M_\odot$	46±5	$M_\odot$	36±9	$M_\odot$
Surface gravity ($\log g$ in cgs)	3.76±0.07		3.77±0.08		3.92±0.10	
Radial velocity semi-amplitude (K)[b]	263±15	km s^{-1}	279±15	km s^{-1}	—	
Synchronized rotational velocity ($v_{\rm sync}\sin i$)	189±16	km s^{-1}	182±17	km s^{-1}	—	

[a] Out of eclipse average: $\Delta\phi = [0.04 - 0.45, 0.63 - 0.88]$
[b] Including non-Keplerian corrections
[c] Assuming a single coeval component

providing fits with rms residuals of 0.018 mag in B, 0.013 mag in V and 0.033 mag for the DIRECT V light curve. The residuals of the RVs are 11 km s^{-1} and 15 km s^{-1} for the primary and secondary components, respectively. The light and RV curves, with their respective fits superimposed, are shown in Fig. 4.13.

The resulting best-fitting elements, listed in Table 4.12, reveal a detached EB with two components having masses (and radii) of $\mathcal{M}_P = 49\pm6\ M_\odot$ ($R = 15.3\pm1.3$ $R_\odot$) and $\mathcal{M}_S = 46 \pm 5$ ($R = 17.7 \pm 1.3\ R_\odot$) for the primary and secondary components, respectively. The derived values reveal that SB3 is an extremely massive and eccentric EB showing apsidal motion ($\dot{\omega} = 2.4 \pm 1.0$ deg year^{-1}). The synchronized rotational velocity shown in Table 4.12 was computed assuming pseudo-synchronization, where both components are synchronized at periastron angular velocity. All these quantities, together with additional properties, are further discussed in Sect. 4.1.4.3.

4.1.4.3 Comparison with stellar evolutionary models

The triple-line spectra obtained for SB3 could not be disentangled and, therefore, a direct temperature determination could not be obtained. However, considering

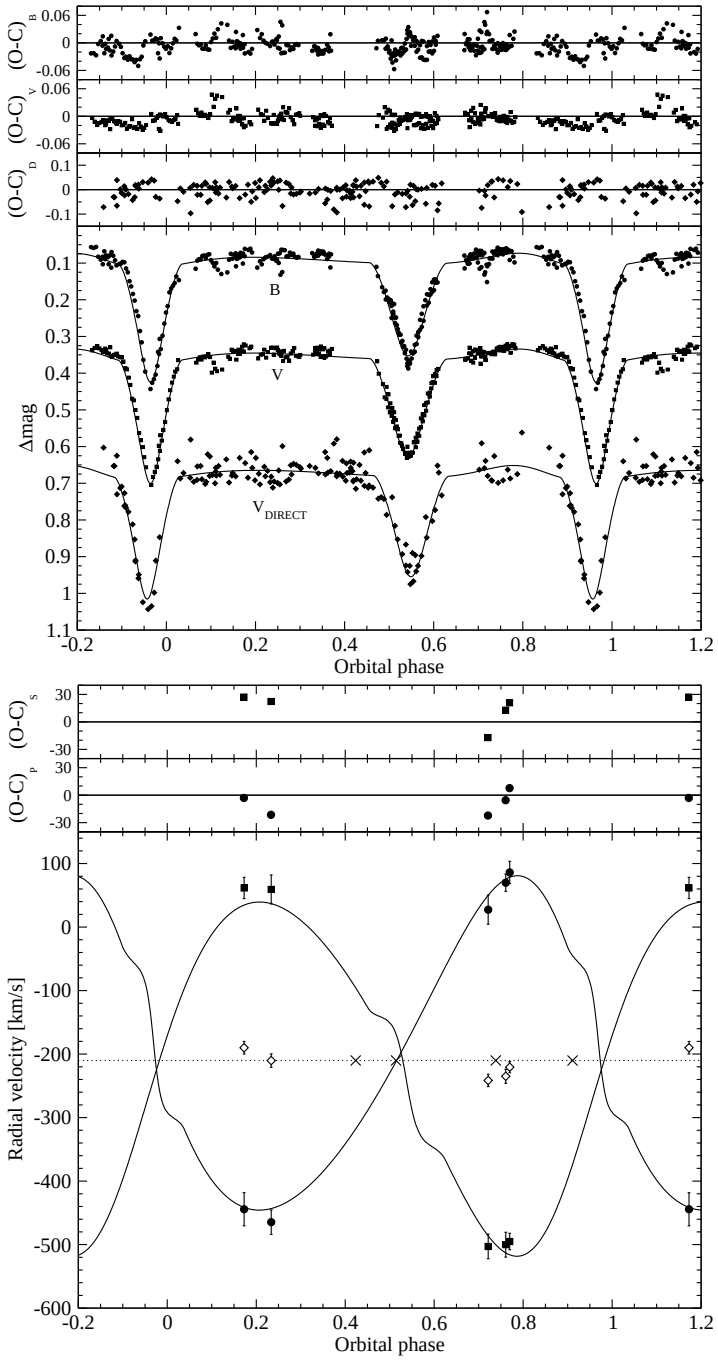

Figure 4.13. Observations for M31V J00442326+4127082 (SB3) and corresponding W&D fits. **Top:** Light curve fits and corresponding residuals. The residuals shown were derived for a mean epoch and do not consider the apsidal motion effect. **Bottom:** RV curve fits with RVs for the primary (circles), the secondary (squares) and the tertiary (empty diamonds) components, with corresponding residuals for the eclipsing components. Phases of rejected observations are also indicated (crosses).

Table 4.13. Fundamental properties of M31V J00442326+4127082 (SB3) derived from the comparison of the parameters in Table 4.12 with stellar evolutionary models of Lejeune & Schaerer (2001).

System properties						
Age					2.3±0.5	Myr
Absolute V magnitude (M_V)					-6.9±0.2	mag
Color excess ($E(B-V)$)					0.41±0.18	mag
Line-of-sight absorption (A_V)					1.3±0.6	mag
Distance modulus ($(m-M)_0$)					24.8±0.6	mag
Component properties	Primary		Secondary		Tertiary[a]	
Effective temperature ($T_{\rm eff}$)	40 000±2 000	K	40 000±2 000	K	39 000±3 000	K
Absolute V magnitude (M_V)	-5.93±0.17	mag	-5.82±0.20	mag	-5.1±0.5	
Intrinsic color ($(B-V)_0$)	-0.311±0.005	mag	-0.311±0.005	mag	-0.306±0.004	mag

[a] Assuming a single coeval component

that the eclipsing components are coeval, an accurate modeling of the system was obtained from comparison with stellar evolutionary models of Lejeune & Schaerer (2001).

As in previous cases, the mass-radius diagram was used to infer suitable evolutionary tracks with solar metallicity (Fig. 4.14). In this case, however, the detached nature of the system enabled us to assume that the components are coeval. In order to find the most likely coeval solution and the corresponding errors, a Monte Carlo simulation was performed with 1000 realizations. In addition to being coeval, the constraints derived from the W&D fits (i.e, temperature ratio, luminosity ratio and radius ratio) were also included. The resulting most likely models were used to determine the age, as well as the temperature and luminosity of both components (Table 4.13), revealing that both components are main sequence stars (Fig. 4.14).

The derived fundamental properties reveal a supermassive EB system, with the two components well above 40 $M_\odot$. In addition to determining the properties of the eclipsing components, the luminosity ratio could be used to infer the magnitude of the tertiary component. Considering the derived RVs of the tertiary component, it is reasonable to consider that all the stars belong to the same stellar association and are coeval. The resulting coeval absolute magnitude is $M_V = -5.1 \pm 0.5$ mag.

The large uncertainty in the computed M_V magnitude prevents a precise determination of other properties for the tertiary component. In addition, the third light contribution could be due to one or several stars. However, to explain the relatively bright M_V magnitude, the tertiary component has to be composed by one (or several) hot stars (i.e., $T_{\rm eff} > 30\,000$ K). To further confirm this scenario, a synthetic spectrum was generated with three equal stars (with the properties inferred from the binary analysis) and compared to the observed spectra (Fig. 4.12). After some attempts, it was observed that the rotational velocity of the tertiary component had to be rather low (40 km s^{-1} in Fig. 4.12) to reproduce the observed line depths. In

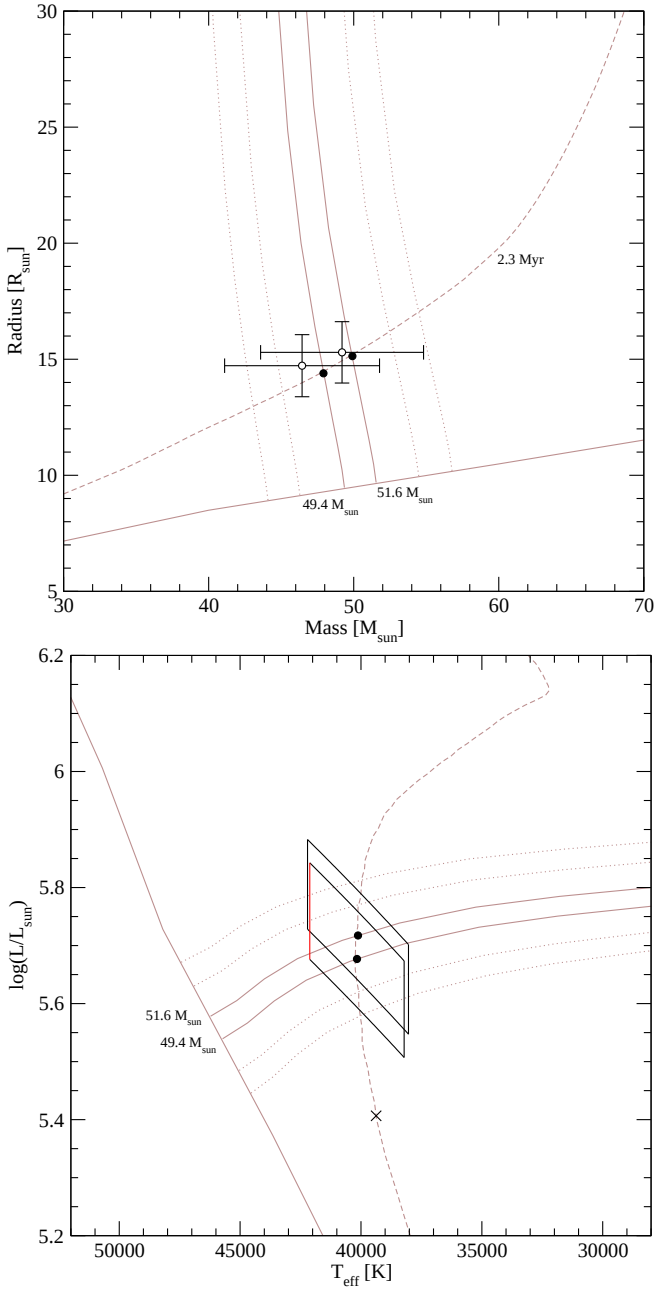

Figure 4.14. Comparison of stellar evolutionary models with derived physical properties of M31V J00442326+4127082 (SB3). Results obtained after the W&D fitting are shown (open circles) together with the most likely coeval solution (black circles). Gray solid lines correspond to the ZAMS and the evolutionary tracks (initial masses are labeled). The best fitting isochrone of 2.3 Myr is also shown (gray dashed line). Gray dotted lines denote the uncertainties in the derived masses. **Top:** Mass–radius diagram. **Bottom:** H-R diagram. The skewed rectangular boxes correspond to 1σ error loci. The coeval position of the tertiary source is also shown (cross).

any case, the combined spectra seem to be capable of reproducing the observed shapes of the lines rather well considering the noise of the observed spectra.

The most distinctive characteristic of SB3 is the large measured apsidal motion. The measured value of $\dot{\omega} = 2.4 \pm 1.0$ deg year^{-1}, in combination with the derived masses, converts SB3 into the most massive EB system with measured apsidal motion ever reported. The measured apsidal motion rate can be compared with theoretical predictions and will be subject of future investigation. So far, three possible causes can be put forward to explain the observed apsidal motion (see Guinan & Maloney, 1985, for details).

Firstly, the presence of a third body can introduce an apsidal motion (together with additional effects, for instance in the inclination). However, even supposing that the third body is tidally bound, forming a triple system with the EB, the derived RVs for the tertiary component reveal that the rotational period of the supposed triple system is much longer (> 100 times longer) than the EB period. Since the angular motion rate depends on the ratio of periods as $(P/P')^2$, where P is the EB period and P' is the triple system period, the effect of the third body on the apsidal motion has to be several orders of magnitude lower than the observed value.

Secondly, general relativity introduces an advance in the periastron that, for some EB systems, is large enough to be observed. In this case, however, the relativistic effect introduced in the apsidal motion is on the order of 0.2–0.3 deg yr^{-1}, much lower than the observed apsidal motion.

Finally, the most likely cause for the observed apsidal motion is due to the deformation of the components. The apsidal motion rate depends on the eccentricity of the EB system, the relative radius of the components, the mass ratio, the period and rotational velocity (Claret & Gimenez, 1993). In addition, the distribution of matter in the interior of the stars (modeled as internal structure constants, k_2) are critical values to determine the apsidal motion rate. Using the values tabulated in Claret (2004), the internal structure constants derived for the primary and the secondary components are $\log k_{21} = -2.44 \pm 0.16$ and $\log k_{22} = -2.52 \pm 0.17$. These values, when combined with the parameters derived from the binary analysis (Table 4.12) and assuming pseudo-synchronization, result in a predicted apsidal motion rate of $\dot{\omega}_{\rm theo} = 5.4 \pm 0.8$ deg year^{-1} or, equivalently, a period of apsidal revolution of $U_{\rm theo} = 66 \pm 10$ years. This value is discordant (at the 2σ level) with the observed apsidal motion rate of $\dot{\omega} = 2.4 \pm 1.0$ deg year^{-1} ($U = 150 \pm 60$ years). The same situation is observed for other B stars with convective cores (e.g., V380 Cyg and CO Lac Guinan, 1993; Guinan et al., 2000). The general explanation for the observed discrepancy is that the internal structure constants predicted by the stellar evolution models are too large, implying too small convective cores. Therefore, the observed apsidal motion rate seems to support the idea that the internal structure constants predict cores that are too small when compared with observations. In any case further analysis is needed to better ensure that the ob-

Table 4.14. Distance determinations to M 31 from EBs.

EB system	V [mag]	M_V [mag]	A_V [mag]	$(m-M)_0$ [mag]	Distance [kpc]
SB2A	19.27±0.02	-5.77±0.06	0.60±0.10	24.44±0.12	772±44
SB2B	19.948±0.015	-4.90±0.08	0.55±0.08	24.30±0.11	724±37
SB3	19.195±0.014	-6.9±0.2	1.3±0.6	24.8±0.6	910±250

served apsidal motion is caused by the internal structure of their components and not by other factors (such as a tertiary component).

As a final remark, it is worth mentioning that absolute magnitudes could be derived from the comparison with stellar evolutionary models. Therefore, the derived luminosities could be used to obtain a line-of-sight absorption and a distance modulus to M 31 (Table 4.13), revealing a highly reddened system. The large uncertainty in the third light contribution, combined with the unknown total-to-selective extinction ratio ($\mathcal{R}_V$), makes that the derived distance is highly uncertain. In any case, the resulting distance is within one sigma of the direct distance determinations obtained with SB2A and SB2B (Sect. 4.1.1 and Sect. 4.1.2) and further confirms the scenario described for SB3.

4.2 Distance determination

From the four analyzed EBs, three of them have provided a distance determination to M 31 (Table 4.14). As previously mentioned (Sect. 4.1.1.3), the derived distances to each EB correspond to the center of M 31, because the correction due to the location of the EB is negligible ($\sim 0.3\%$). Therefore, the derived distances, in mutual agreement within their one sigma error bars, prove that EBs can be used to derive precise and accurate distances to M 31.

The derived distances can be averaged to derive a robust distance to M 31. Of the three distance determinations, only two can be considered direct distance determination. The distance value of SB3 cannot be considered to be direct because it is based on stellar evolutionary models. As it is well known, stellar evolutionary models depend on a certain number of assumptions that can affect the derived distance (mass loss, rotational velocity, isolated stellar evolution, etc.). In any case, the large error associated with the distance to SB3 makes that the weighted mean value would vary only slightly if the SB3 distance determination is included. Therefore, the two double-line EBs have been combined to derive a weighted mean distance to M 31 of 744 ± 33 kpc or $(m-M)_0 = 24.36 \pm 0.08$ mag. Although additional EBs are needed to increase the statistical significance, the derived result has an error of only 4%, which is remarkable, given the faintness of the studied targets.

Note that the error bars account for the random uncertainties of the parameters but do not include a possible systematic contribution from the atmosphere models. However, stellar atmosphere models are used in a large number of applications and have been tested thoroughly in several research areas. In addition, our spectrophotometric measurements are fully compatible with stellar atmosphere models, reducing the possibility of important systematics in the models. Therefore, we expect such systematic error to be no larger than a few per cent in flux, having an effect below 0.05 mag in the distance modulus.

Another possible source of systematic error is the fact that both EBs used for distance determination are modeled as semi-detached systems. It has traditionally been argued that detached EBs are the only systems capable to provide accurate distances. The most common reason is that non-detached EBs are affected by the proximity of the components, introducing distortions and reflection effects. However, the proximity of the components can properly be taken into account by current modeling algorithms (such as W&D). In addition, the fact that one of the components fills the Roche lobe decreases the number of free parameters and greatly improves the stability of the solution (Wyithe & Wilson, 2002). On the other hand, there are some other effects, missing in detached EB, that could introduce some systematics in the solutions (e.g., hot spots, circumstellar disks, etc.). In any case, these effects can be observed from the acquired data and properly taken into account. A clear example of these effects is the presence of the O'Connell effect in SB2A. The modeling performed, with the introduction of a hot spot, has been capable to accurately consider this effect, allowing the use of SB2A for distance determination. Therefore, using semi-detached EBs reduces the number of free parameters, at the cost of introducing some other effects that, when properly considered, should introduce no systematic error in the derived distances.

It is also important to remark that the procedure used in the present work, although resource-intensive, is completely independent of any other distance determination. Therefore, with this procedure, distance determination is both highly precise and direct. In addition, without the need for spectrophotometry, the observational requirements decrease, which greatly simplifies the procedure and opens the possibility to perform distance determinations for a large number of EBs.

The need for spectrophotometry could be circumvented because we derived $T_{\rm eff}$ from the disentangled spectra and benefit from the weak temperature dependency of $(B-V)$ above $\sim$ 30000 K to obtain an $E(B-V)$ value. The major cost of loosing spectrophotometric information is an increase in the line-of-sight absorption uncertainty. In fact, uncertainty in the extinction represents $\sim$50% of the total error in the distance determination. Therefore, any further improvements that reduced the uncertainty in the line-of-sight absorption could potentially improve the distance determinations presented here.

5 Cepheids*

The importance of Cepheids for distance determination (Chap. 1) stands in contrast with the relative lack of additional information on the specific characteristics of extragalactic Cepheids and the possible corrections because of their particular properties (i.e., metallicity). A clear example is the Andromeda galaxy (M 31), where the first identification of Cepheids was already performed by Hubble (1929). After the observations of Baade & Swope (1965, and references therein), little effort has been dedicated to further analyze the Cepheid population in M 31.

This trend has changed in recent years with the emergence of new observational capabilities. Several variability surveys have started to study the stellar content of M 31 (Macri, 2004, and references therein) and other Local Group galaxies (Udalski et al., 1999; Mochejska et al., 2001b; Udalski et al., 2001; Pietrzyński et al., 2004; Macri et al., 2006), obtaining large samples of Cepheids with accurate photometry. The detailed study of the observed Cepheids has emphasized the importance of an issue that was usually overlooked in most photometric studies: the effect of blending. It has been proposed (Mochejska et al., 2000, hereafter MMSS00) that the magnitude of Cepheids may be affected by the light of unresolved companion stars (i.e., blends). The effect of blending is somewhat different from crowding or confusion noise, since companion stars appear to be in the same point-like source. Therefore, even when achieving a perfect point-spread function modeling, blending could still be present. The effect can be the same as in spectroscopic binaries, where the individual components cannot usually be resolved from ground-based images.

When studying extragalactic Cepheids the spatial resolution decreases linearly with the distance of the host galaxy and, as a consequence, the number of possible blends increases. Small blending values are expected for the Large Magellanic Cloud (LMC), where individual Cepheids can be resolved from neighboring stars, even from ground-based observations. The situation changes in M 31 and M 33,

*The contents of this chapter were published in Vilardell et al. (2007).

where mean *V* blending values of 19% and 16%, respectively, have been obtained (Mochejska et al., 2004, hereafter MMSS04). These results would imply, when extrapolated to more distant galaxies, a downward revision of the Hubble constant between 5% to 10% (as explained by Gibson et al., 2000). In contrast, Bresolin et al. (2005) found an upper limit on blending in NGC 300 (at $\sim$ 2 Mpc) of 0.04 mag. In addition, Gibson et al. (2000) showed that the systematic effect of blending on farther galaxies (between 4 and 25 Mpc) is almost negligible. Therefore, results obtained so far seem to indicate that blending has an important contribution when observing Local Group galaxies and diminishes when observing distant galaxies. Gibson et al. (2000) explained such behavior as a consequence of the background levels in M 31 and M 33 (with a large number of stars detected around Cepheid variables) not being representative of the more distant galaxies (where the background levels are the result of several unresolved sources). Because of the importance of the subject, a comprehensive study of the effect of blending on Cepheid distance determinations is highly desirable.

The variability survey in Chap. 2 represents an excellent dataset for these studies. The large number of detected stars (416 Cepheids) and the high quality of the resulting light curves have allowed a comprehensive study of Cepheid properties in M 31.

5.1 Period distribution

The period distribution of Cepheids in Local Group galaxies has been a major source of debate. Evolutionary models predict a displacement on the peak of the period distribution as a function of the metallicity of the host galaxy (Becker et al., 1977). It has also been observed that the Milky Way (MW) period distribution displays a dip at around 10 days, while such feature is missing in more metal-poor galaxies such as the LMC. Several theories have been put forward to explain the bimodal distribution, but a satisfying scenario is still lacking (see Antonello et al., 2002, for an extended discussion).

Since the MW and M 31 have similar morphological types and chemical compositions, the observed period distributions are also expected to be similar. The results obtained so far have prevented a direct comparison because of observational biases, which are often difficult to evaluate. On the one hand, faint Cepheids (with usually short periods) can be missing in some shallow surveys while, on the other hand, the distribution of the observations can make the identification of long period Cepheids difficult.

To evaluate the observational biases, the 416 Cepheids from the variable star catalog in Chap. 2 (hereafter VSC sample) were compared with the 420 Cepheids in M 31 of the GCVS (Samus et al., 2004). Both samples have almost the same number of stars, but the two period distributions (Fig. 5.1) are found to be largely

different, as demonstrated by the Kolmogorov-Smirnov tests, which provide values of around 10^{-13}. The origin of the observed difference can be explained by two main factors. Firstly, the VSC sample is known to have a bias for the longest period Cepheids because of the observational window function (see Chap. 2 for further information). And secondly, the GCVS presents an important bias at short periods because the GCVS is shallower than our survey and faint Cepheids are missing. Furthermore, both Cepheid samples in M 31 can be compared with the MW sample of the David Dunlap Observatory[1] (DDO, Fernie et al., 1995). As can be seen (Fig. 5.1), the period distributions of the VSC and the DDO sample are very similar (with a Kolmogorov-Smirnov test value of 0.49). Only a slight difference is observed at long periods, possibly because of the observational bias in the VSC sample. Therefore, as expected, equivalent period distributions are obtained for similar galaxies, including the secondary peak at $P > 10$ d in metal rich galaxies.

The conspicuous similarity between the period distributions of MW and M 31 becomes even more striking when compared with a galaxy of different metallicity (Fig. 5.1). More than 1300 Cepheids have been observed in the LMC as part of the OGLE II survey[2] (Udalski et al., 1999). The resulting period distribution reveals a single peak, which, as expected, is shifted towards shorter periods with respect to those of the distributions of the MW and M 31. Therefore, the great similarity between the DDO and VSC samples indicates that both the observational biases and period distributions are equivalent.

5.2 Fourier decomposition

It is well known that Fourier decomposition of the Cepheid light curves can provide valuable information on the real nature of these variable stars, especially on their pulsation modes (Beaulieu et al., 1995). The procedure involves fitting the coefficients (A_k and φ_k) of a Fourier series of the form:

$$m(t) = A_0 + \sum_{k=1}^{J} A_k \cos\left(2\pi k \Phi(t) + \varphi_k\right) \tag{5.1}$$

where $m(t)$ and $\Phi(t)$ are the magnitude of the Cepheid and the phase at time t, respectively. Once the best coefficients have been obtained, the pulsation mode of the Cepheid variable can be derived from the amplitude ratio $R_{k1} = A_k/A_1$ and phase difference $\varphi_{k1} = \varphi_k - k\varphi_1$.

[1] Data obtained from:
http://www.astro.utoronto.ca/DDO/research/cepheids/cepheids.html

[2] Data obtained from:
ftp://sirius.astrouw.edu.pl/ogle/ogle2/var_stars/lmc/cep/catalog/

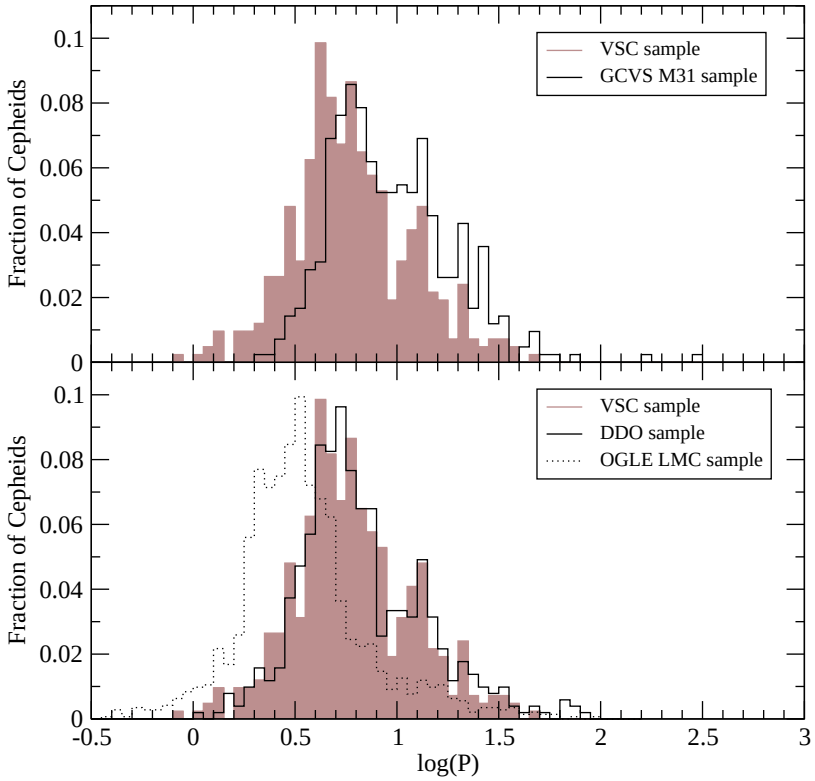

Figure 5.1. Top: normalized period distribution for the 416 detected Cepheids in VSC compared with the 420 Cepheids in M 31 of the GCVS. **Bottom**: normalized period distribution for the 416 detected Cepheids in M 31 compared with the 509 Cepheids in the MW from the DDO sample. The OGLE LMC Cepheid sample is also shown for comparison.

A prerequisite of the Fourier decomposition of the 416 Cepheids identified in M 31 is the determination of the maximum order of the fit, J. In agreement with other studies in the literature (Antonello et al., 1990; Beaulieu et al., 1995; Zakrzewski et al., 2000), we observed that an iterative solution provided satisfactory results. Therefore, for each light curve, the fitting procedure started with $J = 1$ and increased until the value of χ^2_{dof} varied by less than one. Although the Fourier fit always provided values for all the light curves, several important aspects were considered before studying the results. Firstly, since measurements with large photometric errors can provide unreliable fits, light curves with a mean photometric error larger than 0.1 mag were excluded. Secondly, all light curves with $\chi^2_{dof} > 7$ were rejected to eliminate the fits that did not accurately match the observations. Finally, large gaps in a light curve can prevent the fit to correctly reproduce its shape, even when χ^2_{dof} is relatively low. Problematic fits usually have coefficients with large error bars. Therefore, coefficient errors were computed (according to Petersen, 1986) and light curves with $\sigma_{A_0} > 0.01$ mag, $\sigma_{R_{21}} > 0.1$, or $\sigma_{\varphi_{21}} > 0.6$ rad ($\simeq 0.2\pi$ rad) were also rejected.

The above criteria yielded a sample of 315 Cepheids with accurate Fourier fits in both passbands (B and V). The R_{21} and φ_{21} values in *both passbands* (Fig. 5.2) have been used to classify 75 Cepheids pulsating in the first-overtone mode (FO) and 240 pulsating in the fundamental mode (FM). Since FO Cepheids are not expected to have periods longer than $\sim$ 7 days, the FM sample has been completed with all Cepheids with $\log P > 0.9$ ($\simeq$ 8 days), regardless of the quality of their Fourier fit. The final sample of 281 FM Cepheids includes three type II Cepheid candidates, but they are easily identified as a consequence of the detailed analysis of the P-L distribution (Sect. 5.3.1).

5.3 Period-luminosity relationship

The P-L diagram for the 356 classified Cepheids (281 FM and 75 FO) reveals a large scatter in both passbands (Fig. 5.3), especially in *B*. The origin of the observed scatter can be understood if we consider that the field of view covers about 7 kpc at the distance of M 31 ($(m-M)_0 = 24.44 \pm 0.12$ mag, Sect. 4.1.1.3)[3]. The large covered area in M 31, the fact that Cepheids are located along the spiral arms, and the clumpy structure of the interstellar medium (clearly observed in the survey images), indicates that differential absorption in the disk is most likely responsible for an important fraction of the observed scatter. In addition, the larger dispersion of the P-L distribution in B compared to V reinforces the interstellar absorption hypothesis.

Another possible effect on the observed scatter is metallicity. Several authors have suggested (see, i.e., Gieren et al., 2005) that the slope of the Cepheid P-L relationship is basically independent of metallicity. However, comparison of the tip of the red giant branch and Cepheid distance determinations to several galaxies has shown that a slight dependence on metallicity is present (Sakai et al., 2004). Therefore, a metallicity dependence on the zero-point of the Cepheid P-L relationship could exist. Since metallicity within M 31 decreases as a function of the galactocentric distance (Zaritsky et al., 1994), some of the observed scatter could also be introduced by metallicity differences.

In addition, the Cepheid measured photometry can be affected by blends. The mean seeing of our images is around 1 arcsec. Therefore, each observed point-like source corresponds to $\sim$4 pc at the distance of M 31. Since Cepheids are usually located in young star clusters and associations, it is likely that the observed magnitude of a Cepheid can be the combination of several unresolved sources.

[3] In course of this work, the distance modulus for SB2A is used instead of the mean value of Sect. 4.2 for consistency with the published version (the distance determination to SB2B was not available when this work was published). In any case, the similarity of both results, well within the error bars, and the fact that SB2A has a temperature determination for both components, makes that the distance to SB2A can be considered highly accurate and capable, by itself, to fulfill the requirements of this analysis.

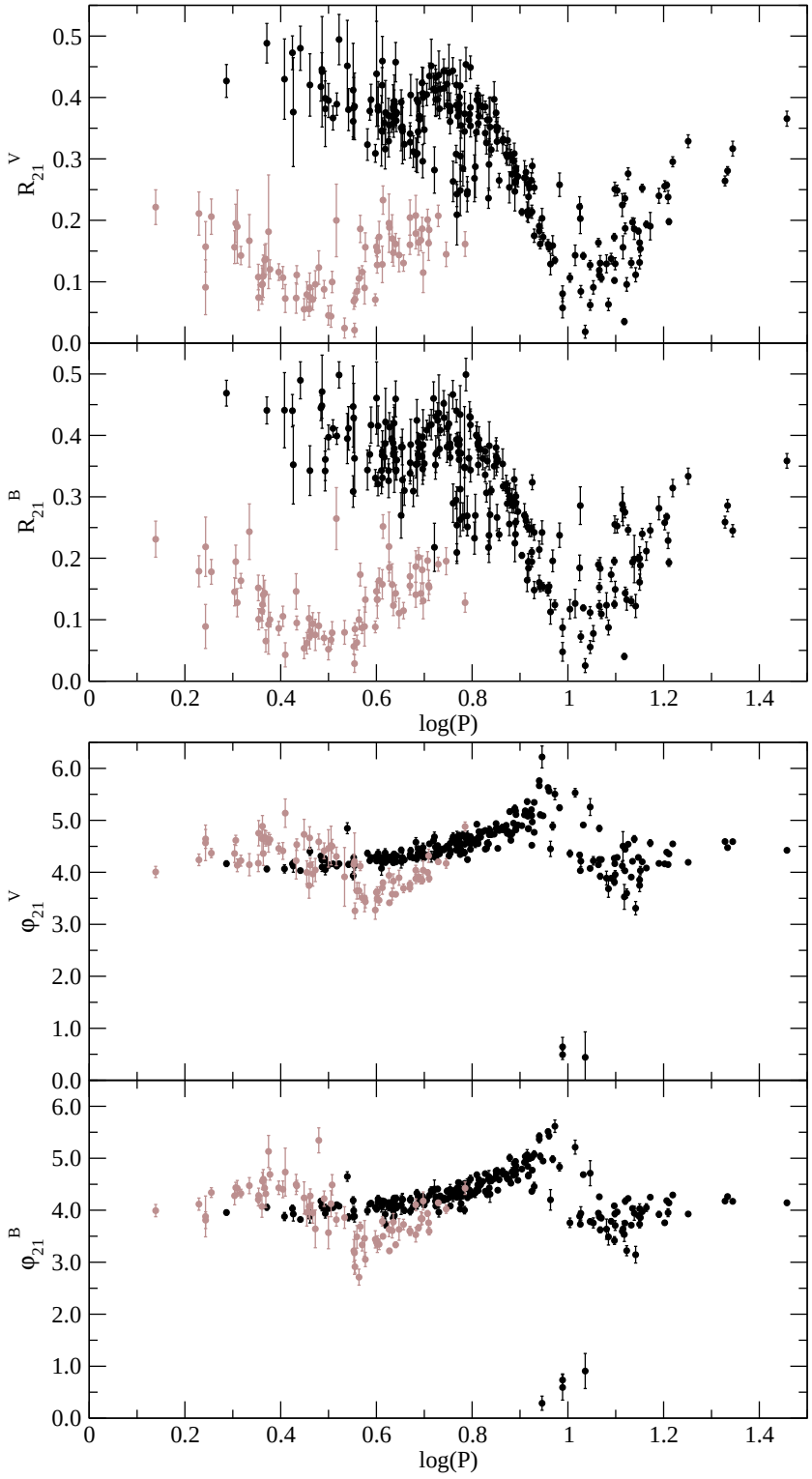

Figure 5.2. Fourier coefficients in each passband (*B* and *V*) as a function of period. The pulsation mode of the 315 Cepheids is identified: black circles – fundamental mode; gray circles – first overtone.

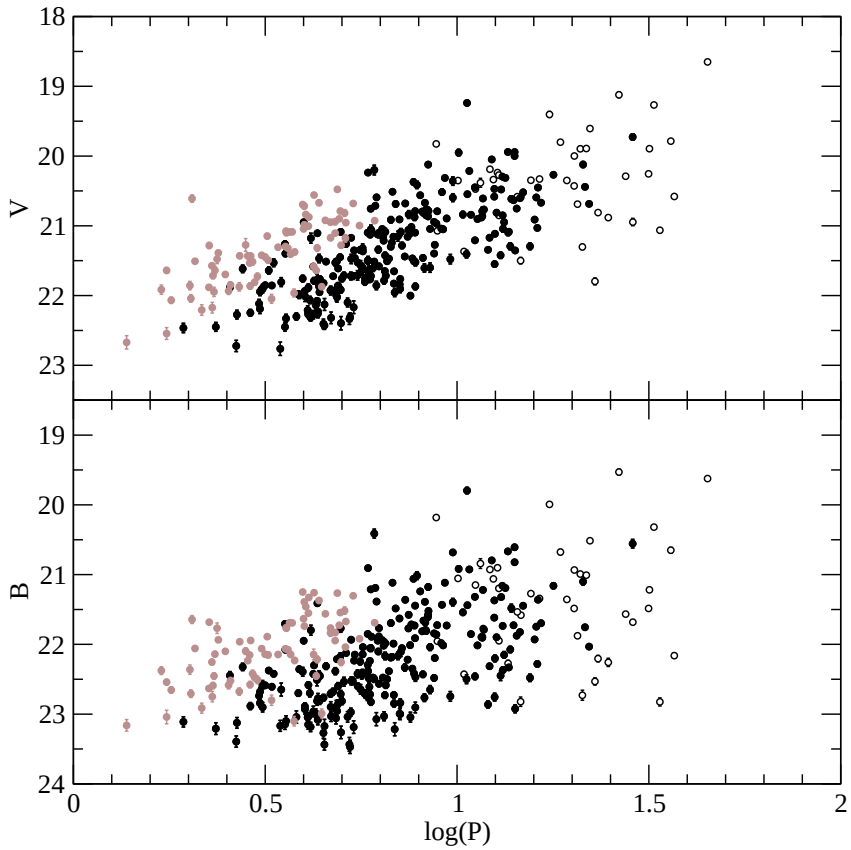

Figure 5.3. Observed magnitudes as a function of period for 356 Cepheids. Filled black circles: fundamental mode Cepheids with accurate Fourier coefficients. Empty black circles: fundamental mode Cepheids without accurate Fourier coefficients. Gray circles: first overtone mode pulsators.

Below we analyze the three aforementioned effects that are the most probable sources of the scatter in the P-L diagram.

5.3.1 Absorption

The effect of differential absorption can be partially corrected from the observed Cepheid color $(B-V)$ through the color-excess ($E(B-V) \equiv (B-V) - (B-V)_0$, see Feast, 1999, as an example). We used P-L relationships from Udalski et al. (1999)[4] to estimate B_0 and V_0 values. The LMC distance modulus was assumed to be $(m-M)_0 = 18.42 \pm 0.06$ mag and was computed from the weighted mean of all the LMC distance determinations with eclipsing binaries (Table 1.3). The reason for using LMC relationships (instead of those for the MW), was moti-

[4]Updated relationships were obtained from the OGLE II web site:
`ftp://sirius.astrouw.edu.pl/ogle/ogle2/var_stars/lmc/cep/catalog/README.PL`

vated by several recent results. First, Gieren et al. (2005) suggested that the MW Cepheid distances, mostly obtained through the Baade-Wesselink method, could be affected by a systematic bias when converting the observed radial velocities into pulsation velocities. Second, Macri et al. (2006) found that LMC P-L slopes provide a better agreement with the P-L distribution of Cepheids in NGC 4258 than MW relationships. Finally, the new parallax measurements of several MW Cepheids (Benedict et al., 2007; van Leeuwen et al., 2007) yield P-L slopes that seem to be in better agreement with the LMC than with previous MW relationships.

After obtaining the color excess for each Cepheid, a total-to-selective extinction ratio of $\mathcal{R}_V \equiv A(V)/E(B-V) = 3.1 \pm 0.3$ (Fitzpatrick, 1999) was used to compute the absorption and the V_0 magnitude for every Cepheid. The resulting P-L distribution can be compared with the LMC P-L relationship (Fig. 5.4), assuming a M 31 distance modulus of $(m-M)_0 = 24.44 \pm 0.12$ mag (Sect. 4.1.1.3). An offset between the V_0 values and the LMC P-L relationship is clearly observed, but the effects of metallicity and blending have still to be considered.

Finally, as previously mentioned, three of the studied Cepheids seem to be of type II. To further investigate these objects they have been kept in the studied sample of FM Cepheids (Sects. 5.3.3 and 5.4).

5.3.2 Metallicity

As explained above, the zero-point of the P-L relationship may depend on metallicity. To account for this effect, the metallicity of each Cepheid needs to be estimated, and we did so by considering a galactocentric metallicity dependence. According to Zaritsky et al. (1994), the M 31 galactocentric metallicity dependence can be modeled by:

$$12 + \log(O/H) = (9.03 \pm 0.09) - (0.28 \pm 0.10)(\rho/\rho_0 - 0.4) \qquad (5.2)$$

where ρ is the de-projected galactocentric radius and ρ_0 is the isophotal radius (77.44 arcmin for M 31). Following the procedure in Baade & Arp (1964), the Cepheid galactocentric radius was obtained assuming a position angle of 38°, an inclination of 12.°5 (Simien et al., 1978), and an M 31 center position of $\alpha = 00^h42^m44\overset{s}{.}31$ $\delta = +41°16'09\overset{''}{.}4$ (in J2000.0 coordinates, Cotton et al., 1999).

The metallicity dependence of the Cepheid P-L relationship and the galactocentric metallicity variation implies that a different P-L relationship must be used for each individual Cepheid when computing the value $V_0 - M_V$. Alternatively, one can compute $V_0 - M_V$ by using a universal P-L relationship and then applying a correction for each Cepheid *a posteriori*. According to Sakai et al. (2004), the correction on the computed $V_0 - M_V$ value is $\delta(m-M)_0/\delta(O/H) = -0.25 \pm 0.09$ mag/dex when using the Udalski et al. (1999) P-L relationships. Therefore, for

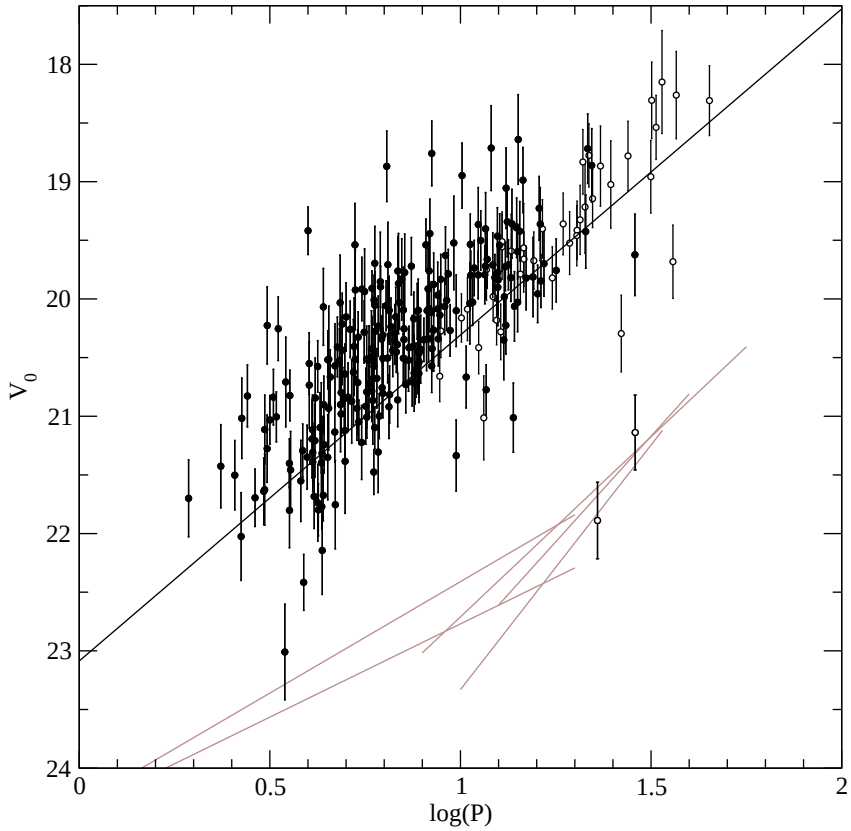

Figure 5.4. Absorption-corrected V magnitude as a function of period for 281 fundamental mode Cepheids. Filled circles: stars with accurate Fourier fit. Empty circles: stars without accurate Fourier fits. Black line: Udalski et al. (1999) P-L relationship, for a distance modulus to M 31 of 24.44 mag (Sect 4.1.1.3). Gray lines: distance corrected P-L relationships for type II Cepheids as given by Alcock et al. (1998).

each Cepheid, we computed metallicity corrections ($\delta(O/H)$) by comparing the metallicity given by Eq. 5.2 with the metallicity of the LMC ($12+\log(O/H) = 8.5$ dex, Sakai et al., 2004). The resulting metallicity corrections were then used to derive the corresponding $\delta(m - M)_0$ for each Cepheid in the sample, providing corrections between -0.15 mag and -0.05 mag.

5.3.3 Blending

The best approach to study the effect of blending given our available data set is by using the observed Cepheid amplitudes (Antonello, 2002). The intrinsic amplitude $\mathcal{A}^i$ of a Cepheid is given by the expression:

$$\mathcal{A}^i = -2.5 \log\left(\frac{f_c}{F_c}\right) \tag{5.3}$$

where f_c and F_c are the fluxes at minimum and maximum light, respectively. When blending is present, the observed amplitude $\mathcal{A}$ can be expressed in the following form:

$$\mathcal{A} = -2.5 \log\left(\frac{f_c + f}{F_c + f}\right) \tag{5.4}$$

where f is the sum of fluxes of all blending sources. From these two equations, one can write:

$$\mathcal{A} = 2.5 \log\left(\frac{10^{0.4\mathcal{A}^i} + \frac{f}{f_c}}{1 + \frac{f}{f_c}}\right) \tag{5.5}$$

Since $\mathcal{A}^i$ and f/f_c are always positive quantities, the observed amplitude of a blended Cepheid is always smaller than its intrinsic amplitude. The observed amplitude and the blended mean magnitude $< m >$ can be expressed as:

$$\mathcal{A} = m - M \tag{5.6}$$

$$< m >= \frac{m + M}{2} \tag{5.7}$$

where m and M are the observed magnitudes at minimum and maximum light of a Cepheid, respectively. In the same way, the intrinsic amplitude and the blending-free mean magnitude $< m^i >$ can be expressed as:

$$\mathcal{A}^i = m^i - M^i \tag{5.8}$$

$$< m^i >= \frac{m^i + M^i}{2} \tag{5.9}$$

From Eqs. (5.6)-(5.9) the difference on the mean magnitude of a given Cepheid as a consequence of blending can be expressed as:

$$\Delta =< m > - < m^i >= (m - m^i) - \frac{\mathcal{A} - \mathcal{A}^i}{2} \tag{5.10}$$

Considering that $(m - m^i)$ can be defined as:

$$m - m^i = -2.5 \log\left(\frac{f_c + f}{f_c}\right) = -2.5 \log\left(1 + \frac{f}{f_c}\right) \tag{5.11}$$

and isolating f/f_c from (5.5), the difference on the mean magnitude (5.10) can be expressed as:

$$\Delta = 2.5 \log\left(\frac{10^{0.2\mathcal{A}} - 10^{-0.2\mathcal{A}}}{10^{0.2\mathcal{A}^i} - 10^{-0.2\mathcal{A}^i}}\right) \tag{5.12}$$

Therefore, the variation on the mean magnitude of a given Cepheid because of blending can be computed from the amplitude of the Cepheid. Although $\mathcal{A}^i$ and Δ are unknown quantities, the above equation can be solved in combination with period-color and P-L relationships. The results shown below are based on the

Udalski et al. (1999) relationships, but almost identical results were obtained with other LMC relationships (Sandage et al., 2004).

The next step of the process involves recalling that $< m > \simeq \overline{m}$, where $\overline{m}$ is the phase-weighted intensity-average mean magnitude of the observed Cepheids. Therefore, defining the blending-free color excess as:

$$E(B^i - V^i) \equiv (B^i - V^i) - (B - V)_0 \tag{5.13}$$

the blended color excess can be expressed as:

$$E(B - V) = E(B^i - V^i) + \Delta_B - \Delta_V \tag{5.14}$$

where $\Delta_B = B - B^i$ and $\Delta_V = V - V^i$. Analogously, the distance modulus can be expressed as:

$$(V_0 - M_V) = (m - M)_0 + \Delta_V - \mathcal{R}_V(\Delta_B - \Delta_V) \tag{5.15}$$

where:

$$(V_0 - M_V) = V - \mathcal{R}_V E(B - V) - M_V \tag{5.16}$$

$$(m - M)_0 = V^i - \mathcal{R}_V E(B^i - V^i) - M_V \tag{5.17}$$

The combination of Eqs. (5.15) and (5.12) reveals that the value of $(V_0 - M_V)$ is only a function of the amplitude of the Cepheids and the distance modulus to M 31. In addition, the fact that the color excess is obtained from the observed color of the Cepheids (which is affected by blending) introduces the color term $(\Delta_B - \Delta_V)$ in Eq. (5.15). Therefore, and contrary to the intuitive interpretation, when reddening is computed from the observed color of Cepheids $(B - V)$ the blended distance modulus can be either larger or smaller than the intrinsic distance modulus $(m - M)_0$, depending on the values of $(\Delta_B - \Delta_V)$.

Considering that all Cepheids are roughly at the same distance, $(m - M)_0 = 24.44 \pm 0.12$ mag (Sect. 4.1.1.3), and assuming that $\mathcal{A}_V^i$ and $\mathcal{A}_B^i$ are linearly dependent (Fig. 5.5), Eq. (5.15) can be numerically solved. In fact, when the intrinsic amplitude of the Cepheid tends to zero, the observed amplitudes have to be zero in all passbands. Therefore, both amplitudes were considered to be proportional (i.e., $\mathcal{A}_B^i = \alpha \mathcal{A}_V^i$). The assumption that Cepheid amplitudes, when observed at different passbands, are proportional can be considered a first-order approximation of the Fourier coefficient interrelations (Ngeow et al., 2003).

Since the interrelations between B and V have not been accurately worked out, we computed the proportionality factor empirically from the observed amplitude of Cepheids. The amplitude of the studied Cepheids can be reliably estimated from the Fourier fits (Sect. 5.2). Therefore, the 240 FM Cepheids with accurate Fourier fits were used to compute the amplitude proportionality factor (Fig. 5.5), obtaining a mean value (with 2.5σ clipping) of $\mathcal{A}_B^i/\mathcal{A}_V^i \simeq \mathcal{A}_B/\mathcal{A}_V = 1.435 \pm 0.011$.

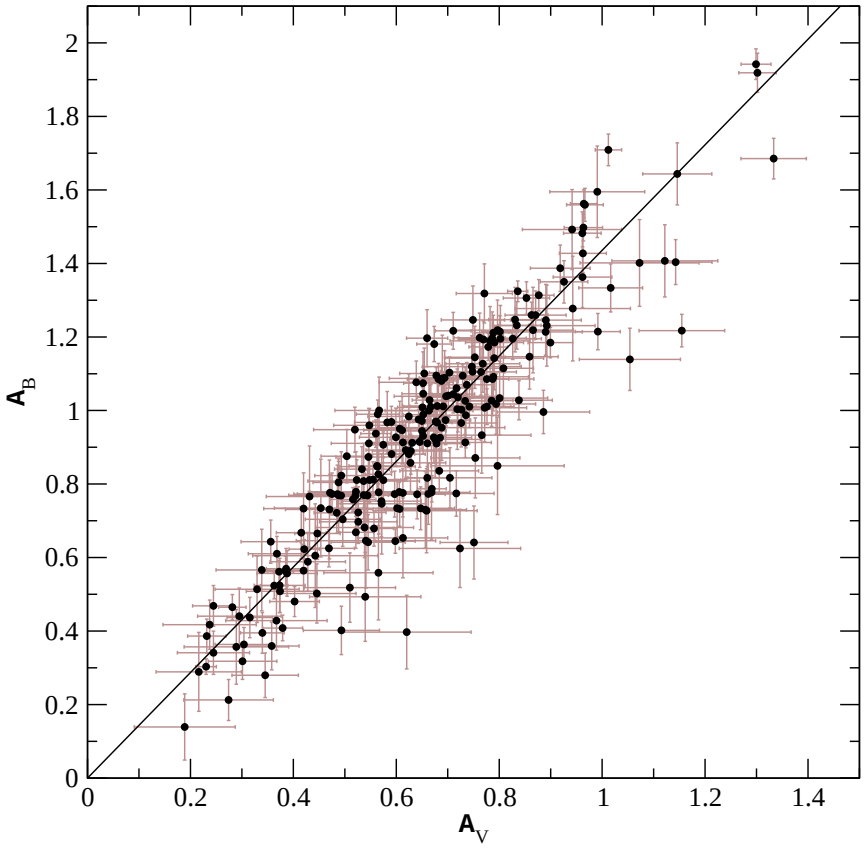

Figure 5.5. Amplitude relationship for the 240 fundamental mode Cepheids.

The above distance modulus to M 31 and the amplitude proportionality factor, when applied to Eq. (5.15), yielded the intrinsic amplitudes of the Cepheids. Once the intrinsic amplitudes are known, the difference on the mean magnitude can be computed (Fig. 5.6). The large resulting uncertainties in Δ_B and Δ_V clearly indicate that not much can be said from the individual blending of each Cepheid. The uncertainties were obtained from a MonteCarlo run with 1000 realizations on the input parameters of each Cepheid. The positive Δ values (implying negative blending) provide additional information on the associated uncertainties (probably of the order of 0.1-0.2 mag). In any case, it is interesting to observe that moderate intrinsic amplitudes are obtained for the entire sample, as it can be deduced from the lines of constant intrinsic amplitude in Fig. 5.6 (at $\Delta = 0$, $\mathcal{A} = \mathcal{A}^i$). Furthermore, the Cepheid with $\Delta_V > 1$ mag is the only suspected type II Cepheid with an accurate Fourier fit (see Fig. 5.4). The unrealistic blending value provides an additional evidence in favor of the type II classification.

Given the large number of studied Cepheids, the obtained blending values can also be used to determine a mean blending value for Cepheids in M 31. The results are shown in Table 5.1 where they are also compared with previous blending determinations in M 31 and M 33. The values labeled Sect. 2.4.1 were obtained

from the third light contribution in eclipsing binary systems, and the MMSS00 and MMSS04 values were obtained from comparison of Hubble Space Telescope (HST) and ground based images. The blending factors (S) presented in MMSS00 and MMSS04 were transformed into variation on the mean magnitude values by considering that:

$$\Delta = -2.5 \log\left(1 + \frac{f}{< f_c >}\right) \equiv -2.5 \log(1 + S) \tag{5.18}$$

where $< f_c >$ is the flux of the Cepheid at mean magnitude.

The observed difference with MMSS00 could be due to the assumed distance moduli or to the observing conditions. On the one hand, the reported uncertainties on the LMC and M 31 distance moduli could produce a variation of 0.12 mag in Δ_B and Δ_V. On the other hand, blending depends on seeing conditions and background level. Large seeing images increase the blending and high signal-to-noise data enables the detection of faint stars, decreasing the computed background and increasing the blending contribution. Considering that similar results have been obtained for the eclipsing binary sample (which comes from the same observational data but from a completely different procedure), the obtained differences with the values reported in MMSS00 could be the result of different observing conditions. The method used by MMSS00 can only provide lower limits to blending values, since the HST point spread function (used as a blending-free reference) could still hide unresolved companions. This is especially the case for the *B*-band results, where the available HST data was of low signal-to-noise ratio, thus implying that only the most severe blends were detected. In addition, the relatively small sample used by MMSS00 cannot be considered representative of the Cepheid population in M 31.

It is interesting to note that the results of MMSS04, based on a relatively large sample of Cepheids in M 33, have mean values similar to ours (although slightly different median values; Table 5.1). Such good agreement should be taken with caution as the host galaxies, the methods used, the period distributions of the samples, and therefore the associated systematic errors are different. Nevertheless, it is encouraging that estimates made using different methods in two somewhat differing spiral galaxies yield similar results.

To further analyze the effects of blending we have applied several cuts to the FM sample. It has traditionally been argued that the longer period (and brighter) Cepheids should be less affected by blending (Macri et al., 2006). We computed the mean blending for Cepheids with a period longer than 12 days and obtained, as expected, lower blending values (Table 5.1). Furthermore, considering that blending decreases the Cepheid amplitude, larger amplitude Cepheids should also be less affected by blending and, in fact, the 37 Cepheids with $\mathcal{A}_V > 0.8$ mag do have lower blending values (Table 5.1).

Finally, a blending-corrected color excess can be computed from Eq. (5.14),

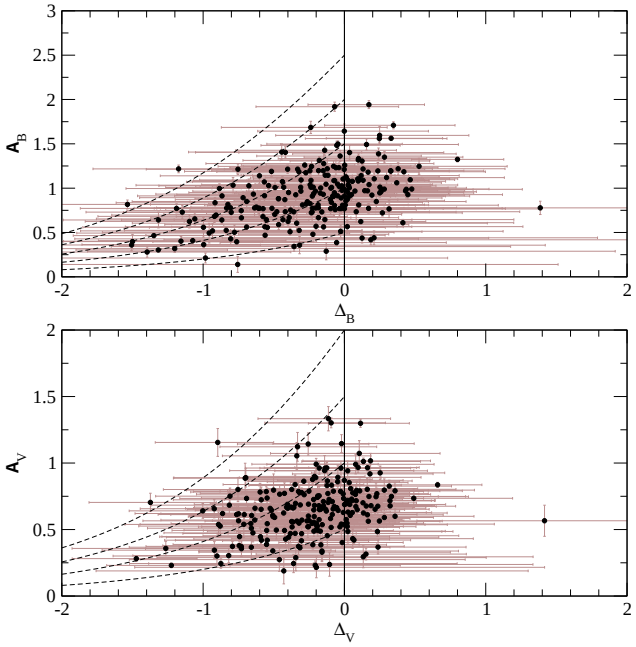

Figure 5.6. Observed amplitude of the 240 fundamental mode Cepheids with accurate Fourier fits as a function of the computed variation on the mean magnitude due to blending. Lines of constant intrinsic amplitude from 0.5 to 2 or 2.5 mag in steps of 0.5 mag are also shown (dashed lines).

Table 5.1. Blending values in M 31 and M 33 obtained from several methods. **Top:** Mean values and their errors. **Bottom:** Median values.

Reference	Sample	Number	$< S_V >$	$< S_B >$	$< \Delta_V >$ [mag]	$< \Delta_B >$ [mag]
MMSS00	Cepheids in M 31	22 (10 in *B*)	0.19 ± 0.03	0.06 ± 0.06	−0.18 ± 0.03	−0.05 ± 0.05
Present work	Eclipsing binaries	48	0.31 ± 0.07	0.30 ± 0.06	−0.23 ± 0.05	−0.25 ± 0.04
Present work	FM Cepheids	240	0.31 ± 0.03	0.37 ± 0.04	−0.23 ± 0.02	−0.24 ± 0.03
Present work	FM Cepheids with $P > 12$ days	37	0.14 ± 0.06	0.20 ± 0.10	−0.09 ± 0.05	−0.10 ± 0.07
Present work	FM Cepheids with $\mathcal{A}_V > 0.8$ mag	37	0.10 ± 0.05	0.11 ± 0.07	−0.06 ± 0.04	−0.05 ± 0.06
MMSS04	Cepheids in M 33	95 (57 in *B*)	0.24 ± 0.03	0.29 ± 0.06	−0.20 ± 0.02	−0.23 ± 0.04
MMSS04	Cepheids in M 33 with $P > 10$ days	60 (39 in *B*)	0.16 ± 0.04	0.20 ± 0.05	−0.14 ± 0.03	−0.17 ± 0.04
Reference	Sample	Number	Median(S_V)	Median(S_B)	Median(Δ_V) [mag]	Median(Δ_B) [mag]
MMSS00	Cepheids	22 (10 in *B*)	0.12	0.00	−0.12	0.00
Present work	Eclipsing binaries	48	0.09	0.16	−0.09	−0.16
Present work	FM Cepheids	240	0.20	0.15	−0.19	−0.16
Present work	FM Cepheids with $P > 12$ days	37	0.09	0.04	−0.09	−0.05
Present work	FM Cepheids with $\mathcal{A}_V > 0.8$ mag	37	0.09	0.04	−0.09	−0.05
MMSS04	Cepheids in M 33	95 (57 in *B*)	0.13	0.15	−0.13	−0.15
MMSS04	Cepheids in M 33 with $P > 10$ days	60 (39 in *B*)	0.07	0.10	−0.07	−0.10

obtaining a mean value of $< E(B^i - V^i) >= 0.305 \pm 0.011$. The blended mean color excess is slightly lower ($< E(B - V) >= 0.296 \pm 0.012$), indicating that blending sources are bluer than Cepheids. The difference is more significant when considering only Cepheids with large blending values ($\Delta_V < -0.5$ mag and $\Delta_B < -0.5$ mag), obtaining a blending-corrected color excess of $< E(B^i - V^i) >= 0.472 \pm 0.028$, whereas $< E(B - V) >= 0.315 \pm 0.030$. Therefore, considering the color-magnitude diagram (Fig. 2.12) and the distribution of Cepheids along the spiral arms, it is likely that early-type and young main sequence stars are responsible for the large measured blending. The obtained results are in good agreement with the results in MMSS04, who also found that M 33 blending sources were on average bluer than the Cepheids. To further check this scenario we used young MW open clusters to compute the light contribution that the main sequence stars would introduce on a Cepheid variable in the cluster. The resulting predictions on Δ_V and $\Delta_B - \Delta_V$ are in good agreement with the inferred blending values in M 31.

5.4 Distance determination

As previously mentioned, long period and large amplitude Cepheids are less affected by blends. Therefore, when computing the mean distance modulus to M 31, a systematic trend should be observed for increasing period and amplitude cuts (i.e., rejecting short period or low amplitude Cepheids). The $V_0 - M_V$ values obtained after the metallicity correction (Sect. 5.3.2) were used to compute weighted mean distance determinations to M 31 (with 2.5σ clipping). The resulting values assume a distance modulus to the LMC of $(m - M)_0 = 18.42 \pm 0.06$ mag (Table 1.3). The amplitudes for the 41 FM Cepheids without accurate Fourier fits were computed from the observations and were also included in order to obtain a better coverage in periods and amplitudes.

Figure 5.7 shows that the distance modulus increases as the minimum period or minimum amplitude cuts increase. We observe that the distance modulus value stabilizes for $\mathcal{A}_V > 0.8$ mag. The most likely cause for the observed trend is that blending is lower than photometric errors (or even zero) for large amplitudes. The most suitable period cut is more difficult to compute, although an increasing trend is also observed. The observed behavior is explained if long period Cepheids are still affected by large blends, thus still introducing a bias in the derived distance modulus. Hence, an amplitude cut is the best choice to derive the distance to M 31 from the studied Cepheid sample. From this analysis (Fig. 5.7), the 66 Cepheids with amplitude $\mathcal{A}_V > 0.8$ mag seem to represent the best sample for distance determination.

The effect of removing small amplitude Cepheids is clearly visible in Fig. 5.8, where the P-L diagram for the largest amplitude Cepheids is shown. Two stars with $\mathcal{A}_V > 0.8$ mag are placed far below the general P-L distribution (empty

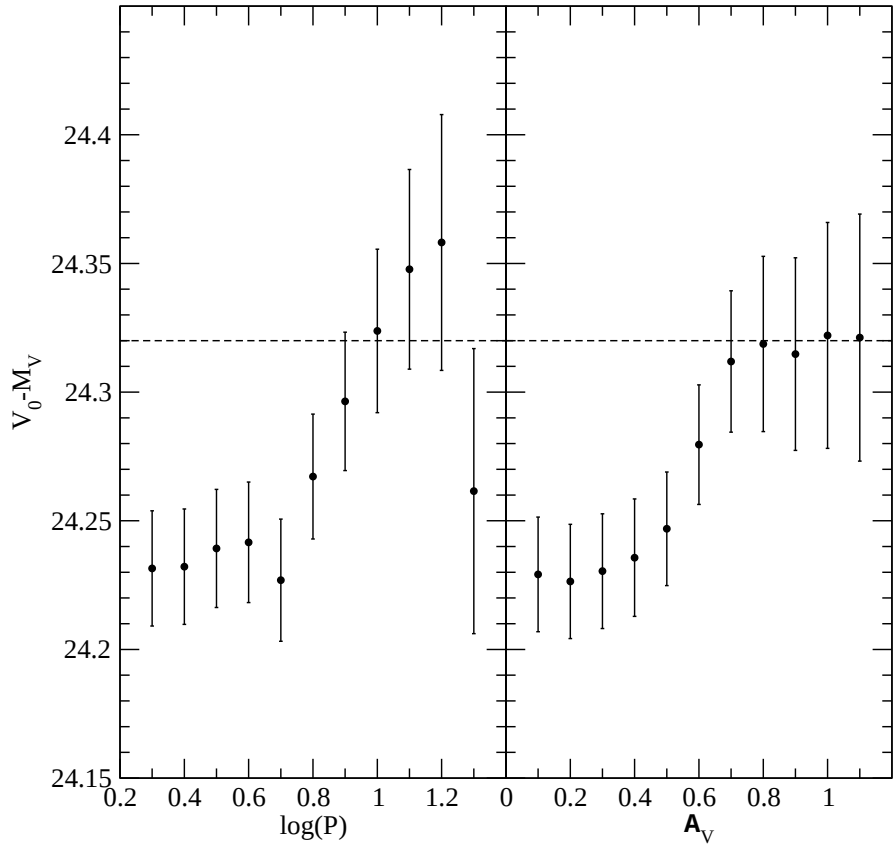

Figure 5.7. Weighted mean $V_0 - M_V$ values for the 281 fundamental mode Cepheids in M 31 for different cuts. Error bars indicate the error on the mean. The dashed line represents the adopted distance determination of $(m - M)_0 = 24.32 \pm 0.12$ mag. **Left:** each distance determination includes all Cepheids with period longer than the specified value. **Right:** each distance determination includes all Cepheids with amplitude larger than the specified value.

circles in Fig. 5.8). Both stars are on the type II Cepheids relationships, reinforcing the hypothesis that these stars are, in fact, type II Cepheids and they have not been considered from now on. Finally, the obtained P-L slope, with a value of -2.83 ± 0.12 mag dex^{-1}, is closer to the Udalski et al. (1999) LMC value of -2.779 ± 0.031 mag dex^{-1} than to MW P-L slopes (e.g.: -3.087 ± 0.085 mag dex^{-1}, Sandage et al., 2004), therefore favoring the adopted P-L relationships.

From the considerations above, the M 31 distance modulus obtained from the studied sample of Cepheids is $(m - M)_0 \simeq (V_0 - M_V)_{\mathcal{A}>0.8} = 24.32 \pm 0.12$ mag. This value is compatible with most distance determinations found in the literature (Table 1.1) and with EB distance determinations of Sect. 4.2 (one of which was used to assume the distance modulus in Sect. 5.3.3). Considering that some large amplitude Cepheids may still be affected by blends, the distance modulus we derive could have a slight negative bias. Note that our final value is 0.09

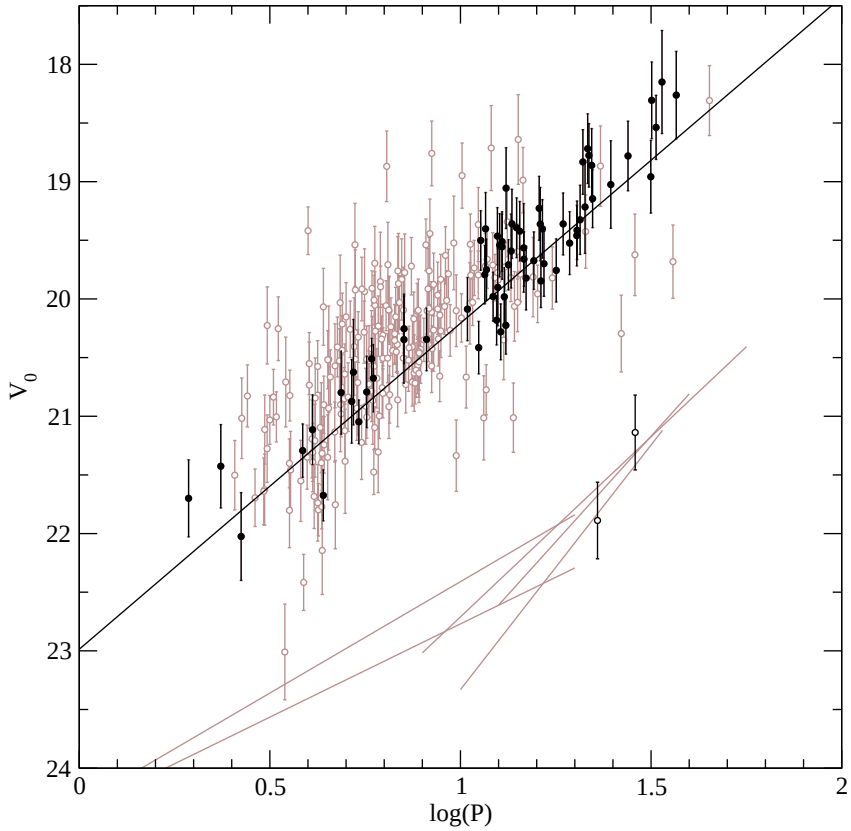

Figure 5.8. Absorption-corrected V magnitude as a function of period for 281 fundamental mode Cepheids. Empty gray circles: complete fundamental mode sample. Filled black circles: Cepheids with $\mathcal{A}_V > 0.8$ mag. Empty black circles: two stars with $\mathcal{A}_V > 0.8$ mag excluded from the distance determination. Black line: Udalski et al. (1999) P-L relationship, for a distance modulus to M 31 of 24.44 (Sect. 4.1.1.3) and a mean metallicity correction of −0.1 mag (Sect. 5.3.2). Gray lines: P-L relationships for type II Cepheids as given by Alcock et al. (1998) at distance of M 31.

mag larger than the weighted mean distance modulus for the 281 FM Cepheids ($(V_0 - M_V) = 24.23 \pm 0.12$ mag). Therefore, blending is clearly an important effect that has to be considered when obtaining extragalactic distance determinations. In fact, blending has nearly the same impact on the final distance determination for M 31 as the metallicity correction.

6 The distance to M 31 and final remarks

During the course of the present work, several distance determinations to M 31 have been obtained. In order to study the relationship between the derived distances and to place the derived values in context, a brief discussion is required (Sect. 6.1). Once the final distance is derived and placed in context, the results derived in the present work are summarized (Sect. 6.2) together with some comments on future investigation lines that could help to improve the presented results (Sect. 6.3).

6.1 The distance to M 31

From the results given in Sect. 4.2, it is obvious that the main goal of the present work (a direct and accurate distance determination to M 31 from EBs) has been fulfilled. The derived distance modulus of $(m - M)_0 = 24.36 \pm 0.08$ mag relies on the modeling of two different EBs and, therefore, can be considered to be:

- *Direct*. The distance determination from EBs does not rely on previous calibrations and, since it is derived using a one-step procedure, it can be considered direct. Therefore, a posterior recalibration of the distance to other Local Group galaxies (such as LMC) or a variation on the zero-point of any standard candle (such as Cepheids) has no effect on the derived distance. Furthermore, any standard candle in M 31 can be calibrated using our derived distance.

- *Accurate*. One of the most important points when determining distances is the effect of possible systematics in the derived value. Contrary to other distance determinations, the uncertainty in our distance modulus includes most, if not all, the possible systematics. In particular, the possible sources

of systematic errors, and the corresponding considerations, can be summarized in the following points:

- Photometry. The photometry has been compared with other catalogs (Sect. 2.3.1) and checked to be well below 0.03 mag for the magnitude of the selected EBs.
- Assumed configuration in the modeling of the EBs. The configuration assumed is completely independent for each one of the two EBs used for distance determination and result in distances that agree within the uncertainties. In addition, SB2A has clear evidences of being a post-mass-transfer EB (O'Connell effect, no eccentricity, secondary apparently more evolved, etc.) and SB2B has been thoroughly tested for any other possible configuration, with none of them being capable to reproduce the observations.
- Radial velocities. Several aspects have been considered with respect to the radial velocity determinations. TODCOR is a well tested program that has been checked to introduce some systematics only for spectra with a short wavelength coverage (Torres & Ribas, 2002), which is not our case. In addition, the possible systematics introduced by the use of Balmer lines (that can be affected by stellar winds) is compensated with the incorporation of He lines. In addition, the stellar wind would introduce a bias mainly in the systemic velocity, which has no impact in the final distance determination.
- Stellar atmosphere models used to determine the surface flux. This is probably the major source of systematic errors, since it is based on several calibrations. However, the models used are thoroughly tested in several branches of astronomy. In addition, the derived fluxes are compatible with the HST spectrophotometry at optical wavelengths. Therefore, any possible systematics are expected to be well below 0.05 mag.
- Line-of-sight absorption. As seen in the spectrophotometry, the ultraviolet part of the mean galactic extinction curve is unable to reproduce the observed values. However, the only effect in the determination of the absorption at optical wavelengths would be a variation in the determination of $\mathcal{R}_V$. The value of $\mathcal{R}_V$ has already been considered to have an uncertainty of 10% and larger variations are unlikely, as seen from previous statistical analysis (Fitzpatrick & Massa, 2007).

- *Precise*. The uncertainty on the derived distance modulus of 0.08 mag represents a distance determination with an error of only 4%. Although several of the values reported in Table 1.1 have smaller errors, most of these results do not consider the effect of systematics. In fact, the derived uncertainty is equal to the standard deviation resulting from the combination of all the

non-direct distance determinations in Table 1.1 and, therefore, our derived distance is equally precise.

Therefore, EBs have proven to be excellent distance markers and, arguably, the best method to provide direct distances for all the galaxies in the Local Group.

The uncertainty in the derived distance could be improved with the analysis of additional EBs (already identified in the list of 24 EBs provided in Sect. 2.4.1), resulting in a distance determination to M31 with a relative uncertainty of 2–3% and free of most systematic errors. This result would represent the most accurate and reliable distance determination to this important Local Group galaxy. In addition, a better determination of the line-of-sight absorption could also improve the uncertainty in the distance determination. In this sense, observations (already performed) with GALEX (Thilker et al., 2005) and Spitzer (Mould et al., 2008) could help to determine the spectral energy distribution of the observed EBs and, therefore, to better constrain the absorption.

The derived distance modulus is in complete agreement with the mean value in Table 1.1 (Fig. 6.1). In fact, *all* the 18 distances reported in Table 1.1 agree with the EB value within 2σ and prove that the different distance indicators are all rather well calibrated within their error bars. In addition, the large number of distance indicators observed in M 31 strengthens the importance of this galaxy as the main calibrator for extragalactic distance determinations. In fact, all the distance indicators used to determine a distance to LMC (Gibson, 2000), can be used, in principle, in M 31. In addition, at least two other distance determination methods can be used in M 31 (planetary nebulae luminosity function and Tully-Fisher relationship). Therefore, after the direct distance obtained with EBs, M 31 may be the best extragalactic benchmark for distance determinations.

Cepheids have also been used to determine a distance to M 31 (Sect. 5.4). The derived distance modulus of $(m - M)_0 = 24.32 \pm 0.12$ mag represents an additional distance determination to M 31 that is fully compatible with the EB value. The consistent result with EBs proves that the Cepheid analysis performed, including the period-luminosity relationship, metallicity correction and blending, is correct (within the uncertainties). The consistency of the results is specially valuable, because the EB distance to LMC has been used as reference. Therefore, the Cepheid distance modulus proves that the EB distances to LMC and to M 31 are fully compatible, tightening the extragalactic distance scale.

In fact, Cepheids have proven to be extremely useful and robust to determine *relative* distances among galaxies. Macri et al. (2006) used the Cepheids in NGC 4258, which has a direct maser-based distance (Herrnstein et al., 1999), to determine a distance modulus to LMC that is almost identical to the EB value. Therefore, the derived distances using EBs are not only fully compatible among themselves, but also to other direct distance determination methods.

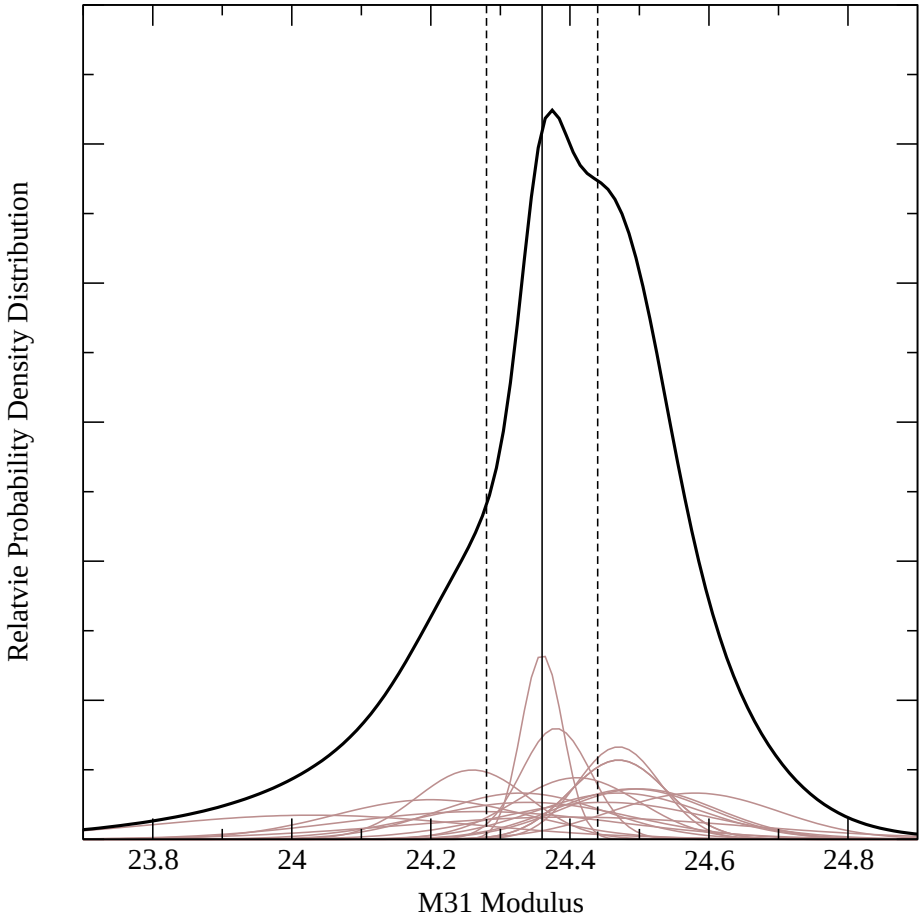

Figure 6.1. Distribution of M 31 distance moduli as compiled in Table 1.1 plotted as a continuous probability density distribution (black line) built from the sum of individual unit-area Gaussians centered at the quoted modulus, and broadened by the published internal random error (gray lines). Distance to M 31 derived after the present work is shown (straight black line) together with its 1σ error bars (dashed lines).

6.2 Summary of the results

The main results of this work are summarized here to enable a quick look. For any additional information in a specific topic, see the corresponding section.

6.2.1 Data acquisition, reduction and analysis

As the very first step in the determination of a distance to M 31, deep and high-quality time-series photometry was obtained. A region (of $33\farcm8 \times 33\farcm8$) in the north-eastern quadrant of M 31 was observed during five years in B and V with

the WFC at INT. Two main factors place the present survey among the best variability surveys obtained so far in M 31. On one hand, the implementation of the image subtraction technique has allowed the acquisition of highly precise photometry ($\sim$ 0.01 mag at $V \sim 19$ mag) of 3 964 variable stars, with 437 EBs and 416 Cepheids. This technique is representing a revolution in the search for extragalactic variable stars, where crowding is a major concern, being also implemented with great success in other surveys as OGLE (Udalski et al., 2008) or DIRECT (Mochejska et al., 2001b). On the other hand, the great number of observations ($\sim$ 250 per passband) has enabled an almost complete coverage of the light curves of all the variables with periods shorter than five days.

In addition to the photometry of variable stars, photometry of all the detected stars in the field of view (236 238) was also obtained. The resulting photometry is both precise (with 37 241 objects having errors below 0.1 mag in B and V) and accurate, since it has been checked for compatibility with other surveys, such as LGGS (Massey et al., 2006) and DIRECT (Macri, 2004). The comparison has revealed that any possible systematics larger than 0.03 mag for the brightest stars can be ruled out. In addition, it is one of the deepest photometric surveys obtained in the disk of M 31 (with magnitude limits at $V \simeq 25.5$ and $B \simeq 26.0$). Therefore, our resulting catalog can be used as a reference to extend the time baseline of future stellar surveys in M 31.

Apart from the already identified population, there are over 3 000 variable stars still pending for an identification. The obtained catalog can contain any type of variable stars (Miras, LBVs, etc.). In fact, one of the variable stars (M31V J00441943+4122468) is a well known LBV (V15, King et al., 1998). Therefore, the obtained catalog represents an important database for future studies in M 31. The great potential of the obtained catalog to analyze additional variable stars has been revealed by the discovery of a dM4 flaring star in the Milky Way (Appendix A). Therefore, further analysis on the already obtained data could reveal other interesting objects in M 31 and in our own galaxy.

Another requirement to derive a distance determination to M 31 with EBs is the acquisition of spectroscopy. The EB sample was inspected in order to identify those systems that were more suitable for accurately determining the components' physical properties. A list of 24 EBs was selected to be the best candidates for spectroscopic follow up and multi-object spectroscopy was obtained for five of them. The observed sample is only a small fraction of the total number of selected EBs. Therefore, the list provided constitutes an excellent masterlist from which to select EB systems for further observations.

The nine acquired spectra with GMOS at Gemini-North have a resolution of $\sim$ 80 km s^{-1}, cover the wavelength interval of $\sim$ 380 nm to $\sim$ 530 nm (with most of the Balmer lines) and have a S/N ranging from 5 to 40. EBs have a major drawback when obtaining radial velocities, since their relatively short orbital periods preclude the use of long exposure times, thus limiting the S/N. However,

the techniques used in the course of the present work (with the implementation of TODCOR, TIRAVEL, TRIMOR and KOREL) have enabled the determination of radial velocities, even for low S/N spectra. In addition to the acquisition of radial velocities, the techniques used have enabled the disentangling and the combination of the observed spectra to produce a higher S/N spectrum. The great similarities of the obtained spectra with synthetic counterparts reveal that spectral disentangling is capable to provide accurate fundamental properties for the individual components of EB systems even for low S/N spectra. Therefore, the techniques applied during the course of the present work clearly reveal that fundamental properties of EB systems in Local Group galaxies can be obtained with current facilities.

Finally, the obtained spectrophotometry (with ACS at HST) has revealed that current instrumentation has to be improved in order to derive precise spectrophotometry for stars in M 31. This instrumentation existed in the past (i.e., STIS and FOS), but the current state of HST has reduced the capability to obtain precise spectrophotometry of faint stars. Hopefully, the situation will change in the near future, with the Service Mission 4 to HST in 2009 and the launch of the World Space Observatory/Ultraviolet in few years. These two space missions should provide new instrumentation in the ultraviolet to the scientific community, which should enable the acquisition of precise spectrophotometry of faint stars and, thus, allow the use of the spectrophotometric method for EBs in M 31 (and other galaxies in the Local Group).

6.2.2 Properties of eclipsing binaries

The determination of the fundamental properties of bright stars in other galaxies has revealed to be a valuable source for identifying massive stars (e.g., Bonanos et al., 2004). The comparison of the color-magnitude diagrams of EBs (Fig. 2.10) and Cepheids (Fig. 2.12) has revealed that the EB population observed is much bluer ($< B-V >= 0.1 \pm 0.5$) than the Cepheid population ($< B-V >= 0.9 \pm 0.3$). Considering the mean blending-free color excess derived of $< E(B-V) >= 0.305 \pm 0.011$ (Sect. 5.3.3), the reddening-free mean color of the EB population is $< B-V >= -0.2 \pm 0.5$. Therefore, most of the reported EB systems are composed by blue and massive main sequence components.

EBs are excellent tools to determine fundamental properties of massive stars in M 31 and other Local Group galaxies. Direct determinations of masses and radii for massive stars in the Milky Way are more difficult due to absorption. Therefore, extragalactic determinations of masses and radii (like the ones performed in the present work) will greatly help in determining the fundamental properties of the most massive stars. The analysis of four EBs in Chap. 4 (with two double-line, one single-line and one triple-line EB) has revealed a whole zoo of different massive stars, all of them being extremely interesting to better understand the physics of

these stars.

The modeling of the double-line EBs has provided masses and radii with relative uncertainties below 10% and around 5%, respectively, which is remarkable given the faintness of the stars. Although both systems have similar components (with masses around 22 $M_\odot$ and 15 $M_\odot$), the evolutionary stage of each EB is largely different. SB2A (M31V J00443799+4129236) is a semi-detached EB with active mass transfer, where the originally more massive component is now observed as the secondary. The observed O'Connell effect in SB2A can well be used, in the future, to infer the mass transfer rate in such a massive binary system. SB2B (M31V J00443610+4129194), on the contrary, is a pre-mass-transfer EB (with an age of about 4.2 Myr), where the more massive component is about to fill its Roche lobe. This evolutionary stage is not commonly observed in massive EBs, due to the short time spent at this stage. Therefore, both systems have characteristics that make them interesting cases of close EBs, enabling futures studies of mass transfer and the effects of proximity on the evolution of massive stars.

In the case of the single-line EB (M31V J00444528+4128000, SB1), two evolved and massive components (of ∼26 $M_\odot$ and ∼14 $M_\odot$) have been observed. The analysis performed has revealed that the primary component is a blue supergiant in a semi-detached configuration. This system can be useful to study the mass transfer of massive stars during the helium burning phase.

Another interesting target is the triple-line EB (M31V J00442326+4127082, SB3). This target is composed by two extremely massive stars (49 $M_\odot$ and 46 $M_\odot$) with an age of 2.3 Myr. The measured apsidal motion of $\dot{\omega} = 2.4 \pm 1.0$ deg year^{-1} identifies this system as the most massive EB with apsidal motion ever reported. The analysis performed so far has revealed the great value of this EB to study and verify the stellar interior models for stars with convective core. Further analysis of the obtained data should help to verify whether the observed stars have convective envelopes larger than those predicted by stellar models. In this sense, since the photometric survey ended in 2003, current observations of SB3 would already be able to greatly improve the apsidal motion rate determination.

The obtained results open the field of detailed investigations of stellar evolutionary models for massive stars (single and binary) in another galaxy and, hence, in a completely independent chemical environment. It is important to remind that only four of a list of 24 massive EBs have been analyzed. The analysis of additional EBs in the list could provide an excellent workbench where to test stellar structure and evolutionary models. However, the analysis of the reported sample involves the acquisition of spectra with large telescopes (8–10 m) having spectroscopic instrumentation in the optical. Currently, one of the only telescopes with such facilities in the northern hemisphere is Gemini-North. Fortunately, Gran Telescopio de Canarias (GTC) has just started operations with OSIRIS, an instrument that could well be suitable for this study when the proper gratings are available.

6.2.3 Properties of Cepheids

The large number of detected Cepheids (416) motivated a comprehensive analysis of the Cepheid population in M 31. Having the same number of Cepheids that the General Catalog of Variable Stars, our catalog is much deeper, being almost as complete as the David Dunlap Observatory Milky Way sample. Both period distributions have a double-peak structure, with a dip at around 10 days. The only difference may be the lack of long period (and bright) Cepheids in our catalog.

In addition, the large number of epochs obtained (~ 250) in both filters (B and V) has permitted the accurate pulsation mode identification of 240 fundamental mode (FM) and 75 first overtone (FO) Cepheids. The sample of FM Cepheids was completed with 41 long period (i.e., longer than 8 days) Cepheid variables, resulting in a total amount of 281 FM Cepheids. The subsequent analysis of this sample revealed that at least three of these stars are, in fact, type II Cepheids. Regarding FO pulsators, although some FO Cepheids were previously detected in M 31 (Fliri et al., 2006), our sample yields an important increase in the number of detected FO pulsators and opens a new window to study the basic properties of these stars in another Local Group galaxy.

The analysis of the P-L relationship for the FM Cepheids reveals a large scatter, which is not explained solely through the effects of interstellar absorption and metallicity. Although additional efforts are needed to reduce the obtained uncertainties, a new method to compute the effect of blending was developed. The exact dependence of the amplitudes among different passbands, as well as more precise amplitude determinations, would greatly enlarge the results shown here. The uncertainties could also be reduced by acquiring time series photometry at longer wavelength (such at I band or at the infrared).

Even by considering the large uncertainties, the large number of studied Cepheids provides an accurate characterization of the mean blending values, which are in good agreement with those derived by Mochejska et al. (2000, 2004) in M 31 and M33. We conclude that the most likely cause of blending seems to be the light from unresolved stars belonging to the same stellar associations or clusters as Cepheid variables.

The effect of blending has also been shown to be larger than 0.09 mag in the distance modulus to M 31, thus having an effect as important as the metallicity correction. Therefore, blending should always be taken into account when obtaining extragalactic distance determinations with Cepheids.

6.2.4 Distance determinations

Four distance determinations to M 31 have been presented in the course this work. Of these, two are direct distance determinations with EBs, deriving distance mod-

uli of $(m-M)_0 = 24.44 \pm 0.12$ mag and $(m-M)_0 = 24.30 \pm 0.11$ mag. These values have been averaged to derive a robust distance modulus to M 31 of $(m - M)_0 = 24.36 \pm 0.08$ mag, firmly establishing the distance to this important galaxy. Another EB has been shown to provide a distance determination to M 31 of $(m - M)_0 = 24.8 \pm 0.6$ mag. This value cannot be considered a direct distance determination because stellar evolution models were used. The derived distance, however, represents a useful cross-check to ensure that the properties derived for this binary, composed of extremely massive stars, are consistent. Finally, the Cepheids identified in the photometric catalog have provided a distance to M 31 of $(m - M)_0 = 24.32 \pm 0.12$ mag. The derived value is fully compatible with the EB distance determinations, providing an additional check on the derived results.

6.3 Future work

As the last step in the present work, some comments are made on how to improve the derived results. Most of them have already been mentioned somewhere else in the course of the present work. Even though, they are placed together here for reference.

The extensive data analysis performed in the course of the present work has provided a wealth of data acquired with leading observational facilities. Our investigation was centered on acquiring the necessary information to derive a distance to M 31, setting apart any additional information. Therefore, the obtained data can be an excellent starting point for future work.

One of the potential sources for future analysis is the photometric catalog of variable stars (Sect. 2.3.2). Of the derived sample of 3 964 variable stars, there are over 3 000 sources still pending to be identified. The possible sources in the compiled catalog are numerous, and range from luminous blue variables (M31V J00441943+4122468) to flaring stars in the Milky Way (see Appendix A) with, probably, several long period variables (like Miras).

Another source for future work is the list of 24 EB selected as suitable candidates for distance determination (Sect. 2.4.1). Four EBs have been analyzed in the course of the present work. Therefore, there are still 20s EB waiting for spectroscopic observations. The future analysis of the sample can result in a distance determination to M 31 with a relative uncertainty of 2–3% and free of most systematic errors.

In addition to the distance determination, the analysis of the EB sample would provide an excellent benchmark where to test stellar structure and evolutionary models. In particular, the EB sample could be used to determine internal structure constants through the apsidal motion (e.g., SB3 in Sect. 4.1.4), to study the mass transfer in semi-detached systems (e.g., with SB2A in Sect. 4.1.1) or, since the

radii of stars can be directly determined, to study the wind momentum-luminosity relationship for massive stars (see Kudritzki & Puls, 2000, for a review).

Apart from EBs, the present study has shown that accurate photometry for Cepheids in M 31 can be obtained. A program to obtain high quality light curves in whole disk of M 31 would be of great interest. The presented work has revealed hundreds of Cepheids in a region that is about one third of the M 31 disk. Therefore a specially aimed survey (with *I* photometry) could reveal several thousands of Cepheids in this galaxy. In fact, the determination of the global properties of Cepheids (such as the period distribution or the dependence on metallicity) could be much more easy to study in M 31 than in our own galaxy.

Another interesting project would be the analysis of blending in other Local Group galaxies (and beyond) using the method presented in this work. The method needs high accuracy light curves ($\sim 0.01 - 0.02$ mag) with a large number of epochs (~ 100). The only galaxies currently having these light curves are LMC, SMC, the Milky Way and M 31. All the galaxies quoted (except M 31) are expected to have low blending values. Considering that blending can be as important as metallicity correction for the final distance determination with Cepheids, further investigations in other Local Group galaxies would be extremely valuable.

Bibliography

Alard, C. & Lupton, R. H. 1998, ApJ, 503, 325

Alcock, C., Allsman, R. A., Alves, D. R., et al. 1998, AJ, 115, 1921

Antonello, E. 2002, A&A, 391, 795

Antonello, E., Fugazza, D., & Mantegazza, L. 2002, A&A, 388, 477

Antonello, E., Poretti, E., & Reduzzi, L. 1990, A&A, 236, 138

Attrill, G. D. R., Harra, L. K., van Driel-Gesztelyi, L., & Démoulin, P. 2007, ApJ, 656, L101

Baade, W. & Arp, H. 1964, ApJ, 139, 1027

Baade, W. & Swope, H. H. 1963, AJ, 68, 435

Baade, W. & Swope, H. H. 1965, AJ, 70, 212

Baraffe, I. & Chabrier, G. 1996, ApJ, 461, L51

Baraffe, I., Chabrier, G., Allard, F., & Hauschildt, P. H. 1998, A&A, 337, 403

Barnes, T. G. & Evans, D. S. 1976, MNRAS, 174, 489

Beaulieu, J. P., Grison, P., Tobin, W., et al. 1995, A&A, 303, 137

Becker, S. A., Iben, I., & Tuggle, R. S. 1977, ApJ, 218, 633

Benedict, G. F., McArthur, B. E., Feast, M. W., et al. 2007, AJ, 133, 1810

Bertin, E. & Arnouts, S. 1996, A&AS, 117, 393

Bessell, M. S., Castelli, F., & Plez, B. 1998, A&A, 333, 231

Bonanos, A. Z. & Stanek, K. Z. 2003, ApJ, 591, L111

Bonanos, A. Z., Stanek, K. Z., Kudritzki, R. P., et al. 2006, ApJ, 652, 313

Bonanos, A. Z., Stanek, K. Z., Sasselov, D. D., et al. 2003, AJ, 126, 175

Bonanos, A. Z., Stanek, K. Z., Udalski, A., et al. 2004, ApJ, 611, L33

Bresolin, F., Pietrzyński, G., Gieren, W., & Kudritzki, R.-P. 2005, ApJ, 634, 1020

Brewer, J. P., Richer, H. B., & Crabtree, D. R. 1995, AJ, 109, 2480

Brown, T. M., Ferguson, H. C., Smith, E., et al. 2004, AJ, 127, 2738

Capaccioli, M., della Valle, M., Rosino, L., & D'Onofrio, M. 1989, AJ, 97, 1622

Claret, A. 2004, A&A, 424, 919

Claret, A. & Gimenez, A. 1993, A&A, 277, 487

Clausen, J. V. 2004, New Astronomy Review, 48, 679

Clementini, G., Federici, L., Corsi, C., et al. 2001, ApJ, 559, L109

Cotton, W. D., Condon, J. J., & Arbizzani, E. 1999, ApJS, 125, 409

Davidge, T. J. & Milone, E. F. 1984, ApJS, 55, 571

Drimmel, R., Cabrera-Lavers, A., & López-Corredoira, M. 2003, A&A, 409, 205

Durrell, P. R., Harris, W. E., & Pritchet, C. J. 2001, AJ, 121, 2557

Feast, M. 1999, PASP, 111, 775

Feast, M. W. & Catchpole, R. M. 1997, MNRAS, 286, L1

Fernie, J. D., Evans, N. R., Beattie, B., & Seager, S. 1995, Informational Bulletin on Variable Stars, 4148, 1

Fitzpatrick, E. L. 1999, PASP, 111, 63

Fitzpatrick, E. L. & Massa, D. 2005, AJ, 129, 1642

Fitzpatrick, E. L. & Massa, D. 2007, ApJ, 663, 320

Fitzpatrick, E. L., Ribas, I., Guinan, E. F., et al. 2002, ApJ, 564, 260

Fitzpatrick, E. L., Ribas, I., Guinan, E. F., Maloney, F. P., & Claret, A. 2003, ApJ, 587, 685

Fliri, J., Riffeser, A., Seitz, S., & Bender, R. 2006, A&A, 445, 423

Freedman, W. L. & Madore, B. F. 1990, ApJ, 365, 186

Freedman, W. L., Madore, B. F., Gibson, B. K., et al. 2001, ApJ, 553, 47

Gautschy, A. & Saio, H. 1996, ARA&A, 34, 551

Gibson, B. K. 2000, Memorie della Societa Astronomica Italiana, 71, 693

Gibson, B. K., Maloney, P. R., & Sakai, S. 2000, ApJ, 530, L5

Gieren, W., Storm, J., Barnes, III, T. G., et al. 2005, ApJ, 627, 224

Gieren, W. P., Fouque, P., & Gomez, M. I. 1997, ApJ, 488, 74

Giménez, A., Clausen, J. V., Guinan, E. F., et al. 1994, Experimental Astronomy, 5, 181

Gordon, K. D., Bailin, J., Engelbracht, C. W., et al. 2006, ApJ, 638, L87

Guinan, E. F. 1993, in Astronomical Society of the Pacific Conference Series, Vol. 38, New Frontiers in Binary Star Research, ed. K.-C. Leung & I.-S. Nha, 1

Guinan, E. F., Fitzpatrick, E. L., Dewarf, L. E., et al. 1998, ApJ, 509, L21

Guinan, E. F. & Maloney, F. P. 1985, AJ, 90, 1519

Guinan, E. F., Ribas, I., Fitzpatrick, E. L., et al. 2000, ApJ, 544, 409

Hadrava, P. 1995, A&AS, 114, 393

Harries, T. J., Hilditch, R. W., & Howarth, I. D. 2003, MNRAS, 339, 157

Herrnstein, J. R., Moran, J. M., Greenhill, L. J., et al. 1999, Nature, 400, 539

Hilditch, R. W. 2001, An Introduction to Close Binary Stars (Cambridge, UK: Cambridge University Press)

Hodge, P. W. 1981, ARA&A, 19, 357

Holland, S. 1998, AJ, 115, 1916

Hubble, E. P. 1929, ApJ, 69, 103

Hudson, H. S., Wolfson, C. J., & Metcalf, T. R. 2006, Sol. Phys., 234, 79

Ishida, K. 1990, in IAU Symposium, Vol. 137, Flare Stars in Star Clusters, Associations and the Solar Vicinity, ed. L. V. Mirzoian, B. R. Pettersen, & M. K. Tsvetkov, 43

Ishida, K., Ichimura, K., Shimizu, Y., & Mahasenaputra. 1991, Ap&SS, 182, 227

Jacoby, G. H., Branch, D., Ciardullo, R., et al. 1992, PASP, 104, 599

Joshi, Y. C., Pandey, A. K., Narasimha, D., Sagar, R., & Giraud-Héraud, Y. 2003, A&A, 402, 113

Kaluzny, J., Stanek, K. Z., Krockenberger, M., et al. 1998, AJ, 115, 1016

King, N. L., Walterbos, R. A. M., & Braun, R. 1998, ApJ, 507, 210

Kovári, Z., Vilardell, F., Ribas, I., et al. 2007, Astronomische Nachrichten, 328, 904

Kudritzki, R.-P. & Puls, J. 2000, ARA&A, 38, 613

Lacy, C. H. 1977, ApJ, 213, 458

Lacy, C. H., Moffett, T. J., & Evans, D. S. 1976, ApJS, 30, 85

Lamers, H. J. G. L. M. & Fitzpatrick, E. L. 1988, ApJ, 324, 279

Landolt, A. U. 1992, AJ, 104, 340

Lanz, T. & Hubeny, I. 2003, ApJS, 146, 417

Lanz, T. & Hubeny, I. 2007, ApJS, 169, 83

Leavitt, H. S. & Pickering, E. C. 1912, Harvard College Observatory Circular, 173, 1

Lejeune, T. & Schaerer, D. 2001, A&A, 366, 538

Lin, R. P., Schwartz, R. A., Kane, S. R., Pelling, R. M., & Hurley, K. C. 1984, ApJ, 283, 421

Luri, X., Gomez, A. E., Torra, J., Figueras, F., & Mennessier, M. O. 1998, A&A, 335, L81

Macri, L. M. 2004, in ASP Conf. Ser. 310: IAU Colloq. 193: Variable Stars in the Local Group, 33

Macri, L. M., Stanek, K. Z., Bersier, D., Greenhill, L. J., & Reid, M. J. 2006, ApJ, 652, 1133

Massey, P. 2003, ARA&A, 41, 15

Massey, P., Armandroff, T. E., Pyke, R., Patel, K., & Wilson, C. D. 1995, AJ, 110, 2715

Massey, P., Olsen, K. A. G., Hodge, P. W., et al. 2006, AJ, 131, 2478

McConnachie, A. W., Irwin, M. J., Ferguson, A. M. N., et al. 2005, MNRAS, 356, 979

Michalska, G. & Pigulski, A. 2005, A&A, 434, 89

Mochejska, B. J., Kaluzny, J., Stanek, K. Z., & Sasselov, D. D. 2001a, AJ, 122, 1383

Mochejska, B. J., Kaluzny, J., Stanek, K. Z., Sasselov, D. D., & Szentgyorgyi, A. H. 2001b, AJ, 122, 2477

Mochejska, B. J., Macri, L. M., Sasselov, D. D., & Stanek, K. Z. 2000, AJ, 120, 810

Mochejska, B. J., Macri, L. M., Sasselov, D. D., & Stanek, K. Z. 2004, in Astronomical Society of the Pacific Conference Series, Vol. 310, IAU Colloq. 193: Variable Stars in the Local Group, ed. D. W. Kurtz & K. R. Pollard, 41

Mould, J., Barmby, P., Gordon, K., et al. 2008, ApJ, 687, 230

Mould, J. & Kristian, J. 1986, ApJ, 305, 591

Ngeow, C.-C., Kanbur, S. M., Nikolaev, S., Tanvir, N. R., & Hendry, M. A. 2003, ApJ, 586, 959

O'Connell, D. J. K. 1951, MNRAS, 111, 642

Oláh, K., Kolláth, Z., & Strassmeier, K. G. 2000, A&A, 356, 643

Ostriker, J. P. & Gnedin, O. Y. 1997, ApJ, 487, 667

Paczyński, B. 1971, ARA&A, 9, 183

Pagano, I., Ventura, R., Rodono, M., Peres, G., & Micela, G. 1997, A&A, 318, 467

Perryman, M. A. C., de Boer, K. S., Gilmore, G., et al. 2001, A&A, 369, 339

Perryman, M. A. C. & ESA, eds. 1997, ESA Special Publication, Vol. 1200, The HIPPARCOS and TYCHO catalogues. Astrometric and photometric star catalogues derived from the ESA HIPPARCOS Space Astrometry Mission

Petersen, J. O. 1986, A&A, 170, 59

Pettersen, B. R. 1989, Sol. Phys., 121, 299

Pietrzyński, G., Gieren, W., Udalski, A., et al. 2004, AJ, 128, 2815

Popper, D. M. 1967, ARA&A, 5, 85

Popper, D. M. & Etzel, P. B. 1981, AJ, 86, 102

Pritchet, C. J. & van den Bergh, S. 1987, ApJ, 316, 517

Ribas, I., Fitzpatrick, E. L., Maloney, F. P., Guinan, E. F., & Udalski, A. 2002, ApJ, 574, 771

Ribas, I. & Jordi, C. 2003, in Revista Mexicana de Astronomia y Astrofisica Conference Series, 150

Ribas, I., Jordi, C., Vilardell, F., et al. 2005, ApJ, 635, L37

Ribas, I., Jordi, C., Vilardell, F., Giménez, Á., & Guinan, E. F. 2004, New Astronomy Review, 48, 755

Richer, H. B., Crabtree, D. R., & Pritchet, C. J. 1990, ApJ, 355, 448

Saha, A. & Hoessel, J. G. 1990, AJ, 99, 97

Sakai, S., Ferrarese, L., Kennicutt, Jr., R. C., & Saha, A. 2004, ApJ, 608, 42

Samus, N. N., Durlevich, O. V., & et al. 2004, VizieR Online Data Catalog, II/250

Sandage, A., Tammann, G. A., & Reindl, B. 2004, A&A, 424, 43

Sarro, L. M., Sánchez-Fernández, C., & Giménez, Á. 2006, A&A, 446, 395

Schwarzenberg-Czerny, A. 1996, ApJ, 460, L107

Simien, F., Pellet, A., Monnet, G., et al. 1978, A&A, 67, 73

Skrutskie, M. F., Cutri, R. M., Stiening, R., et al. 2006, AJ, 131, 1163

Stanek, K. Z. & Garnavich, P. M. 1998, ApJ, 503, L131

Stanek, K. Z., Kaluzny, J., Krockenberger, M., et al. 1998, AJ, 115, 1894

Stanek, K. Z., Kaluzny, J., Krockenberger, M., et al. 1999, AJ, 117, 2810

Stetson, P. B. 1987, PASP, 99, 191

Thilker, D. A., Hoopes, C. G., Bianchi, L., et al. 2005, ApJ, 619, L67

Todd, I., Pollacco, D., Skillen, I., et al. 2005, MNRAS, 362, 1006

Torres, G. & Ribas, I. 2002, ApJ, 567, 1140

Udalski, A., Szymanski, M., Kubiak, M., et al. 1999, Acta Astronomica, 49, 201

Udalski, A., Szymanski, M., Soszynski, I., & Poleski, R. 2008, Acta Astronomica, 58, 69

Udalski, A., Wyrzykowski, L., Pietrzynski, G., et al. 2001, Acta Astronomica, 51, 221

van Leeuwen, F. 2007, Astrophysics and Space Science Library, Vol. 350, Hipparcos, the New Reduction of the Raw Data (Institute of Astronomy, Cambridge University, Cambridge, UK)

van Leeuwen, F., Feast, M. W., Whitelock, P. A., & Laney, C. D. 2007, MNRAS, 379, 723

Vanbeveren, D. 1993, Space Science Reviews, 66, 327

Vilardell, F., Jordi, C., & Ribas, I. 2007, A&A, 473, 847

Vilardell, F., Ribas, I., & Jordi, C. 2006, A&A, 459, 321

Weinberg, M. D. 2000, ApJ, 532, 922

Welch, D. L., Madore, B. F., McAlary, C. W., & McLaren, R. A. 1986, ApJ, 305, 583

Wilson, R. E. & Devinney, E. J. 1971, ApJ, 166, 605

Wilson, R. E. & Wyithe, S. B. 2003, in Astronomical Society of the Pacific Conference Series, Vol. 298, GAIA Spectroscopy: Science and Technology, ed. U. Munari, 313

Wozniak, P. R. 2000, Acta Astronomica, 50, 421

Wyithe, J. S. B. & Wilson, R. E. 2002, ApJ, 571, 293

Zakrzewski, B., Ogloza, W., & Moskalik, P. 2000, Acta Astronomica, 50, 387

Zaritsky, D., Kennicutt, Jr., R. C., & Huchra, J. P. 1994, ApJ, 420, 87

Zebrun, K., Soszynski, I., Wozniak, P. R., et al. 2001, Acta Astronomica, 51, 317

Zucker, S. & Mazeh, T. 1994, ApJ, 420, 806

Zucker, S. & Mazeh, T. 2006, MNRAS, 371, 1513

A Large optical flare*

The analysis of the time series of the variable stars in our photometric catalog (Chap 2) revealed a large optical flare event on 2000 September 25. Flares are known as sudden and violent events releasing magnetic energy and hot plasma from the stellar atmospheres (see Sect. A.1). The analysis of the observed phenomenon is presented as an example of the potential of our photometric catalog for further studies. The high quality of the obtained photometry and the good time sampling allowed the estimation of the stellar properties (Sect. A.2), an accurate characterization of the main flare (Sect. A.3) and several minor events (Sect. A.4).

A.1 The observed phenomenon

Flares are observed on magnetically active stars and, much more closely, on the Sun. Electromagnetic radiation is emitted across the entire spectrum, from radio waves through the optical range to X-rays and γ rays. The total energy released during a typical solar flare is in the order of 10^{30} erg, while the largest solar two-ribbon flares can emit up to 10^{32} erg.

According to the accepted model of solar flares, in the upper atmosphere, between oppositely oriented magnetic field lines, a current sheet forms and magnetic reconnection takes place, which results in acceleration of particles, and thus produces electromagnetic radiation and plasma heating. On the basis of the solar paradigm one could simply expect that modeling stellar flares is just a question of scaling (e.g., as a function of the released energy, size, duration, etc.). However, besides general similarities, stellar flare observations also unveil problems that cannot be explained with the extended canonical solar flare model, arising from the different spectral distribution of the emitted energy, the role of age and spectral type of the host star, the multiform magnetic field topologies on stars, the tidal forces in active binaries, etc. The only way we could get closer to drawing

*The contents of this chapter were published in Kovári et al. (2007).

up similarities and differences between solar and stellar flares is to continuously broaden the ensemble of analyzed flares (solar and stellar as well), thus making an observational base of different types of flaring activities available for theoretical purposes. This is how solar flare observations can help in the correct interpretation of stellar flares, and reversely.

Flare activity in cool stars is a very common phenomenon. Flares in stars with spectral type earlier than M are observed mainly in UV and X-rays and optical flares (like the most energetic white light flares in the Sun; Hudson et al., 2006) are rare. However, in the less luminous low mass dM stars optical flares often occur. It is also known, that red dwarfs from $\approx 0.3 M_{\odot}$ down to the hydrogen burning limit can release a considerable amount of energy via flare eruptions, even when, in most cases, these objects show very low magnetic activity in their quiescent states.

The complete time-series data (obtained between 1999–2003) was used for the study of the detected flare. The object studied here, which has identifier M31 J00453912+4130395 in Chap. 2, was flagged during the course of the analysis as an object with a large brightening following the characteristic light curve shape of a stellar flare. The finding chart of the object, also cross-identified as 2MASS J00453912+4140395, is shown in Fig. A.1, which contains only a small portion of the full $33\farcm8 \times 33\farcm8$ WFC field of view. The B and V observations resulting from the DIA analysis and subsequent calibration to the standard system are plotted in Fig. A.2, where the large flare event (A) is zoomed in alongside of two other weaker flares (B, C).

A.2 Stellar properties

Table A.1 summarizes the quiescent B and V magnitudes from our INT data, as well as V and I magnitudes from the DIRECT catalog (Mochejska et al., 2001a), and J, H and K magnitudes from the 2MASS catalog (Skrutskie et al., 2006). A self-consistent analysis using the observed object color indexes and the extinction law of Drimmel et al. (2003) indicates a color excess of $E(B-V) = 0.05$ mag, and, adopting a ratio of 3.1 between A_V and $E(B-V)$, leads to an absolute extinction of 0.16 mag. The unreddened color indexes are most compatible with a spectral type M4 dwarf with $M_V = 13.8$ mag, $\log L/L_{\odot} \approx -2.5$, $\mathcal{M} \approx 0.16$ $M_{\odot}$ and $R \approx 0.2$ $R_{\odot}$ according to the tabulations from Baraffe & Chabrier (1996), Baraffe et al. (1998), and Bessell et al. (1998). The distance resulting from the analysis is of roughly 300 pc.

KPNO plates taken from the M 31 field (NOAO Science Archive, Aladin Sky Atlas[1]) also agree with a mid-M or later spectral type classification since the object

[1] http://aladin.u-strasbg.fr/

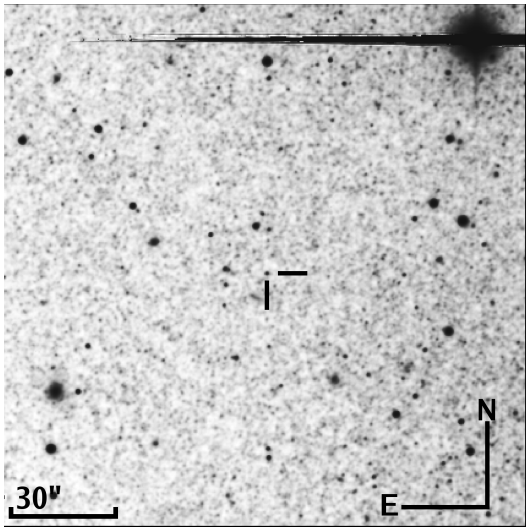

Figure A.1. Finding chart from the M 31 field with flare source (INT WFC image).

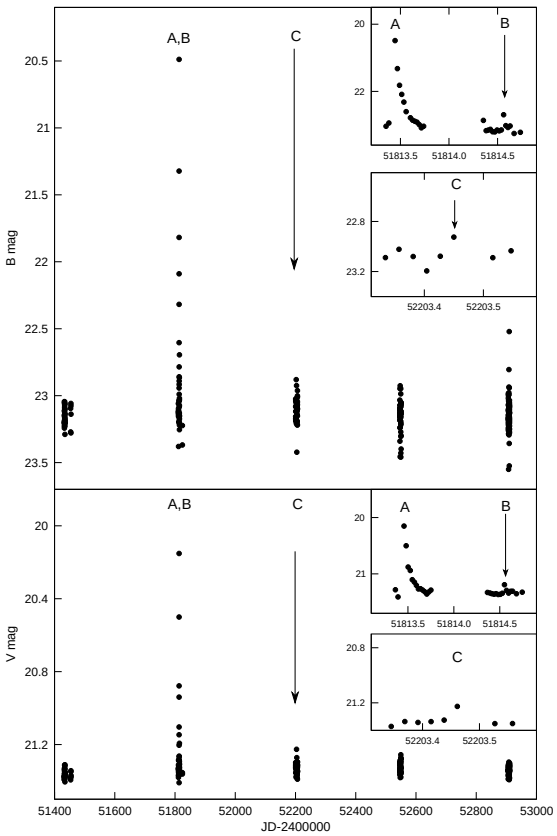

Figure A.2. Light curves in Johnson *B* and *V* of 2MASS J00453912+4140395, taken with the WFC of INT in La Palma, between 1999-2003. Three individual flare events (flares A, B and C) are marked and zoomed.

Table A.1. Catalog data on the observed target.

	INT WFC	DIRECT	2MASS
object ID	M31_J00453912+4140395	D31J004539.1+414039.5	J00453911+4140396
α (J2000)	00 45 39.12	00 45 39.11	00 45 39.12
δ (J2000)	+41 40 39.5	+41 40 39.46	+41 40 39.7
B	23.18		
σB	0.11		
V	21.38	21.62	
σV	0.03	0.07	
I		18.18	
σI		0.07	
J			16.35
σJ			0.11
H			15.98
σH			0.16
K			15.63
σK			0.18

is best seen in the I-band KPNO plates, but also observable in Hα and R. However, in the U, B, and V band plates our target is indistinguishable from the background.

A first step towards evaluating the level of magnetic activity of the studied target is to investigate possible cyclic (rotational) variability induced by surface inhomogeneities (e.g., cool spots). No convincing sign of such modulation was found from our Fourier analysis. Three possible explanations can be put forward. First, spot coverage could be too small to observe any rotational modulation (this is the case when observing our Sun as a star in optical photometric bands). Alternatively, the star could be heavily spotted and yet show small or no modulation if spots are evenly distributed. If we compare the mean error of the measurements in B is 0.08 mag with a scatter of 0.11 mag, i.e., there is still room for some low-level modulation, although the V band does not seem to show such behavior with a scatter of 0.03 mag and a 0.04 mag formal error. The third possible scenario is a low inclination ($i \approx 0^\circ$) of the rotation axis making it not possible to observe any rotational variability. However, in this latter case one could expect variability on a longer timescale of a few years, because of changes in the overall spot coverage according to solar-like spot activity cycle (see e.g. Oláh et al., 2000). No such long-term modulation is seen during the 5-year long observing season and 2MASS J00453912+4140395 seems to be like the vast majority of cool M dwarfs with rotational variability less than 1 – 2% in the visible.

A.3 Flare energy estimation

Flare statistics of red dwarf stars show that stellar flares can generally be divided into two subgroups: a group consisting of relatively small, shorter ($\approx 10^3$ s) im-

pulsive flares, and a more energetic group releasing at least 10^{32} erg and lasting $\approx 10^4$ s. The latter are often related to solar two-ribbon flares which are associated to filament eruptions and coronal mass ejections (CMEs). The basic properties of flare A observed on 2000 September 25 (beginning at HJD 2451813.45), such as the long duration reaching $\Delta t_B \approx 3 \times 10^4$ sec and the large amplitudes of ΔB =2.69 mag and $\Delta V = 1.23$ mag clearly class this event among the more energetic group.

Flare light curves usually consist of a rapid rise followed by a slower, monotonic decay. However, our poorly covered rising phase permits only a rough estimation of the physical properties. For the estimation of the flare energy first we derived intensity from the magnitude values:

$$\frac{I_{0+f}}{I_0} = 10^{\frac{\Delta m_{B,V}}{2.5}}, \tag{A.1}$$

where I_{0+f} and I_0 are the intensity values of the flaring and the quiescent stellar surfaces, respectively, in one of the observed bands. The relative flare energy is then obtained by integrating the flare intensity over the flare duration:

$$\mathcal{E}_f = \int_{t_1}^{t_2} (\frac{I_{0+f}(t)}{I_0} - 1) dt. \tag{A.2}$$

The quiescent stellar fluxes in different bands are estimated assuming a simple black body energy distribution for a dM4 star with $T_{\rm eff} = 3100\,$K, taking $R \approx 0.2 R_\odot$ (see Sect. A.2) from the equation

$$F_\star = \int_{\lambda_1}^{\lambda_2} 4\pi R^2 \mathcal{F}(\lambda)\, S_{B,V}(\lambda) d\lambda, \tag{A.3}$$

where $\mathcal{F}(\lambda)$ is the power function and $S_{B,V}(\lambda)$ is the transmission function for a given passband. Finally, the total integrated flare energy is calculated by multiplying the relative flare energy and the quiescent stellar flux:

$$E_f = \mathcal{E}_f F_\star. \tag{A.4}$$

Since our flare light curve is poorly covered, the abrupt rising phase with its real peak value may be estimated as even 1.5 – 2 mag brighter in B and ≈1.3 mag brighter in V than the measured maxima. This assumption corresponds to a photometric flare temperature of $\approx 1.5 \times 10^4$ K at peak (cf., e.g., Ishida, 1990; Ishida et al., 1991, and references therein). According to this, the observed and dereddened $B - V$ peak of 0.29 mag is just an upper limit of a more reliable $B - V \approx -0.16$ mag. Calculated luminosities for the quiescent star, and the total flare energy for both the minimum fit and the more realistic assumption are summarized in Table A.2, together with the ratio of the flare energy and the quiescent

Table A.2. Quiescent stellar flux and flare energy estimations. A minimum flare energy is estimated both from a minimum fit of the observed data and also by a (more realistic) reconstruction of the rising phase (values in parenthesis).

band	quiescent flux 10^{29} [erg/s]	flare energy 10^{34} [erg]	equivalent duration [h]
B	5.09	3.56 (6.34)	19.4 (34.6)
V	12.76	1.77 (3.47)	3.9 (7.6)

stellar luminosity, often called as equivalent flare duration, i.e., the time interval in which the star would radiate as much energy as the flare itself. The ratio between the flare energies $E_B/E_V = 2.01$ (or 1.83 for the more realistic estimation) is in the order of the statistical value of $1.60^{+0.13}_{-0.32}$ from Lacy et al. (1976). Using the empirical correlation of

$$E_U = 1.2 \pm 0.08 E_B \tag{A.5}$$

we derive an estimation of 4.27 (7.61) 10^{34} erg for E_U. From this we can estimate the total flare energy released in the optical range as being in the order of a few times 10^{35} erg, and resulting in a value of $\simeq 10^{36}$ erg for the bolometric flare energy (cf. the review of Pettersen, 1989). This rough but still realistic estimation (cf. the example in Pagano et al., 1997, with $\sim$ 3 times more brightness in *U*) indicates that the 2000 September 25 flare is among the most energetic stellar flares ever observed.

A.4 Weak flaring and post-flare events

There are statistical evidences that flare-like transient phenomena, often called microflares, are almost continuously present on M-type dwarfs. These events are thought to be one of the major sources of chromospheric and coronal heating. We see them (sometimes as nanoflares) also on the Sun (e.g., Lin et al., 1984), however, because of being relatively weak and short-term events most of them remain unresolved.

For filtering out such short-duration events from the background of our photometric data we searched for small amplitude peaks occurred simultaneously in both photometric colors. We applied different filtering algorithms but finally a visual inspection proved to be the most reliable and efficient. Two such events are apparent. One is just one day after flare A at HJD 2451814.55 (marked with B in Fig. A.2) and another one at HJD 2452203.45 (flare C in Fig. A.2). There are some additional albeit less convincing ones, which are only 2-σ away from the photometric background, and therefore were disregarded. Following the method described in Sect. A.3 we estimate the total energy of flares B and C to be from

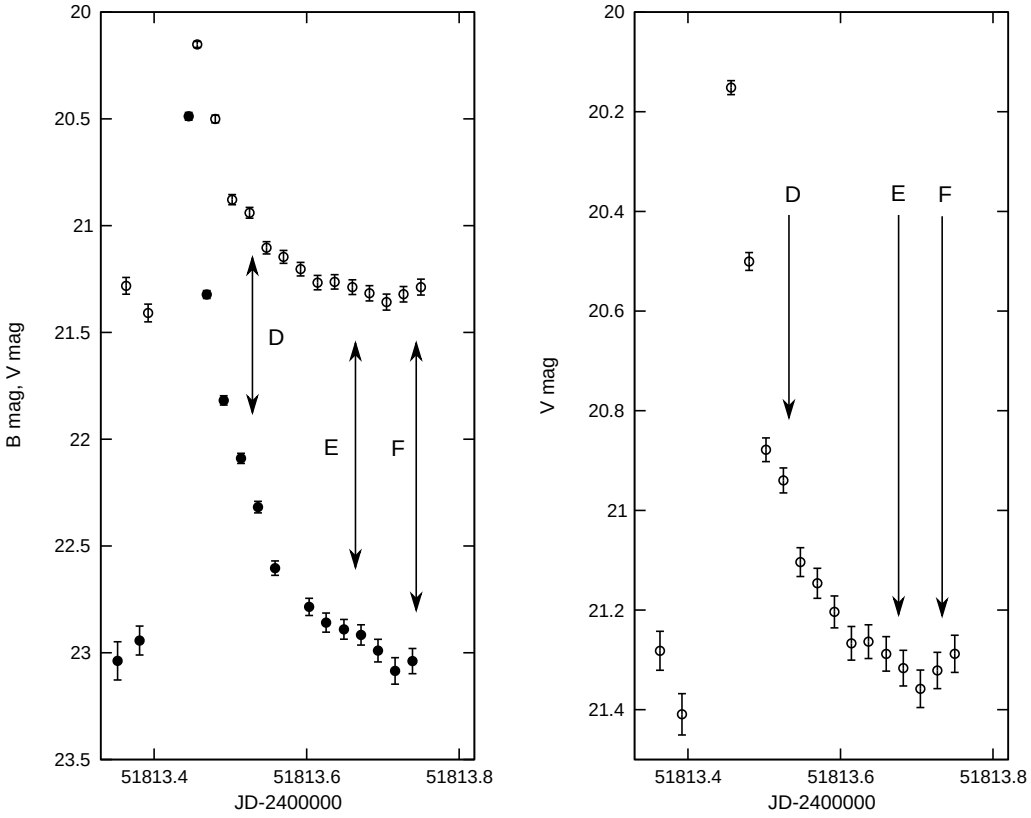

Figure A.3. The large flare of 2000 September 25 (flare A in Fig. A.2) with three post-flare events (D,E and F). *Left. B* (dots) and *V* (circles) light curves together. **Right:** Zoomed *V* curve plotted alone.

a few times 10^{32} erg up to 10^{33} erg in *B*, which are characteristic of a short-term impulsive flares rather than microflares.

When analyzing the decay phase of the light curve of flare A, three other short term increases can be identified. Since those events occurred simultaneously in both colors, we assume them to be an additional three weak flares: one at HJD 2451813.54 (D in Fig.A.3), another one at HJD 2451813.67 (E) and a third one just at the end of the large flare light curve at HJD 2451813.74 (F), all of them lasting about $\Delta t \approx 8\times10^3$ sec (in the case of flare F, the simultaneous rise in *B* and *V* together is considered as just the beginning of the flare event and its duration is extrapolated). Again, we estimate the total flare energies as $2 - 6 \times 10^{31}$ erg in *B* and about a half of this value in *V*. The occurrence of such weak post-flare events in the descending phase of a large long duration flare is a reminder of the mechanism described first by Attrill et al. (2007), which probably occurs on the Sun during large CMEs. After energetic solar flares are associated with CMEs, the moving footpoints of the blowing up magnetic loop crosstalk with opposite polarity flux ropes from the randomly distributed magnetic carpet, or other favorably oriented magnetic concentrations (active regions), thus forming

current sheets and triggering other (micro)flare events from time to time. This seems a plausible interpretation for the three weak flare-like events (D, E and F) observed during the decay phase of flare A.